FACULTY OF ENGINEERING AND APPLIED SCIENCE

DEPARTMENT OF MECHANICAL ENGINEERING

A Computational and Experimental Study of the Dewatering Hydrocyclone

by

Derek Matthew Small

A thesis submitted for the degree of
Doctor of Philosophy

UNIVERSITY OF SOUTHAMPTON

May, 1999

UNIVERSITY OF SOUTHAMPTON

ABSTRACT

FACULTY OF ENGINEERING AND APPLIED SCIENCE

DEPARTMENT OF MECHANICAL ENGINEERING

Doctor of Philosophy

A COMPUTATIONAL AND EXPERIMENTAL STUDY OF THE DEWATERING HYDROCYCLONE

by Derek Matthew Small

This thesis describes research undertaken to further the current understanding of the dewatering hydrocyclone.

Several simplified analytical models of different aspects of flow in the dewatering hydrocyclone are developed in an attempt to illustrate key features of single and multi-component flow in the device.

The distribution of the oil and water components within a operational dewatering hydrocyclone is presently not well understood. Since the opacity of the oil component makes optical methods impractical this thesis presents experimental work making use of electrical impedance tomography to determine the distribution of oil and water in a cylindrical duct, as a preliminary to the application of this technique to the hydrocyclone.

An extensive computational study of a dewatering hydrocyclone geometry operating at different flow rates is described and compared with experimental data. A key feature of such models is the way in which turbulence is modelled. This thesis presents a series of models to demonstrate and quantify the inadequacy of isotropic turbulence models for modelling the strongly swirling flows in a hydrocyclone. The use of Lagrangian and Eulerian multi-component models is also discussed.

Contents

List of Figures

List of Tables

Chapter 1

A List of Terminology

(r, θ, z) Cylindrical polar coordinates

$\mathbf{e}_r$ Unit vector in r direction

$\mathbf{p}$ Pressure

$\mathbf{v}$ Fluid velocity

(v_r, v_θ, v_z) Velocity components in r, θ and z directions, respectively.

$\mathbf{t}$ Time

ρ Density

Γ Fluid angular momentum $= rv_\theta$

$\mathcal{H}$ Head $= \frac{p}{\rho} + \frac{1}{2}(v_r^2 + v_\theta^2 + v_z^2)$

ψ Stokes' streamfunction

(R, θ, ϕ) Spherical polar coordinates

v_r, v_θ, v_ϕ Velocity components in spherical polar coordinates

ω vorticity vector $= \nabla \times vecv$

α^* cone semi-angle of hydrocyclone

μ dynamic viscosity

ν kinematic viscosity

λ turbulent mixing length

s distance along conical wall of hydrocyclone, used in boundary layer analysis

ρ_s Particle density

d Particle diameter

Q Volumetric flux

T_A Time for particle to reach steady state velocity

T_C Time for fluid to complete one revolution of hydrocyclone

A_i Area of hydrocyclone inlet

b Radius of hydrocyclone at inlet

V_θ, V_z Inlet velocities

F Split ratio $= \frac{Q_{overflow}}{Q_{inlet}}$

r_0 Radius used in non-dimensionalisation

$\hat{r}$ Non-dimensional radius. Other non-dimensional quantities and scalings are notated similarly.

$\mathcal{D}$ Linear differential operator

Re Reynolds' number

γ Aspect ratio of hydrocyclone $= \frac{r_0}{z_0}$

μ Dependent variable used in analytical model; $\mu = r^2$

α_i Volume fraction of component i in two component flows

ϵ small parameter, used in stability analysis

n Number of electrodes in tomography

V Electrical potential (V)

ΔV Potential difference (V)

N Rotational speed of mixing pump (RPM)

ρ Electrical resistivity

J_0 Current flux at boundary of tomography vessel

σ Conductivity of fluid mixture, $\sigma = \frac{1}{\rho}$

ϕ Arbitrary scalar

Γ_ϕ Diffusivity of ϕ

S_ϕ Source of ϕ

k Turbulent kinetic energy

ϵ Rate of dissipation of turbulent kinetic energy

ν_T Turbulent (scalar) viscosity

D_0 Diameter of hydrocyclone at inlet

$\mathbf{S_d}$ deviatoric mean stress tensor

$\mathbf{\Sigma_d}$ deviatoric Reynolds' stress tensor

$\mathbf{I}$ Second rank identity tensor

η Isotropy parameter

S Swirl number

ΔP_{io} Pressure drop from hydrocyclone inlet to overflow exit

ΔP_{iu} Pressure drop from hydrocyclone inlet to underflow exit

R_{v_θ} Radius of maximum v_θ in the hydrocyclone

R_{v_z} Radius of zero vertical velocity in the hydrocyclone

Chapter 2

Introduction

2.1 Industrial Context

Commercial offshore oil-fields produce a mixture of crude oil, gas and brine, with the proportion of brine rising as the oil-field reaches the end of its working life. With the emphasis in modern oil production being to extend the lifetime of economically viable operation of oil-fields has come an intensification of interest in separation technology.

The mixture of components produced is input into a primary three-way separator, typically a large gravitational separator, which removes the gas and performs an initial separation of brine from the oil. The brine output must then be cleaned up to meet strict environmental limits (<40 mg/l at present) before it can be discharged into the sea. Gravitational separators are large, with volumes of typically 100 m^3 or greater, and correspondingly heavy. This has a significant economic impact on oil production, since the oil-platform must be engineered to support this weight. This expense is even greater with modern floating oil platforms. The deficiencies of such separators have led to a search for alternatives, with hydrocyclones prominent amongst the candidates.

2.2 The Hydrocyclone

The hydrocyclone (as depicted in 2.1) is a device for separating two components (at least one of which must be a fluid) of different densities. The mixture is injected into the device via tangential inlets, and the rapid rotation of the fluid causes the denser component of

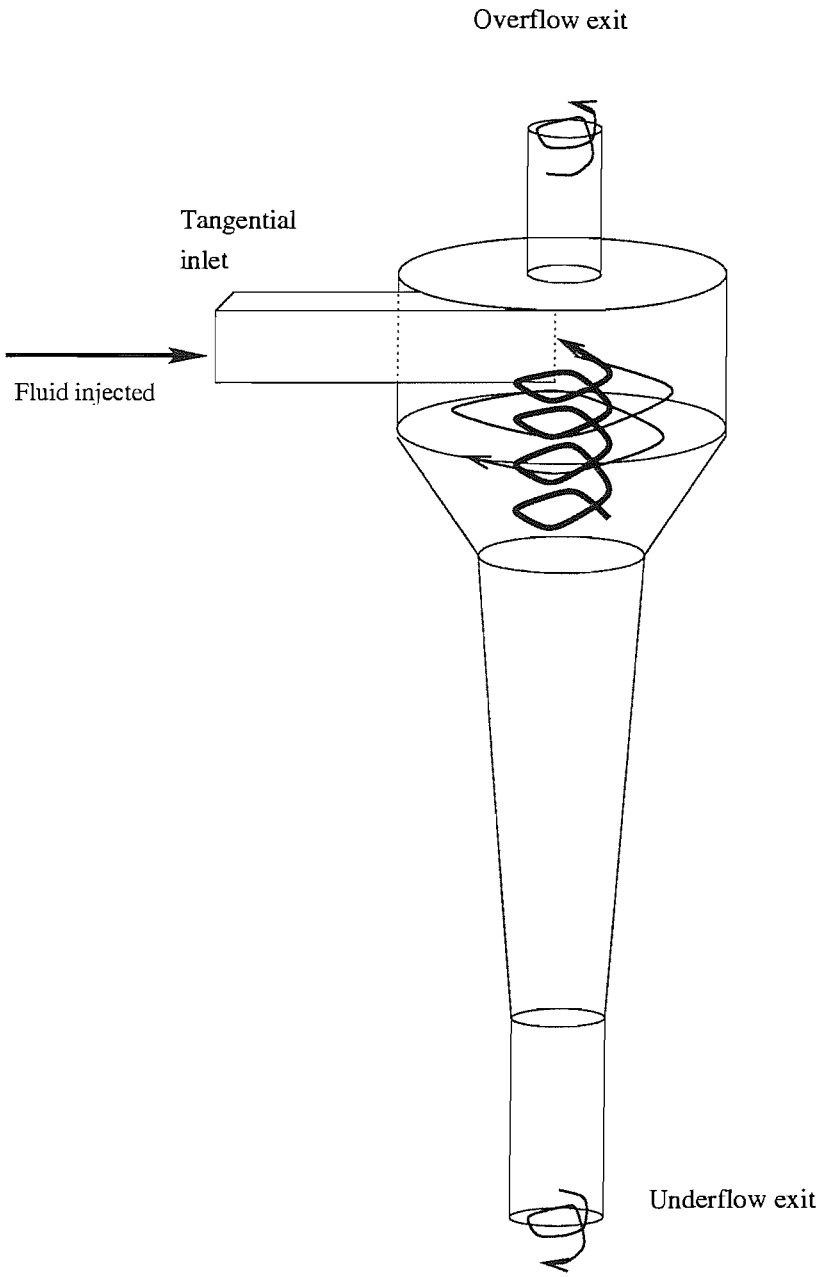

Figure 2.1: A sketch of a hydrocyclone

the mixture to move towards the wall of the device, while the central region of the flow has a higher concentration of the less dense component. The fluid motion in the device causes a reversal of the central flow near the axis. This means that the less dense component is concentrated in the discharge from the overflow, while the more dense component is concentrated in the underflow discharge.

Note that the terms 'overflow' and 'underflow' refer to the location of the exits relative to the cyclone geometry, rather than the orientation of the device in use. The accelerations

due to the rotation of the fluid are typically many times larger than that of gravity, so that the orientation of hydrocyclones in the field is purely a matter of operational convenience.

2.3 Hydrocyclones in the oil industry

The de-oiling hydrocyclone, as developed by researchers at Southampton University has shown itself to be well suited to the task of cleaning oil-contaminated brine downstream of the primary separator to meet stringent requirements on waste water disposal. Installations of banks of hydrocyclones in pressure vessels take up one third of the space and weigh less than two thirds of a comparable gravitational separation procedure. The modularity of this approach also provides a greater adaptability to varying flow-rates. De-oiling hydrocyclones are manufactured and marketed by Conoco Speciality Systems Inc. under the Vortoil brand-name, and have become the standard method world-wide for cleaning produced water offshore.

This success prompted research on the possibility of using hydrocyclones as a primary separation device offshore, following a de-gassing process. Such a hydrocyclone would be removing water from a (usually) oil-continuous mixture, in contrast to the clean-up hydrocyclone which is used to remove oil from water-continuous dispersions. We shall refer to the two kinds of hydrocyclones as dewatering and deoiling respectively.

Since the primary separator, unlike a secondary water clean-up process, must handle the full flow from an oil-field, the advantages of the compactness, convenience and low-maintenance costs of hydrocyclones is even more significant here than in the cleaning role. It is this, and the size of the potential market, which make the commercially exploitable dewatering hydrocyclone a continuing research goal at Southampton University, despite the difficulties described below.

2.4 The De-watering Hydrocyclone

The dewatering hydrocyclone operates in a more difficult regime than the de-oiling hydrocyclone, for a number of reasons: The water droplets must migrate through the more viscous oil component; the water droplets, being less viscous, are more prone to break-up;

and the migration outward is opposed to the main flow in the hydrocyclone, which is in towards the axis.

Additional difficulties are caused by the transition from an oil continuous to a water continuous dispersion within the device. This can cause high effective viscosities, and inhibit the rotation of the fluid in the hydrocyclone.

These difficulties have limited the commercial deployment of the dewatering hydrocyclone, but the size of the market makes it desirable to attempt to overcome them.

Research on the dewatering hydrocyclone began at Southampton University in the early 1980's, carried out mostly by Ian Smyth and Martin Thew. Smyth [1] developed and tested a range of geometries. Later Alistair Sinker [2] worked on the possibility of improving performance using demulsifiers, and made detailed measurements of droplet size distributions at the inlets and outlets of the hydrocyclones. Droplet size within the hydrocyclone has a drastic effect on performance, since the centrifugal force on a droplet is proportional to its volume, while the drag on it is depends on its surface area. The ratio of surface area to volume decreases with size, meaning that larger droplets settle out faster.

2.5 Hydrocyclones and CFD

Computational fluid mechanics (CFD) has been applied to liquid-liquid hydrocyclones before, by John Hargreaves[3]. At that time the study focussed on de-oiling hydrocyclone, and the computational resources available at the time forced some compromises to be made on turbulence modelling and the treatment of the walls. The study was mostly concerned with the study of de-oiling hydrocyclones, so that the dilute dispersed oil phase could be treated using particle-tracking methods, while ignoring the interactions between particles.

2.6 Goals of Research

Investigation of the interior flow of a hydrocyclone is a difficult problem, especially in the case of a dewatering hydrocyclone, where the mixture of oil and water does not

permit optical methods. A result of this is that our knowledge of the distribution of the components within the device at present comes only from the comparing the flow going into the hydrocyclone with that leaving. This make it difficult to design a better hydrocyclone, since there we have little information about how the geometry affects what happens within the geometry.

The research described in this thesis was intended to use computational, mathematical and experimental methods to investigate the dewatering hydrocyclone.

The goals of the research were

- To develop computational models of the dewatering hydrocyclone, initially for single component flow, but later for two component flows of oil and water, and to validate these models with the available experimental data;
- To develop a method for measuring the concentration of the two components within the hydrocyclone, based on electrical impedance tomography, without disturbing the flow;
- To use the tomographic data for the validation of the computational two component model.

Chapter 3

A Review of Analytical Models of the Hydrocyclone

3.1 Introduction

3.1.1 Advantages and Disadvantages of Analytical Models

This chapter constitutes a review of various existing analytical models of hydrocyclones. No analytical model exists which can describe the full complexity of the flow in a hydrocyclone, largely because of the difficulties of incorporating turbulence into such a model. Analytical models are developed using a considerable number of simplifying assumptions, such as inviscid, axi-symmetric flow, and even then attention is usually restricted to a limited part of the geometry of the device.

It is therefore unlikely that any such model could displace experimental testing, full scale computational models or even empirically derived phenomenological models, however this is not their purpose. Analytical models are used in an attempt to understand important aspects of the flow in a hydrocyclone, such as the mechanisms underlying axial reversal, details of the flow in the wall boundary layer, and the forces which dominate in different regions of the hydrocyclone. Also, an analytical (or semi-analytical) model of a hydrocyclone enjoys some of the advantages of empirical correlations: namely that instant feedback may be achieved for changes in geometry or flow-rate, while still resting on more secure theoretical foundations. This is something which is some way from being

achieved with large computational models.

3.1.2 An Overview of the Flow in a Hydrocyclone

The zones of flow in a hydrocyclone are presented in a schematic form in figure 3.1. The

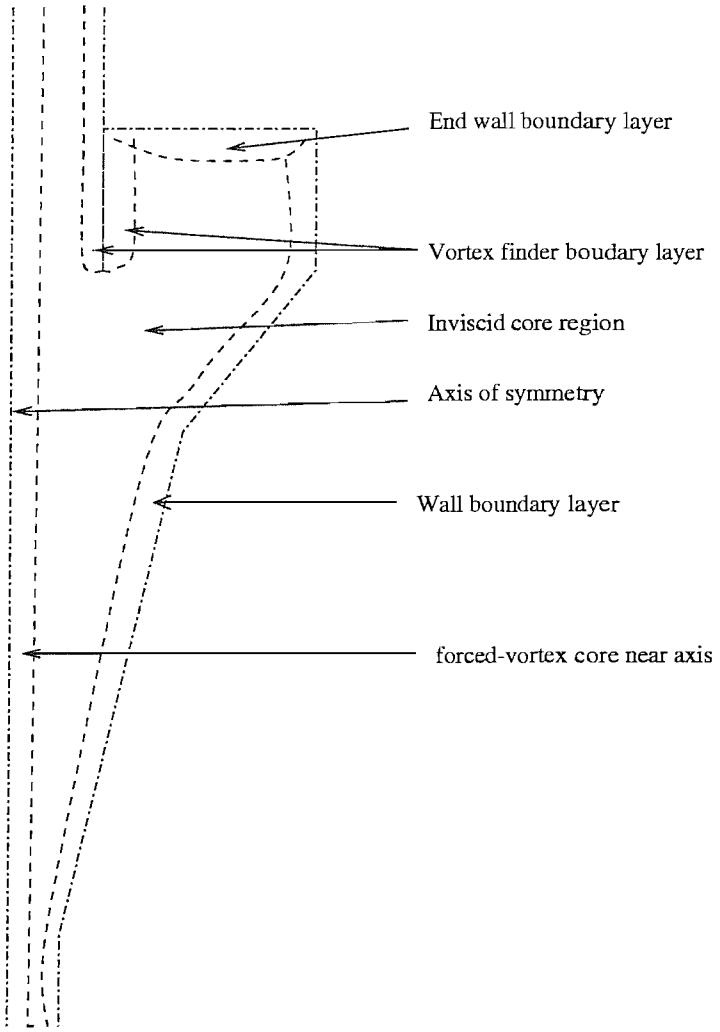

Figure 3.1: A schematic view of hydrocyclone zones

region most commonly modelled, as well as that in which most of the separation occurs, is the 'inviscid' core region. In this region the conservation of angular momentum in the fluid leads to a free vortex structure forming. An inviscid free vortex has a tangential velocity profile of $v_\theta = Ar^{-1}$ for some constant A. Experimental measurements [4] suggest that in fact the exponent in this equation should be adjusted from -1 to take account of the viscous (and turbulent) properties of the fluid.

Clearly the free vortex cannot continue to the axis of the hydrocyclone, since the swirl

velocity would be infinite there. In practice the fluid in a small region near the axis is in solid body rotation, with tangential velocity profile $v_\theta = Br$, for some constant B. Again, experimental results of Kelsall and others have suggested modifications to this profile.

No-slip conditions must also apply to the walls of the device, and boundary layers are formed near the vortex finder, and the side and top walls. The latter boundary layer is of particular interest, since the tangential velocity must decay rapidly in this region, to be zero at the wall. However, the strong radial pressure gradient required to balance the swirl in the body of the hydrocyclone persists in this region. This gives rise to an acceleration of the flow along the top wall to the vortex finder, and then out of the overflow exit. This so-called 'leakage' flow has not passed through the region of the hydrocyclone where centrifugal forces cause the migration of denser particles or droplets away from the core, and hence is still a mixture of similar properties to that injected in the inlet. This leakage flow contributes significantly to the presence of denser particles in the flow from the overflow exit, and is an important cause of inefficiencies in the hydrocyclone.

Much of the work on analytical models of hydrocyclones has been carried out by Bloor and Ingham in a series of papers [5, 6, 7, 8, 9, 10] published between 1973 and 1987. It is the purpose of this chapter to summarize briefly their methods and achievements, as well as the other work in this field which extends their results. These methods have their limitations, and some of them involve the use of numerical methods, although these are simpler than full-scale CFD. There are also advantages: with relatively simple expressions linking the variables it is possible to consider a change in geometry, say, more easily than in a fully numerical simulation, and the results are more accessible to the intuition.

3.2 Assumptions of Analytical Models

In order to produce an analytical model of a hydrocyclone some simplifications must be made. Firstly, the effects of turbulence are typically neglected, although Bloor and Ingham have published a paper [6] which uses a simple turbulence model. Secondly the analysis of the flow is restricted to the conical region of the hydrocyclone in order to simplify the boundary conditions and to allow the use of conical polar coordinates.

This means that the effect of the top wall on the flow is not explicitly modelled, instead a plausible parameterised form for the stream function is postulated and the wall boundary conditions are used to fix the values of the parameters. The flow field is also considered to be time-independent.

The restriction to the inviscid region of the flow also means that neither the viscous core of the cyclone flow (of great importance in the separation of oil and water, since the oil will collect in this region) nor the flow near the walls (where the density of a heavy dispersed component is greatest) is modelled.

3.3 Preliminaries

Much of the work discussed in this chapter draws on a common mathematical framework for axi-symmetric confined swirling flow, which is briefly outlined here. The development and statement of the equations is most naturally carried out in cylindrical polar coordinates, although spherical polar coordinates are often used for cyclone specific work.

We define the velocity components v_r,v_θ and v_z in the r, θ and z directions respectively. However, we shall find it convenient to introduce the dependent variables $\mathcal{H}$, the total pressure head , Γ the angular momentum (more properly these are head and angular momentum divided by density but for incompressible flows these forms, and this terminology, are more convenient), and ω_θ the azimuthal vorticity of the fluid defined, in cylindrical polar coordinates, by

$$\Gamma = rv_\theta \tag{3–1}$$

$$\mathcal{H} = \frac{p}{\rho} + \frac{1}{2}(v_r^2 + v_\theta^2 + v_z^2) \tag{3–2}$$

$$\omega_\theta = \frac{\partial v_r}{\partial z} - \frac{\partial v_z}{\partial r}. \tag{3–3}$$

Since the flow is symmetric about the axis, i.e., none of the flow variables depends on θ, we may define a Stokes stream function, ψ, such that

$$v_r = -\frac{1}{r}\frac{\partial \psi}{\partial z} \tag{3–4}$$

$$v_z = \frac{1}{r}\frac{\partial \psi}{\partial r} \tag{3–5}$$

so that the continuity equation is automatically satisfied. Note that axial symmetry of the flow is sufficient to allow a Stokes' stream function to be constructed, although unlike the case of planar flow it does not describe the flow completely: the tangential component of velocity must be considered separately.

For inviscid flow it is clear that Γ (by Bernoulli's theorem) and $\mathcal{H}$ (by Kelvin's circulation theorem) are conserved along streamlines, and hence are functions of ψ only.

The radial momentum equation, under the assumption of axial symmetry and steady flow, is

$$v_r \frac{\partial v_r}{\partial r} + v_z \frac{\partial v_r}{\partial z} - \frac{v_\theta^2}{r} = -\frac{1}{\rho}\frac{\partial p}{\partial r}. \tag{3-6}$$

Incidentally, if we assume (as is borne out by experiment) that v_θ is much larger than the other components of velocity in the hydrocyclone then this equation implies that

$$\frac{\partial p}{\partial r} \approx \rho v_\theta^2. \tag{3-7}$$

It is this pressure field which causes the leakage flow at the top wall of the hydrocyclone, as discussed above.

In order to eliminate pressure from this equation the variables Γ and $\mathcal{H}$ may be substituted to yield

$$\omega_\theta = \frac{\Gamma}{r}\frac{d\Gamma}{d\psi} - r\frac{d\mathcal{H}}{d\psi}. \tag{3-8}$$

3.4 The central equation

The first paper on hydrocyclones by Bloor and Ingham [5] defines the mathematical context in which all their work on the subject takes place. The geometry of the hydrocyclone is simplified to a cone, with boundary conditions applied to the open top surface. These boundary conditions in effect replace any consideration of the cylindrical portion of the hydrocyclone. All the flow in the device is assumed to flow down into the cyclone, reverse its direction and exit through the overflow orifice; an assumption which is reasonable in the context of a hydrocyclone designed to separate a dense solid component from a lighter fluid component, so that as little fluid as possible exits via the underflow orifice.

This paper considers the inviscid flow in the region of the hydrocyclone between the

wall boundary layer and the viscous core. The authors begin by establishing the equation

$$\left(v_R\frac{\partial}{\partial R}+\frac{v_\phi}{R}\frac{\partial}{\partial\phi}\right)\left(\frac{\omega_\theta}{R\sin\phi}\right)=0 \tag{3–9}$$

where (R,ϕ,θ) are the independent variables of the spherical polar coordinate system, ω is the vorticity, and subscripts denote the components of vectors. This equation merely asserts that $\omega_\theta/R\sin\phi$ is conserved along a streamline, which means that the (azimuthal) vorticity associated with a stream surface is constant: the vorticity spreads out as the stream surface widens.

This equation is initially derived [5] from the θ component of the vorticity transport equation

$$(\mathbf{v}.\nabla)\omega=(\omega.\nabla)\mathbf{v}, \tag{3–10}$$

which is valid for steady state, inviscid flow. It follows that any subsequent analysis is valid only in the regions of the hydrocyclone in which viscosity is unimportant, i.e. away from the boundary layer, and the forced vortex at the axis of symmetry. The assumption is made that $v_\theta = A/R\sin\phi$, so that components of the vorticity other than in the azimuthal direction are identically zero. In a subsequent paper [6] it was derived under the weaker assumption that v_θ is a function of r only, where $r = R\sin\phi$ is the radial distance from the axis of symmetry. This assumption is suggested by the experimental results of Kelsall [4]. In each case the authors continue by defining a stream function ψ, given by

$$\frac{\partial\psi}{\partial R} = -v_\phi R\sin\phi, \tag{3–11}$$

$$\frac{\partial\psi}{\partial\phi} = v_R R^2\sin\phi, \tag{3–12}$$

so that the continuity equation is satisfied identically. Substituting this into equation 3–9 gives the equation, central to this and subsequent studies,

$$\frac{1}{\sin\phi}\frac{\partial^2\psi}{\partial R^2}+\frac{\partial}{\partial\phi}\left(\frac{1}{R^2}\sin\phi\frac{\partial\psi}{\partial\phi}\right)=-R^2\sin\phi f(\psi), \tag{3–13}$$

for some function $f(\psi)$, where $f(\psi)$ is an unknown function of ψ. It is then possible to postulate a plausible form for $f(\psi)$, allowing equation 3–13 to be solved for ψ. This equation is used in [11] as well as [5, 6]. Note that the assumptions mentioned above for the azimuthal velocity amount to a prescription for the inlet velocities, which may

not be true in the upper part of the hydrocyclone, where the flow is not yet genuinely axisymmetric. We shall return to this.

In [5] equation 3–13 is used to find approximate flow velocities in a small angle hydrocyclone. It is assumed that the function $f(\psi)$ may be expanded in a power series in $(\alpha^* - \phi)$, where α^* is the cone semi-angle of the hydrocyclone, and that the leading order term behaves like $F\psi^\delta$, where F and δ are constants. It is further assumed that the cone semi-angle is sufficiently small that $\sin\phi \approx \phi$, and that rates of change with R are much smaller than rates of change with ϕ.

The authors proceed to assume the existence of an approximate solution of the form

$$\psi = Br^\beta \phi^\gamma (\alpha^* - \phi), \tag{3–14}$$

where β and γ are constants to be determined.

This is substituted into equation 3–13, and by equating coefficients it is found that $\beta = \gamma = 3/2$ are the appropriate values for these coefficients. Retaining only two terms in the expansion of $(\alpha^* - \phi)$ yields quite good agreement with the experimental results of Kelsall [4].

The velocity components v_R and v_ϕ are given by

$$v_R = \frac{1}{2}B(R\phi)^{-1/2}(3\alpha^* - 5\phi) \tag{3–15}$$

$$v_\phi = -\frac{3}{2}BR^{-1/2}\phi^{1/2}(\alpha^* - \phi) \tag{3–16}$$

These equations may be resolved into horizontal and vertical components (v_H and v_V, respectively)

$$v_V = v_R, \tag{3–17}$$

$$v_H = -BR^{-1/2}\phi^{3/2} \tag{3–18}$$

The constant B may be determined from the volume flux through the hydrocyclone, ignoring the underflow and leakage from the boundary layer on the vortex finder to the overflow. Of course, in practice, these may not be negligible. In [5] it was assumed that $v_\theta = A/r\sin\phi$, and that the constant A may be determined from the cross-sectional area of the inlet and the volume flux[1]. This analysis produces velocity profiles which compare well with the experimental results of Kelsall [4].

[1]In this paper, and others by Bloor and Ingham, it is assumed that the hydrocyclone is conical

3.5 Turbulence

The next paper considered, [6], is a sequel to [5] in which the effects of turbulence on a hydrocyclone flow are considered. The addition of turbulence allows the azimuthal velocity to be predicted, in contrast to the previous model in which a free vortex was assumed. This has significant implications for the separation performance of the hydrocyclone, since the azimuthal velocity determines the centrifugal force experienced by a particle of different density from the continuous component.

The turbulence model is developed by using dimensional analysis to find constraints on the turbulent viscosity, which is assumed to affect only the azimuthal component of velocity. The axial and radial components of velocity are assumed to take the same form as in the inviscid model described in [5].

The velocity components of equation 3–17 are rewritten in cylindrical polar coordinates, (r, θ, z)

$$v_R = -Br^{3/2}/z^2 \tag{3–19}$$

$$v_z = \frac{1}{2}Br^{-1/2}(3\alpha^* - 5r/z). \tag{3–20}$$

Substituting these velocities into the azimuthal component of the momentum equation and recalling the assumption made earlier that v_θ is a function of r only, gives

$$-\rho B\frac{R^{1/2}}{z^2}\frac{d}{dr}(v_\theta r) = \frac{\partial}{\partial r}\left[\mu\left(\frac{dv_\theta}{dr} - \frac{v_\theta}{r}\right)\right] + \frac{2\mu}{r}\left(\frac{dv_\theta}{dr} - \frac{v_\theta}{r}\right). \tag{3–21}$$

It is clear from a dimensional analysis of this equation that the (turbulent) viscosity must have the form $\mu = f(r)/z^2$. This is not so unreasonable as it may appear: the authors cite work which suggests that the appropriate mixing length is the width of the boundary layer, and that this increases with proximity to the inlet of the hydrocyclone, at least in the upper part of the hydrocyclone. It is thus argued that a mixing length of the form $l \propto 1/z$ is not unreasonable. However the agreement with the expression for boundary layer thickness referred to (derived by Rott and Lewellen using a momentum integral method) is only qualitative. Substituting this form for μ into equation 3–21 reduces it to an ordinary differential equation, which may be solved in terms of the Incomplete Gamma function.

The solutions obtained by this method are a considerable improvement on the inviscid model used earlier, showing the appropriate Rankine vortex-type profile for the swirl velocity, and the results are also in tolerable agreement with Kelsall's experimental data, as shown in figure 3.2 below

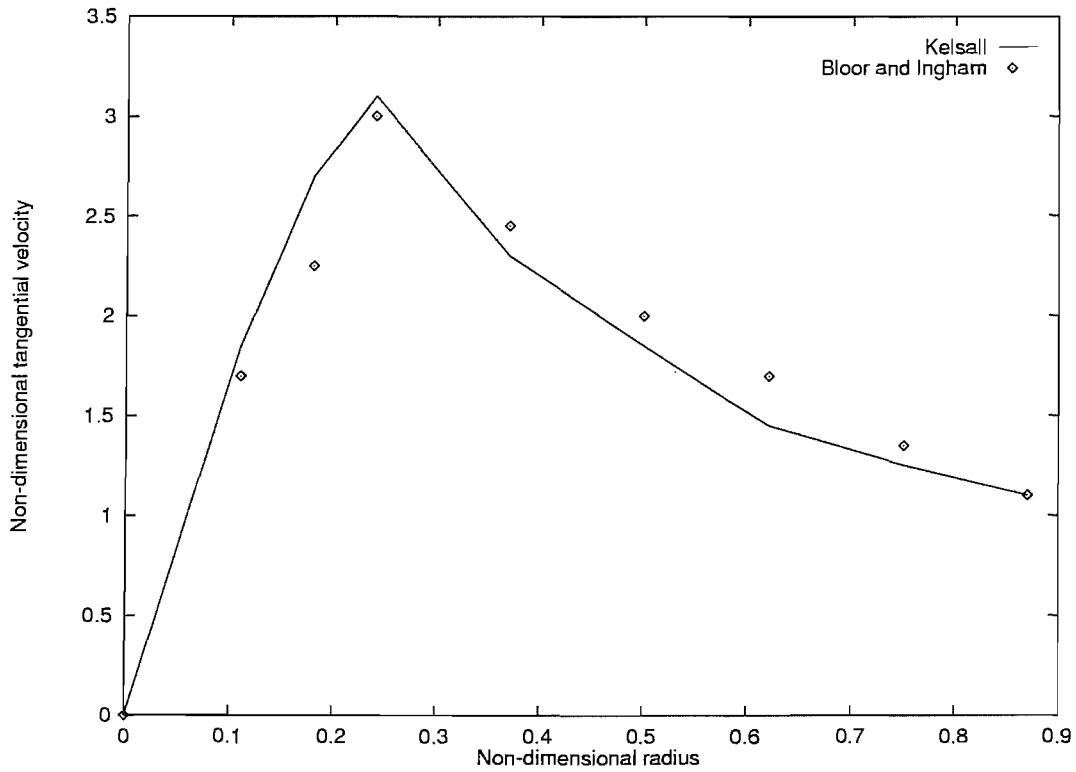

Figure 3.2: A Comparison of Tangential Velocity

The authors continue by introducing a more detailed mixing length hypothesis

$$\mu = \frac{M}{z^2}\left|\frac{dv_\theta}{dr} - \frac{v_\theta}{r} + K\right| \tag{3–22}$$

formed by analogy with the Prandtl's expression

$$\mu = \rho\lambda^2\left|\frac{dv}{dy}\right| \tag{3–23}$$

with $\frac{dv}{dy}$ replaced by a suitable component of the rate of strain tensor. The term K in 3–22 is introduced so that the turbulent viscosity does not vanish, even in the forced vortex region where the solid body rotation produced by viscous effects causes the rate of strain tensor to vanish. This equation may be substituted into 3–21 and solved numerically. The results presented in [6] do not show any startling improvement in agreement with Kelsall's data over the simpler model described above.

3.6 Boundary layers

The wall boundary layer region of the cyclone (as depicted in figure 3.1) is important in the operation of a conventional hydrocyclone, since the denser particles will collect here, and become entrained in the boundary layer which contributes much of the flux out of the underflow.

The boundary layer is one region of the hydrocyclone where analytical models have an advantage over computational models: the latter rely heavily on logarithmic wall functions to avoid modifications to their turbulence models which would otherwise be necessary in this region. The flow in the boundary layer has been investigated by Bloor and Ingham [7] for a single component hydrocyclone flow, although it is likely that the high concentration of particles is this region will have a significant impact on the flow.

It is assumed that the flow in the boundary layer, where viscosity is important, matches onto the solution for the inviscid core region derived earlier.

The coordinate system used in this paper is a special conical system: (s, n, θ), where s is distance along the axis of the cone, from the vertex, n is distance perpendicular to the surface of the cone, and θ is the azimuthal angle. In order to use the Pohlhausen method it is necessary to make some plausible assumptions about the velocity profiles in the boundary layer. The authors first assume that the velocity profiles across the boundary layer are functions of a similarity variable: $\xi = n/\delta(s)$ where $\delta(s)$ is the boundary layer thickness. Denoting the non-dimensionalised values of velocity components in the s and θ directions by v_s and v_θ, where non-dimensionalisation has been carried out using values just outside the boundary layer, the forms

$$v_s = f'(\xi) + a(s)h'(\xi) \tag{3-24}$$

$$v_\theta = g(\xi), \tag{3-25}$$

were adopted, where the functions $f'(\xi)$,$g(\xi)$ and $h'(\xi)$ are fixed low order polynomials (varying between 0 and 1) chosen to match on to the core flow in such a way that there is no shear at the interface between the boundary layer and the main flow.

The function $a(s)$ is introduced to allow for the effects of the pressure gradient: in the boundary layer the radial pressure gradient is higher than it needs to be to balance the centrifugal force, since the fluid in the boundary layer is moving slower than that in

the core. It follows that the excess pressure gradient, resolved along the wall of the cone, will accelerate the boundary layer towards the underflow. This may cause the value of the (non-dimensional) v_s to exceed 1, a phenomenon known as 'overshoot'.

When the expressions for f', g and h' are introduced into the boundary layer equations a pair of ordinary differential equations for $a(s)$ and $\delta(s)$ are obtained. These must be solved numerically, and the results are presented in [7]. The results show the dependence of the overshoot on the non-dimensional parameters

$$L = -\rho \frac{r_0^2 V_s}{s_0 \mu_m}, \tag{3–26}$$

and

$$M = -V_{0,s}/V_{0,\theta} \tag{3–27}$$

where r_0 is the radius of the hydrocyclone at the inlet, s_0 is the distance along the director of the cone to the inlet, $V_{0,s}$ and $V_{0,\theta}$ are the inlet velocity along the hydrocyclone wall and the inlet swirl velocity, respectively, and ρ and μ_m are the density and effective viscosity (taking into account turbulence) of the fluid. The former is a sort of Reynolds' number. The authors also evaluate the meridional flux through the boundary layer (i. e. that towards the apex). This is predicted to decrease as the apex is reached, which the authors take to be evidence of a leakage of vorticity into the core flow, which might explain the success of their previous rotational inviscid models.

No direct comparison with experimental measurements is made for this model.

3.7 Particle motion

The material in this section is drawn from [5], and is the basis for the more sophisticated calculations of particle motions in CFD simulation studies. We begin by considering the equation of motion for a spherical particle, from a Lagrangian point of view

$$\rho_s \frac{\pi d^3}{6} \frac{\partial V}{\partial t} = F - 3\pi\mu V d \tag{3–28}$$

where ρ_s is the density of the particle (assumed to be solid), d is its diameter, U is the relative velocity of the particle with respect to the fluid, μ is the viscosity of the fluid and F is the force acting on the particle as a result of the acceleration of the continuous

component of flow. In the case of a hydrocyclone the force F will be the centrifugal force (in the frame of reference of the particle) due to rotation of the continuous component of the flow. The last expression in this equation describes the drag on the particle, which is assumed to be given by Stokes' law. It is desirable to establish the time scale for the particle to attain a steady drift velocity. It is assumed that the dependency of F on V and t is small, so that a time scale may be established by a dimensional analysis of equation 3–28. This gives

$$T_A = \frac{d^2 \rho_s}{18\mu}. \tag{3–29}$$

A time scale for the flow as a whole may be derived from the time taken for the fluid to complete one revolution of the hydrocyclone . If the volume flux through the inlet, Q, and the area, A_i of the inlet are used to determine a swirl velocity, and the radius of the hydrocyclone at the inlet is denoted by b, then the time taken for the fluid to complete one circuit of the hydrocyclone, a distance of $2\pi b$, at a speed given by Q/A is

$$T_C = 2\pi b \frac{A_i}{Q}. \tag{3–30}$$

Noting further that the equilibrium velocity of the particle, found by setting $\frac{\partial V}{\partial t} = 0$, is

$$U_{eq} = \frac{(\rho_s - \rho) d^2 Q^2}{18\mu A_i^2 b}, \tag{3–31}$$

it is possible to express the condition for the acceleration of the particle to be negligible in the form

$$\frac{Re}{72\pi} \frac{\rho_s^2}{(\rho_s - \rho)\rho} \frac{d}{b} \ll 1 \tag{3–32}$$

where $Re = \rho \frac{V_{eq} d}{\mu}$ is a Reynolds' number for the particle. Experimental evidence suggests that this is unlikely to exceed unity. The ratio of particle to hydrocyclone diameter is expected to ensure that this inequality holds, and the particle motion is thus treated as governed by an algebraic equation. The particle will then tend towards a steady orbit, where its horizontal drift velocity matches the inward radial movement of the fluid. The details of this calculation are carried out in [5], and good agreement with the results of Kelsall is obtained.

3.8 The central equation revisited: Part 1

In their 1984 paper, [9], Bloor and Ingham reconsider equation 3–13. Noting that the form given above for the right hand side effectively prescribes a distribution of azimuthal vorticity, they consider the effect of adding a perturbation term to the right hand side, so that

$$f(\psi) = F(\psi^{-5/3} + \epsilon), \tag{3–33}$$

since this perturbation does not affect the leading order term in ψ. The paper goes on to investigate the consequences of this modification by means of a series solution of equation 3–13. The authors conclude that vorticity has a considerable effect on the separation efficiency of the hydrocyclone, with negative azimuthal vorticity at the inlet improving performance, despite decreasing the jetting effect of fluid down the hydrocyclone wall. The authors suggest that it is desirable to consider how the velocity profile at the inlet may be modified in order to exploit this phenomenon, by taking into account the secondary flows induced in pipe-work connecting hydrocyclones in arrays in field operation.

Brayshaw [12] also takes equation 3–13 as his starting point. In his paper however a wider variety of forms for the vorticity function $f(\psi)$ is investigated by means of numerical methods. However the form used by Bloor and Ingham was not compatible with the numerical method used, although the author concedes that this form is probably preferable. The solutions obtained for velocity profiles were shown to be in worse agreement with the experimental data of Kelsall than the analytical model of Bloor and Ingham.

The author develops a relationship between the vorticity distribution function $f(\psi)$ and the velocity distribution at an idealised toroidal (axisymmetric) inlet, thus making a link between the inlet boundary conditions and the separation efficiency of the hydrocyclone. Experimental work demonstrating the effects of different inlets on particle classification is also presented.

3.9 The central equation revisited: Part 2

In their most recent paper [8] Bloor and Ingham reconsider the use of equation 3–13, preferring on this occasion to start from equation 3–8. They comment that their previous

models, utilizing equation 3–13, were flawed by the assumption that all particles entering the hydrocyclone had identical angular momenta, thus allowing the term in Γ in 3–8 to be neglected. Recall that this was suggested by the experimental result that swirl velocity is a function of radial distance from the axis only, which is an observation valid for the main part of the hydrocyclone body and is unlikely to hold in the region near the inlet.

The inlet conditions in this paper are modelled with more care: the flow is assumed to enter the hydrocyclone in an axially symmetric fashion, with swirl velocity V_θ, axial velocity V_z directed into the hydrocyclone , and a radial velocity which is chosen in order to make the normal velocity vanish at the wall and keep $\mathcal{H}$, the total head as defined in equation 3–2 constant. These assumptions yield

$$\Gamma = R\sin\phi V_\theta \tag{3–34}$$

$$\psi = \frac{1}{2}V_z(r_0^2 - R^2\sin^2\phi) \tag{3–35}$$

where the constant of integration in the second equation has been chosen so as to make the stream function vanish on the hydrocyclone wall. Substituting these equations into equation 3–8 the equation

$$\frac{\partial^2\psi}{\partial R^2} + \frac{\sin\phi}{R^2}\frac{\partial}{\partial\phi}\left(\frac{1}{\sin\phi}\frac{\partial\psi}{\partial\phi}\right) = -\frac{V_\theta^2}{V_z} \tag{3–36}$$

is obtained.

This equation, in which V_θ and V_z are assumed to be constant, has a solution of the form

$$\psi = R^2F(\phi), \tag{3–37}$$

and substituting this in to 3–36 gives

$$\psi = \sigma\{[\csc^2\alpha^* + \ln(\frac{1}{2}\tan\alpha^*) - \csc\alpha^*\cot\alpha^*]\sin^2\phi - \sin^2\phi\ln(\frac{1}{2}\tan\phi) - 1\} \tag{3–38}$$

where $\sigma = -\frac{\pi r_0^2 v_\theta^2}{Qv_z}$ is a dimensionless constant. In the derivation of this equation it has been assumed that the stream line $\psi = 1$ just enters the vortex finder, and no flow (or negligible flow) goes to the underflow orifice, since the axial velocity V_z was not specified at the inlet. The swirl velocity may be found from the first of equations 3–34, showing that it has a modified free vortex form, and the other two components may be found from 3–38.

These results are then compared with experimental data from papers by Kelsall[4], and Knowles[13]. The agreement is quite good, notwithstanding the (unphysical) logarithmic singularity in the axial velocity profile at the axis, which is an anticipated failure of the inviscid model in this region.

3.10 Liquid-liquid hydrocyclones

Modelling liquid-liquid hydrocyclones (in particular those specialized for oil and water separation) requires extensions to the models of Bloor and Ingham previously presented for a number of reasons. In particular, it cannot be assumed that all the flow exits via the overflow of the hydrocyclone; a wider range of split ratios must be considered. Also, for separation of less-dense components, the region of flow near the axis may not be safely neglected, since the less dense component must be concentrated here. Also, the smaller density differences between the components in such hydrocyclones has led to the development of geometries which are quite different from solid-liquid separators, the former typically having a much smaller cone angle.

Recent work by Moraes *et al.*[14] extends the work of Bloor and Ingham to cover liquid-liquid hydrocyclones. Beginning with equation 3–13, in non-dimensional form, they propose a solution of the form $\psi = r^2 f(\phi) + G(\phi)$, which satisfies boundary conditions more appropriate to a small cone angle hydrocyclone. The boundary conditions used in this paper are

$$\begin{aligned} \psi_1 &= 0, \\ \psi_3 = \psi_4 &= -\frac{(1-f)Q}{2\pi} \\ \psi_2 - \psi_1 &= \frac{FQ}{2\pi}, \end{aligned}$$

where ψ_1 is the streamfunction at the hydrocyclone axis, ψ_2 is the streamfunction at the overflow pipe wall, and ψ_3 and ψ_4 are the streamfunctions at the hydrocyclone wall at the top and bottom respectively of the region of interest.

The solutions thus obtained are shown for various values of the split ratio F, and show a reversal of core flow for $F = 1\%$ which penetrates very little of the hydrocyclone body below the overflow. However, this is not an accurate reflection of the known behaviour of

slender geometry hydrocyclones. The assumptions initially made by Bloor and Ingham were that the fluid could be modelled as inviscid, so that their model describes the behaviour of the fluid away from the core, where solid body rotation is typical, and away from the hydrocyclone wall, where a viscous boundary layer will form. It is likely that the effects of these two viscous regions on the flow in a slender hydrocyclone geometry will be far more pronounced, and that continuing to neglect these effects is unwise in attempts to model these flows.

3.11 Concluding remarks

This section has presented, in bare outline, some of the analytical models of the hydrocyclone developed over a period of some years by Bloor and Ingham. The intention has been to indicate the methods found useful and the assumptions found necessary in such models. Their most recent papers on the subject [9, 8] demonstrate the importance of modelling the entry flow to the success of the model, and show a good fit with experimental data from different hydrocyclone geometries.

However, the models developed have some faults. The models of the core flow are primarily inviscid, and the axial region of reversed flow, which coincides with the forced vortex region in which viscous effects are important, is not well accounted for by such a model. The authors hold that the effect of this region on (dense) particle separation is not important. In the context of this writer's proposed study of de-watering hydrocyclones this assertion is unjustified: since the important component of the flow (the oil) is removed from the overflow, and the concentration of oil is highest in the recirculation zone it is precisely this region in which phase-inversion may be expected to occur. In this context Bloor and Ingham cite a study by Riley[15] on recirculation, in which the author concludes that it would be more efficient to solve the full Navier-Stokes equations in this region.

The models reviewed above also typically assume that all the flow exits the hydrocyclone via the overflow orifice, with a boundary layer of negligible volume flux carrying particles to the underflow, and that the volume fraction of the denser component is negligible. Neither of these assumptions are tenable for the de-watering hydrocyclone. The effect of a variable split ratio on the flow is not considered, and no predictions of pressure

drops across the hydrocyclone are made.

Chapter 4

Alternative Mathematical Models

4.1 Introduction

This chapter describes two mathematical models, originating with this author, which attempt to shed light on different aspects of the flow in a hydrocyclone. The common feature of these models is the use of analytical mathematical methods which means that they represent considerable simplifications of the flow. Nevertheless, it is the author's opinion that each model contributes to the understanding of the fundamental behaviour of fluid flow in a hydrocyclone.

4.1.1 Introduction

The analytical models of hydrocyclones reviewed in the previous chapter are all essentially descendents of [5]. However, the extension of this model to the case of the slender geometries typical in liquid-liquid hydrocyclones by Moraes, *et al.*[14] predicts that the reversal of flow in the hydrocyclone does not penetrate far into the body of device. As discussed in the preceding chapter, this is not the behaviour observed experimentally for these geometries, in which the reversed flow near the axis extends into the underflow outlet.

Accordingly, it seems appropriate to return to first principles and seek a new framework for a mathematical model of flow in a hydrocyclone. The model described in section 4.2 below is this author's attempt to develop such a model with the following advantages

over the models described in the previous chapter:

- It reproduces the qualitative behaviour of the flow field in a slender geometry hydrocyclone, including a core of reversed flow which extends for the full length of the conical section of the device.
- It models both the region of flow at the core where viscosity causes a forced vortex region and the free vortex structure of the flow outside the core.

This model also shares some limitations with previous analytical models of the hydrocyclone. Specifically:

- The effects of turbulence are neglected.
- Only single component flow is considered.
- Wall boundary layers are not considered.
- The cyclone geometry is simplified to a cone.

The second part of this chapter addresses some of the issues involved in constructing a mathematical model of a rotating two-component flow. (Note that no distinction is made in this thesis between a 'phase' and a 'component'. Since no thermodynamic phase transitions are discussed this should not cause any confusion.) There is no widely accepted practice for the computational modelling of engineering flows involving two inter-penetrating but immiscible continua.

It is neither practical nor desirable to track individual droplets, much as is the case with turbulent eddies. Again, as with turbulence modelling, an attempt is made to formulate a model using only 'averaged' quantities of engineering interest. This is done by introducing the continuously varying volume fractions which represent the probability (in some sense) of a point in space being occupied by each of the components. If α_1 is the volume fraction of oil, say, then the fact that $\alpha_1(\mathbf{p}) = 1$ at some position $\mathbf{p}$ in the flow field implies that this position is always occupied by oil. We require a volume fraction field for each component and require that their sum is unity at any given point in the flow-field.

Accordingly, for an oil/water hydrocyclone we would hope that the volume fraction of water was near one at the underflow exit, and that of oil was near one at the overflow.

The analogy between turbulent and two phase flow can be extended: since both involve a form of averaging of the equations, which corresponds to discarding some information, both of the resulting systems of equations need to be supplemented by closure laws in order to be mathematically and computationally tractable.

The well known k–ϵ turbulence model is widely accepted as suitable for many flows of engineering interest (although, as we shall see in subsequent chapters, it is not appropriate for hydrocyclones). For multi-component flows there is no such consensus of established practice in computational modelling.

The purpose of the model described in this chapter is to investigate a simple model of two phase flow in a disk, and to show that it is both mathematically well-formed and gives rise to the behaviour that physical intuition would predict. It thus represents a suitable starting point for the development of more elaborate two phase models, incorporating turbulence and interfacial effects.

4.2 Single phase flow in a hydrocyclone

4.2.1 The flow equations

We begin with the Navier-Stokes equations in cylindrical polar coordinates, (r,θ,z), with:

$$\mathbf{v} = v_r \mathbf{e}_r + v_\theta \mathbf{e}_\theta + v_z \mathbf{e}_z, \tag{4-1}$$

and assuming that the flow is axi-symmetric (i.e., none of the flow variables depends on θ) and viscous, but laminar, we have

$$\begin{aligned}
v_r \frac{\partial v_r}{\partial r} + v_z \frac{\partial v_r}{\partial z} - \frac{v_\theta^2}{r} &= -\frac{1}{\rho}\frac{\partial p}{\partial r} + \nu \left[\frac{\partial^2 v_r}{\partial r^2} + \frac{1}{r}\frac{\partial v_r}{\partial r} + \frac{\partial^2 v_r}{\partial z^2} - \frac{v_r}{r^2} \right] \\
v_r \frac{\partial v_\theta}{\partial r} + v_z \frac{\partial v_\theta}{\partial z} + \frac{v_r v_\theta}{r} &= \nu \left[\frac{\partial^2 v_\theta}{\partial r^2} + \frac{1}{r}\frac{\partial v_\theta}{\partial r} + \frac{\partial^2 v_\theta}{\partial z^2} - \frac{v_\theta}{r^2} \right] \\
v_r \frac{\partial v_z}{\partial r} + v_z \frac{\partial v_z}{\partial z} &= -\frac{1}{\rho}\frac{\partial p}{\partial z} + \nu \left[\frac{\partial^2 v_z}{\partial r^2} + \frac{1}{r}\frac{\partial v_z}{\partial r} + \frac{\partial^2 v_z}{\partial z^2} \right] \\
\frac{1}{r}\frac{\partial}{\partial r}(r v_r) + \frac{\partial v_z}{\partial z} &= 0
\end{aligned}$$

4.2.2 Non-dimensionalisation

We assume that the tangential velocity component will be larger than those in other directions. It is scaled with a 'typical' value V_θ. A typical value for the radial velocity component may then be defined as δV_θ, where $\delta << 1$. The slenderness of the hydrocyclone geometry suggests that the scalings for radial and vertical lengths should be different. We adopt scalings

$$r = r_0\hat{r}, z = z_0\hat{z}. \tag{4-2}$$

Substituting these into the continuity equation gives:

$$\frac{\delta V_\theta}{r_0}\frac{1}{\hat{r}}\frac{\partial(\hat{r}\hat{v}_r)}{\partial\hat{r}} + \frac{V_z}{z_0}\frac{\partial\hat{v}_z}{\partial\hat{z}} = 0, \tag{4-3}$$

where V_z is a scaling for v_z. For these to balance we require

$$V_z = \frac{z_0}{r_0}\delta V_\theta. \tag{4-4}$$

We define an aspect ratio parameter $\gamma = \frac{r_0}{z_0}$ and obtain $V_z = \frac{z_0}{r_0}V_\theta$. The hypothesis of strongly swirling flow (i.e., $V_z << V_\theta$) then suggests that $\delta << \gamma$.

It is useful here to rewrite the flow equations in terms of the variables ω_θ and ψ, as defined in chapter 3. The definition of ω_θ may be re-stated in terms of ψ as

$$\frac{\partial^2\psi}{\partial r^2} - \frac{1}{r}\frac{\partial\psi}{\partial r} + \gamma^2\frac{\partial^2\psi}{\partial r^2} = -r\omega_\theta, \tag{4-5}$$

dropping the use of hats for non-dimensional quantities. This may be rewritten as

$$\mathcal{D}\psi = -r\omega_\theta \tag{4-6}$$

where the operator $\mathcal{D}$ is defined by:

$$\mathcal{D} = r\frac{\partial}{\partial r}\left(\frac{1}{r}\frac{\partial}{\partial r}\right) + \gamma^2\frac{\partial^2}{\partial z^2}. \tag{4-7}$$

The equations for v_r and v_z may be combined to yield an equation for the transport of ω_θ.

$$\left(v_r\frac{\partial}{\partial r} + v_z\frac{\partial}{\partial z}\right)\frac{\omega_\theta}{r} = 2\frac{\gamma^2}{\delta^2}\frac{1}{r^2}v_\theta\frac{\partial v_\theta}{\partial z} + \frac{1}{r\delta Re}\left(\frac{\partial^2\omega_\theta}{\partial r^2} + \frac{1}{r}\frac{\partial\omega_\theta}{\partial r} - \frac{\omega_\theta}{r^2} + \gamma^2 pde^2\omega_\theta z^2\right). \tag{4-8}$$

We may also write a transport equation for Γ, defined as $\Gamma = rv_\theta$:

$$\left(v_r\frac{\partial}{\partial r} + v_z\frac{\partial}{\partial z}\right)\Gamma = \frac{1}{\delta Re}\left(\frac{\partial^2\Gamma}{\partial r^2} - \frac{1}{r}\frac{\partial\Gamma}{\partial r} + \gamma^2\frac{\partial^2\Gamma}{\partial z^2}\right). \tag{4-9}$$

We may eliminate ω_θ and v_θ from 4–8 and 4–9 in favour of Γ and ψ to obtain the equations

$$r\frac{\partial\psi}{\partial z}\frac{\partial}{\partial r}\left(\frac{\mathcal{D}\psi}{r^2}\right) - \frac{1}{r}\frac{\partial\psi}{\partial r}\frac{\partial}{\partial z}\mathcal{D}\psi = 2\frac{\Gamma}{r^2}\frac{\partial\Gamma}{\partial z} - \frac{\mathcal{D}^2\psi}{\delta Re} \tag{4–10}$$

and

$$\frac{1}{r}\left(\frac{\partial\psi}{\partial z}\frac{\partial\Gamma}{\partial r} - \frac{\partial\psi}{\partial r}\frac{\partial\Gamma}{\partial z}\right) = \frac{1}{Re\delta}\mathcal{D}\Gamma. \tag{4–11}$$

These equations may be simplified by a change of variable: we define $\mu = r^2$, and assume that Γ and ψ may be expanded in terms of δ^2. We also adopt the convention that $R = \delta Re$ is a more suitable Reynolds' number.

To leading order 4–10 becomes

$$\Gamma_0\frac{\partial\Gamma_0}{\partial z} = 0. \tag{4–12}$$

I.e., $\Gamma_0 = \Gamma_0(\mu)$, and equation 4–11 becomes

$$\frac{2\mu}{R}\frac{d^2\Gamma_0}{d\mu^2} + \frac{\partial\psi_0}{\partial z}\frac{d\Gamma_0}{d\mu} = 0 \tag{4–13}$$

It follows from 4–13 that ψ_0 is a linear function of z:

$$\psi_0 = A_0(\mu) + A_1(\mu)z \tag{4–14}$$

If we are able to specify stream functions $\Psi_0(\mu) = \psi_0(\mu, 0)$ and $\Psi_1(\mu) = \psi_0(\mu, 1)$ at $z = 0$ and $z = 1$, then we have

$$\psi_0 = \Psi_0(\mu) + (\Psi_1(\mu) - \Psi_0(\mu))z \tag{4–15}$$

Equation 4–13 then becomes

$$\frac{2\mu}{R}\frac{d^2\Gamma_0}{d\mu^2} + (\Psi_1(\mu) - \Psi_0(\mu))\frac{d\Gamma_0}{d\mu} = 0,$$

and the problem is reduced to an ordinary differential equation for Γ. This may readily be integrated to give

$$\frac{d\Gamma}{d\mu} = Ae^{-\frac{R}{2}\int\frac{\Delta\Psi}{\mu}d\mu},$$

where $\Delta\Psi = \Psi_1 - \Psi_0$

Equation 4–15 and the definition of ψ_0 imply that u_r is a function of r only, from which u_z may immediately be determined, by continuity.

Essentially the same conclusions, namely that the inviscid flow is determined by a function of one variable, and that radial velocity is independent of z, are reached by Davidson [16], in the context of electro-magnetically induced swirl flow in a molten metal cavity. That paper goes on to show how, in that case, the boundary conditions on the side-walls control the interior flow.

4.2.3 Boundary conditions

The boundary condition at the wall is straightforward; we require that Ψ is constant along the wall, or more accurately, it is constant just outside the wall boundary layer. We restrict our attention to a cone frustum, with $(r, z) = (1, 1)$ at the top, and $(r, z) = (0, a)$ at the bottom, where $a < 1$. By restricting attention to this domain, which does not include the top wall of the hydrocyclone, we avoid the need to model the top wall and overflow outlet of the hydrocyclone. It may be assumed that the bottom of our frustrum coincides with the underflow exit.

In order to satisfy this wall constraint we require that

$$\Psi_0 = (r - a)f(r)$$
$$\Psi_1 = (r - 1)f(r),$$

for some function $f(r)$.

This gives $\Delta\Psi = (a - 1)f(r)$, so that

$$\frac{d\Gamma}{d\mu} = Ae^{\frac{R}{2}(1-a)\int \frac{f(r)}{\mu}\,d\mu} \tag{4–16}$$

and

$$u_r = \frac{1 - a}{r} f(r). \tag{4–17}$$

However, the treatment of the hydrocyclone as a cone frustrum, so that the top wall is not modelled, means that boundary conditions at the top and bottom of our region are less straightforward to specify. We may in fact postulate a function $f(r)$ as a result of the simplification of our model. For simplicity, we may take $f(r)$ to be a polynomial in r; equation 4–17 suggests that the lowest order term in the polynomial should be of order r^2, which is analogous to the Burger's vortex.

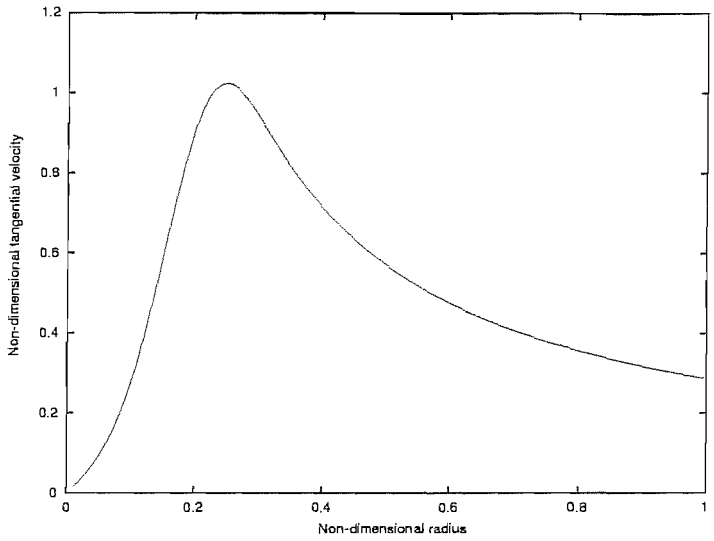

Figure 4.1: Calculated Tangential Velocities

The fact that the model described here neglects the top part of the hydrocyclone, including the top wall, means that we are free to pick any coefficients we wish for $f(r)$.

Taking $a = 1/4$, and $f(r) = a_2 r^2 + a_4 r^4$, with $a_2 = -5$, $a_4 = -500$, we obtain the streamlines shown in figure 4.2. These coefficients were chosen to give a flow qualitatively similar to that known to occur in a hydrocyclone.

The hydrocyclone in this picture is drawn lying sideways, with the axis of symmetry at the bottom of the picture, and the conical wall of the hydrocyclone sloping down and to the right. This figure shows that the axial reversal of flow extends to the base of the cone, although the apex of the cone is not included in the model; the flow reversal continues into the underflow exit, which is not included in this model. This matches the observed behaviour of the hydrocyclone better than the model of Moraes *et al.*

The tangential velocities as shown in figure 4.1 (which plots non-dimensional tangential velocity against radius) show the combined vortex structure described in section 3.1.2, with solid body rotation towards the core, and a free vortex beyond this. This is also an improvement on the model of Bloor and Ingham [5], and its successors, which assume inviscid flow and therefore predict only a free vortex, with a singularity at the axis.

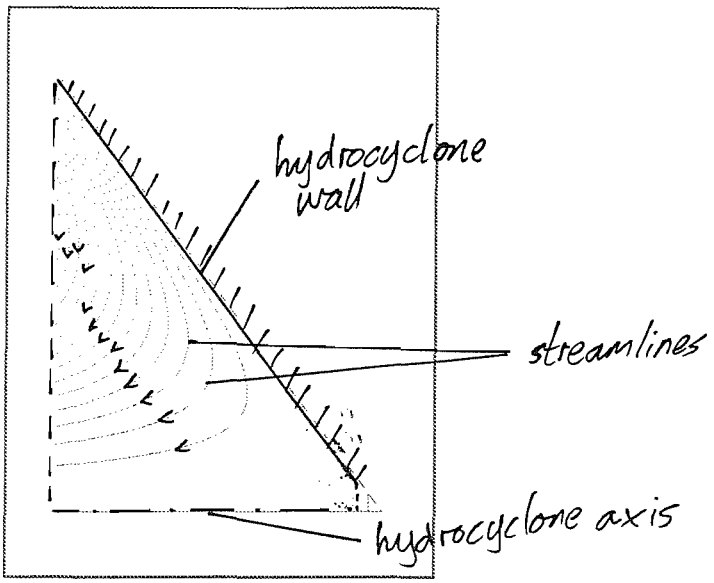

Figure 4.2: Calculated Streamfunctions

4.2.4 Conclusions

A model of a hydrocyclone in cylindrical polar coordinates using a Stoke's streamfunction and angular momentum as independent variables has been developed. Scalings which reflect natural assumptions about the flow in a hydrocyclone have been used to simplify the resulting equations, and a solution has been developed which both describes the axial region of reversed flow, and satisfies an inviscid wall condition, so that it could be matched to a wall boundary layer there.

The resulting model is shown to be a good fit to observed behaviour over more of the geometry of the hydrocyclone than its predecessors.

4.3 Two Phase Flow

4.3.1 Introduction

Although some of the models of hydrocyclones discussed in the previous chapter deal with particle flow, as do some of the computational models described in chapter 8, they all share the assumption that the dispersed phase is solid and dilute. Such problems may be approached by tracking individual particles, in a Lagrangian frame. For the regimes

of interest in this study, where high concentrations of the minor component are expected (at least in some regions of the hydrocyclone) this approach is not appropriate. Instead, it is desirable to model the flow as that of two inter-penetrating continua, each of which has a volume fraction (between 0 and 1) which denotes the probability of the each phase occupying a given point. Of course, in reality, at a given time in a given experiment, any point is either occupied by one component or the other, so the void fraction represents some form of average likelihood of finding a particular component at a specified point. The nature of the averaging which must be carried out to calculate these probabilities is subtle and is discussed at length in [17] and [18]. The averaging may be carried out over time, to yield a steady state flow, or over many runs of an experiment, to give an ensemble average. In the model described here it is assumed that the flow is axially symmetric; that is, that the values of the void fractions and other averaged values are independent of the angle θ.

The author is not aware of any studies of such models in the context of strongly swirling flows. In view of the complex nature of continuum models of two phase flows it was thought advisable to develop the theory in the simplest context which could preserve the fundamental properties of the flow in a hydrocyclone. Accordingly, a model of swirling flow in a disc is now described, and its properties investigated.

In this section we consider the flow of two components within a disk. This should be considered as an instructive model problem, which may highlight some of the essential features of two component rotating flow.

The work described in this section is original with the author. While this work is unlikely to lead directly to a realistic model of a hydrocyclone, it is nonetheless useful. Two phase flow problems are much less well understood mathematically than there single phase counterparts, to the point were there is not a even standard set of equations that is generally accepted. The goal of this section is to explore the consequences of a set of simple assumptions about rotating two phase flow. By treating the flow only in two dimensions the mathematics remains tractable, and the results show that the model developed is consistent with physical intuition.

This analysis justifies to some extent the use of similar assumptions in developing a computational model of the two component flow in a hydrocyclone. Such an extension is

described later in this thesis.

4.3.2 Constitutive Equations

Two component flows are more difficult to model than single component flows: it is possible to devise superficially plausible equations which are elliptic in time. This means that boundary conditions would be needed for both an initial time and a final time, to allow the model to predict the flow at intermediate times. This is clearly not a desirable property for a model: we wish to prescribe initial conditions, and predict the subsequent evolution of the flow. An attempt to do this with a model which is elliptic in the time dimension will cause instabilities in the solution: small changes in the initial conditions will grow without bound, rendering the model useless for prediction. Fitt [17] discusses how such equations can arise for apparently plausible models of two component flow in a pipe.

Accordingly we propose here a simple model, and check that its behaviour fits our expectations of such a system. In order to keep the model simple we neglect such factors as turbulence and viscosity, other than its role in causing a drag force, of a form we need not specify initially, between the two components.

We propose continuity equations of the form,

$$\frac{\partial(\alpha_i\rho_i)}{\partial t} + \nabla.(\alpha_i\rho_i\mathbf{v}_i) = 0 \tag{4–18}$$

where ρ denotes density, α volume fraction, $\mathbf{v} = v_r\mathbf{e}_r v_\theta\mathbf{e}_\theta$ and i is used as a generic subscript which may take the values 1 and 2 to specialize equations to a particular component.

In the case of two dimensional axisymmetric flow in a disk equation 4–18 reduces to

$$\frac{\partial(\alpha_i\rho_i)}{\partial t} + \frac{\partial(\alpha_i\rho_i v_{r_i})}{\partial r} + \frac{1}{r}(\alpha_i\rho_i v_{r_i}) = 0, \tag{4–19}$$

In this model we assume that the pressures in the two components are equal; an assumption which fails to yield a hyperbolic system of equations for simple pipe flows [17], but which we shall see succeeds in this case.

The momentum equation for each component is

$$\frac{\partial}{\partial t}\rho_i\alpha_i\mathbf{v}_i + \mathbf{v}_i.\nabla(\rho_i\alpha_i\mathbf{v}_i) = -\alpha_i\nabla p + (-1)^i\mathbf{F}, \tag{4–20}$$

where $\mathbf{F}$ is the drag force resulting from the motion of a droplet of one component moving through the other component. Newton's third law requires that this force be of equal magnitude for the two components, but of opposite direction.

In the case of this model the momentum equation reduces to

$$\frac{\partial(\alpha_i v_{r_i})}{\partial t} + v_{r_i}\frac{\partial(\alpha_i v_{r_i})}{\partial r} - \frac{v_{\theta_i}^2}{r} = -\frac{\alpha_i}{\rho_i}\frac{\partial p}{\partial r} + \frac{(-1)^i}{\rho_i}\mathbf{F}.\mathbf{e}_r \tag{4–21}$$

$$\frac{\partial(\alpha_i v_{\theta_i})}{\partial t} + v_{r_i}\frac{\partial(\alpha_i v_{\theta_i})}{\partial r} + \alpha_i\frac{v_{r_i}v_{\theta_i}}{r} = \frac{(-1)^i}{\rho_i}\mathbf{F}.\mathbf{e}_\theta. \tag{4–22}$$

We may use the continuity equations to simplify equations 4–21 and 4–22:

$$\frac{\partial \alpha_i v_{r_i}}{\partial t} - \alpha_i\frac{(v_{r_i}^2 + v_{\theta_i}^2)}{r} = = -\alpha_i\frac{1}{\rho_i}\frac{\partial p}{\partial r} + (-1)^i + \frac{(-1)^i}{\rho_i}\mathbf{F}.\mathbf{e}_r \tag{4–23}$$

$$\alpha_i\frac{\partial v_{\theta_i}}{\partial t} + v_{r_i}\alpha_i\frac{\partial v_{\theta_i}}{\partial r} = \frac{(-1)^i}{\rho_i}\mathbf{F}.\mathbf{e}_\theta \tag{4–24}$$

We now wish to assess whether this system is hyperbolic in the time direction, since, as discussed above, this is a prerequisite for a model which can be allowed to evolve from initial conditions. To establish this we rewrite the above equations in the form

$$A\frac{\partial \mathbf{v}}{\partial t} + B\frac{\partial \mathbf{v}}{\partial r} = C, \tag{4–25}$$

where

$$\mathbf{v} = (\alpha_1, v_{r_1}, v_{\theta_1}, v_{r_2}, v_{\theta_2}, p)^T \tag{4–26}$$

and

$$A = \begin{pmatrix} 1 & 0 & 0 & 0 & 0 & 0 \\ -1 & 0 & 0 & 0 & 0 & 0 \\ 0 & \alpha_1 & 0 & 0 & 0 & 0 \\ 0 & 0 & \alpha_1 & 0 & 0 & 0 \\ 0 & 0 & 0 & \alpha_2 & 0 & 0 \\ 0 & 0 & 0 & 0 & \alpha_2 & 0 \end{pmatrix} \tag{4–27}$$

and

$$B = \begin{pmatrix} v_{r_1} & \alpha_1 & 0 & 0 & 0 & 0 \\ -v_{r_2} & 0 & 0 & \alpha_2 & 0 & 0 \\ 0 & \alpha_1 v_{r_1} & 0 & 0 & 0 & \frac{\alpha_1}{\rho_1} \\ 0 & 0 & \alpha_1 v_{r_1} & 0 & 0 & 0 \\ 0 & 0 & 0 & \alpha_2 v_{r_2} & 0 & \frac{\alpha_2}{\rho_2} \\ 0 & 0 & 0 & 0 & \alpha_2 v_{r_2} & 0 \end{pmatrix}. \tag{4–28}$$

The question of hyperbolicity is simply that of whether the matrix $|B - \lambda A| = 0$ has only real solutions for λ. With systems such as this it is preferable to carry out the computation with a symbolic manipulation system such as MAPLE. It transpires that the characteristic values of the system are v_{r_1}, v_{r_2} and $\alpha_2 v_{r_1} + \alpha_1 v_{r_2}$.

4.3.3 Steady State Solutions

Having shown that the assumption of a single pressure field allows the evolution of the flow with time to be modelled, and is thus physically realistic, we may now restrict attention to steady flows, and attempt to find solutions to these equations.

In the steady state situation the continuity equation reduces to

$$\frac{1}{r}\frac{\partial}{\partial r}(r\alpha_i v_{r_i}) = 0, \tag{4–29}$$

from which we conclude that $u_{r_i} = 0$, since this must be the case at $r = 0$. The momentum equations reduce to

$$-\frac{v_{\theta_i}^2}{r} = -\alpha_i \frac{1}{\rho_i}\frac{\partial p}{\partial r} + \frac{(-1)^i}{\rho}\mathbf{F}.\mathbf{e}_r \tag{4–30}$$

$$0 = \mathbf{F}.\mathbf{e}_\theta. \tag{4–31}$$

If we assume that the drag force is of the form

$$\mathbf{F} = k|\mathbf{v}_1 - \mathbf{v}_2|(\mathbf{v}_1 - \mathbf{v}_2), \tag{4–32}$$

then it follows that, since $v_{r_1} = v_{r_2} = 0$, $\mathbf{F}.\mathbf{e}_r = 0$. Then equation 4–31 implies that $v_{\theta_1} = v_{\theta_2}$. Equation 4–30 then implies that if α_1 and α_2 are non-zero at a given position in the flow that

$$\rho_1 v_{\theta_1}^2 = \rho_2 v_{\theta_2}^2, \tag{4–33}$$

but since $v_{\theta_1} = v_{\theta_2}$ this implies $\rho_1 = \rho_2$, which contradicts our assumptions about the two components of the flow.

We conclude, therefore, that the only possible steady-state solutions for two component flow in a disk are those which consist of separate annular rings of the two components. In other words the two components do not mix, but stratify into layers. We anticipate that the only steady state solution that would be observed in practice would have the

denser fluid at the outside of the cylinder, and the less dense fluid at the core with a sharp interface between them. We have established that the interfaces will be sharp; to complete our model we must investigate the stability of the solutions we have found.

4.3.4 Stability Analysis

We now consider the stability of these solutions to small perturbations which may vary in time and space. Only solutions in which small perturbations die away can be expected to be observed in practice. Since the perturbations we consider need not be time-independent or axisymmetric we must return to the consideration of the full non-axisymmetric, time-dependent equations, for each of the components separately.

$$\frac{\partial v_{r_1}}{\partial t} + v_{r_1}\frac{\partial v_{r_1}}{\partial r} + \frac{v_{\theta_1}}{r}\frac{\partial v_{r_1}}{\partial \theta} - \frac{v_{\theta_1}^2}{r} = -\frac{1}{\rho_1}\frac{\partial p_1}{\partial r} \tag{4–34}$$

$$\frac{\partial v_{r_1}}{\partial t} + v_{r_1}\frac{\partial v_{\theta_1}}{\partial r} + \frac{v_{\theta_1}}{r}\frac{\partial v_{\theta_1}}{\partial \theta} - \frac{v_{\theta_1}v_{r_1}}{r} = -\frac{1}{\rho_1}\frac{1}{r}\frac{\partial p_1}{\partial \theta} \tag{4–35}$$

$$\frac{\partial v_{r_1}}{\partial r} + \frac{v_{r_1}}{r} + \frac{1}{r}\frac{\partial v_{\theta_1}}{\partial \theta} = 0 \tag{4–36}$$

$$\frac{\partial v_{r_2}}{\partial t} + v_{r_2}\frac{\partial v_{r_2}}{\partial r} + \frac{v_{\theta_2}}{r}\frac{\partial v_{r_2}}{\partial \theta} - \frac{v_{\theta_2}^2}{r} = -\frac{1}{\rho_2}\frac{\partial p_2}{\partial r} \tag{4–37}$$

$$\frac{\partial v_{r_2}}{\partial t} + v_{r_2}\frac{\partial v_{\theta_2}}{\partial r} + \frac{v_{\theta_2}}{r}\frac{\partial v_{\theta_2}}{\partial \theta} - \frac{v_{\theta_2}v_{r_2}}{r} = -\frac{1}{\rho_2}\frac{1}{r}\frac{\partial p_2}{\partial \theta} \tag{4–38}$$

$$u_{1,r} + \frac{v_{r_2}}{r} + \frac{1}{r}\frac{\partial v_{\theta_2}}{\partial \theta} = 0 \tag{4–39}$$

Now we consider small perturbations from the steady state:

$$v_{r_1} = 0 + \epsilon V_{r_1} \tag{4–40}$$

$$v_{\theta_1} = \bar{v}_{\theta_1} + \epsilon V_{\theta_1} \tag{4–41}$$

$$p_1 = \bar{p_1} + \epsilon P_1, \tag{4–42}$$

where ϵ is assumed to be small, so that terms of second order or higher in ϵ may be neglected in the following analysis.

Substituting these into the above equations we obtain, on considering the $O(\epsilon)$ system,

$$\frac{\partial V_{r_1}}{\partial t} + \frac{\bar{v}_{\theta_1}}{r}\frac{\partial V_{r_1}}{\partial \theta} - 2\frac{\bar{v}_{\theta_1}V_{\theta_1}}{r} = -\frac{1}{\rho_1}\frac{\partial P_1}{\partial r} \tag{4–43}$$

$$\frac{\partial V_{\theta_1}}{\partial t} + V_{r_1}\frac{\partial \bar{v}_{\theta_1}}{\partial r} + \frac{1}{r}\bar{v}_{\theta_1}\frac{\partial V_{\theta_1}}{\partial \theta} + \frac{V_{r_1}\bar{v}_{\theta_1}}{r} = -\frac{1}{\rho_1 r}\frac{\partial P_1}{\partial \theta} \tag{4-44}$$

$$\frac{\partial V_{r_1}}{\partial r} + \frac{V_{r_1}}{r} + \frac{1}{r}\frac{\partial v_{\theta_1}}{\partial \theta} = 0, \tag{4-45}$$

and similarly for the other component:

$$\frac{\partial V_{r_2}}{\partial t} + \frac{\bar{v}_{\theta_2}}{r}\frac{\partial V_{r_2}}{\partial \theta} - 2\frac{\bar{v}_{\theta_2}V_{\theta_2}}{r} = -\frac{1}{\rho_2}\frac{\partial P_2}{\partial r} \tag{4-46}$$

$$\frac{\partial V_{\theta_2}}{\partial t} + V_{r_2}\frac{\partial \bar{v}_{\theta_2}}{\partial r} + \frac{1}{r}\bar{v}_{\theta_2}\frac{\partial V_{\theta_2}}{\partial \theta} + \frac{V_{r_2}\bar{v}_{\theta_2}}{r} = -\frac{1}{\rho_2 r}\frac{\partial P_2}{\partial \theta} \tag{4-47}$$

$$\frac{\partial V_{r_2}}{\partial r} + \frac{V_{r_2}}{r} + \frac{1}{r}\frac{\partial v_{\theta_2}}{\partial \theta} = 0, \tag{4-48}$$

Now, suppose disturbances are of the form

$$F = F(r)e^{i(k\theta-\omega t)}, \tag{4-49}$$

where F denotes any of the capitalized quantities in the above equations. Any periodic disturbance can be written in this form by taking the Fourier transform of its angular component.

Then we have

$$-i\omega V_{r_1} + ik\frac{\bar{v}_{\theta_1}V_{r_1}}{r} - 2\frac{\bar{v}_{\theta_1}V_{\theta_1}}{r} = -\frac{P_1'}{\rho_1} \tag{4-50}$$

$$-i\omega V_{\theta_1} + V_{r_1}\frac{\partial \bar{v}_{\theta_1}}{\partial r} + ik\frac{V_{\theta_1}\bar{v}_{\theta_1}}{r} + \frac{V_{r_1}\bar{v}_{\theta_1}}{r} = -ik\frac{P_1}{\rho_1 r} \tag{4-51}$$

$$\frac{dV_{r_1}}{dr} + \frac{V_{r_1}}{r} + ik\frac{V_{\theta_1}}{r} = 0, \tag{4-52}$$

The continuity equation for component 1 may be rewritten to give V_{θ_1} in terms of V_{r_1} and its derivative:

$$V_{\theta_1} = \frac{i}{k}r\frac{dV_{r_1}}{dr} + \frac{i}{k}V_{r_1}. \tag{4-53}$$

Substituting this into the θ momentum equation gives:

$$\left(\frac{w}{k}r - \bar{v_{\theta_1}}\right)\frac{dV_{r_1}}{dr} + \left(\frac{w}{k} + \bar{v}_{\theta_1}\right) = -\frac{ikP_1}{\rho_1 r}. \tag{4-54}$$

By differentiating the r momentum equation and equating the pressure terms we have:

$$\frac{w}{k}(r^2\frac{d^2V_{r_1}}{dr^2}+3rV_{r_1}+(1-k^2)V_{r_1})+V_{r_1}\frac{\partial \bar{v}_{\theta_1}}{\partial r}+rV_{r_1}\frac{d^2\bar{v}_{\theta_1}}{dr^2} = \bar{v}_{\theta_1}\left(r\frac{d^2V_{r_1}}{dr^2} + 3\frac{dV_{r_1}}{dr} + (2-k^2)V_{r_1}\right). \tag{4-55}$$

To continue with this analysis we need to make some assumption about the form of the time-averaged azimuthal velocity $\bar{v}_{\theta_1}$. This is necessary since we neglected the effects of viscosity within each component, so that there is no shear between different rings of fluid. For simplicity we assume that we have solid body rotation, i.e., $\bar{v}_{\theta_1} = A_1 r$ for some constant A_1. Then equation 4–55 reduces to

$$\frac{w}{k}(r^2\frac{d^2V_{r_1}}{dr^2} + 3r\frac{dV_{r_1}}{dr} + (1-k^2)V_{r_1}) = A_1(r\frac{d^2V_{r_1}}{dr^2} - 3\frac{dV_{r_1}}{dr} + (1-k^2)V_{r_1}). \tag{4–56}$$

This is an Euler equation whose indicial equation is

$$\alpha(\alpha-1) + 3\alpha + (1-k^2) = 0, \tag{4–57}$$

which has solutions $\alpha = -1 \pm k$. Thus $V_{r_1} = C_1 r^{-1+k} + D_1 r^{-1-k}$. We may argue by symmetry that $V_{r_2} = C_2 r^{-1+k} + D_2 r^{-1-k}$.

We now need to use the interface conditions:

$$\frac{\partial \omega_\theta}{\partial t} + \frac{v_{\theta_i}}{r} - u_{r_i} = 0, \tag{4–58}$$

on $r = \omega_\theta = R + \epsilon H$ (the interface) for $i = 1, 2$. A third interface condition can be derived from the assumption that the pressures in the two components match at the interface.

$$p_1|_R + \epsilon H \left.\frac{\partial p_1}{\partial r}\right|^r = p_2|_R + \epsilon H \left.\frac{\partial p_2}{\partial r}\right|^r \tag{4–59}$$

at $r = R + \epsilon H$.

To first order this implies that $\bar{p_1}|_R = \bar{p_2}|_R$. We may eliminate pressure by the use of the θ momentum equations and obtain

$$\begin{aligned} &\rho_1\left(\tfrac{\omega}{k}V_{\theta_1} + 2iV_{r_1}A_1 - A_1V_{\theta_1}\right) \\ &-\rho_2\left(\tfrac{\omega}{k}V_{\theta_2} + 2iV_{r_2}A_2 - A_2V_{\theta_2}\right) \\ &+H(\rho_1A_1^2 - \rho_2A_2^2 i) = 0, \end{aligned} \tag{4–60}$$

while equation 4–58 becomes

$$-i\omega H - V_{r_i} + A_i ikH = 0, \tag{4–61}$$

for $i = 1, 2$. Now, the solutions

$$U_{r_i} = C_i r^{-1+k} + D_1 r^{-1-k}, \tag{4–62}$$

where component 1 is assumed to be within component 2 are only bounded at $r = 0, \infty$ if $V_{r_1} = C_1 r^{-1+k}$ and $V_{r_2} = C_2 r^{-1-k}$, where the expression for V_{r_1} requires that $k > 1$. Substituting these into equations 4–62 gives

$$-i\omega H + A_1 ikH - C_1 R^{-1+k} = 0 \tag{4–63}$$

$$-i\omega H + A_2 ikH - D_1 R^{-1-k} = 0. \tag{4–64}$$

From the continuity equation

$$\frac{dV_{r_i}}{dr} + \frac{V_{r_i}}{r} + \frac{ikV_{\theta_i}}{r} = 0 \tag{4–65}$$

we obtain

$$V_{\theta_1} = C_1 i r^{k-1} \tag{4–66}$$

$$V_{\theta_2} = -D_2 i r^{-1-k}. \tag{4–67}$$

Substituting these into equation 4–62 gives

$$\begin{aligned} &C_1\rho_1 R^{-1+k}(\omega + 2A_1 - A_1 k) \\ &+D_1\rho_2 i R^{-1-k}(\omega - 2A_2 - A_2 k) \\ &+kH(\rho_1 A_1^2 - \rho_2 A_2^2) = 0. \end{aligned} \tag{4–68}$$

For non-trivial solutions of equations 4–63 and 4–68 we require that

$$\begin{vmatrix} -R^{-1+k} & 0 & ikA_1 - i\omega \\ 0 & -R^{-1+k} & ikA_2 - i\omega \\ \rho_1 i R^{-1+k}(\omega + 2A_1 - A_1 k) & \rho_2 i R^{-1-k}(\omega - 2A_1 - A_1 k) & k(\rho_1 A_1^2 - \rho_2 A_2^2) \end{vmatrix} = 0 \tag{4–69}$$

Evaluating this determinant (with the use of the symbolic manipulation program MAPLE) gives rise to a quadratic equation in ω. For stability we require that the discriminant of this quadratic be positive, i.e.,

$$(\rho_1 + \rho_2)[(k+1)A_2^2\rho_2 - A_1^2(k-1)\rho_1] \geq \rho_1\rho_2((k+1)A_2 - (k-1)A_1)^2. \tag{4–70}$$

If $A_1 = A_2$ then we need

$$k(\rho_2^2 - \rho_1^2) + (\rho_1 - \rho_2)^2 \geq 0, \tag{4–71}$$

which is always true for $\rho_2 > \rho_1$ and fails for large values of k if $\rho_1 > \rho_2$. This means that perturbations with small wavelengths, k, will grow with time, so that the solution is unstable. In other words, the only stable solutions are those with the denser fluid at the outside of the disc surrounding the less dense fluid, with a clear demarcation between the two fluids. This is exactly what physical intuition would lead us to expect.

4.3.5 Conclusions

These results are heartening, even if it is unlikely that a model such as this can be developed analytically into a more complete hydrocyclone model, they do show that a simple two component model can give reasonable answers qualitatively.

It has been shown that the assumption that the pressures of the two phases are equal, while somewhat unphysical, leads to a well-posed (hyperbolic) system of equations for flow in a disk. This is not the case for one-dimensional flow in a pipe [17], and is a welcome development.

Further, the only steady axisymmetric solutions are those where the two phases occur in disjoint concentric rings. Making the further simplifying assumption that the annular rings are rotating in a the manner of a forced vortex it has been shown that the only stable solutions are those with the denser phase at the outside of the disk. It is not clear whether this result can be generalised to other tangential velocity distributions.

These results are not remarkable in the insight they convey about the likely behaviour of the flow in a disk; they serve rather to strengthen our confidence that the model proposed does indeed capture some of the expected behavior of the flow. This augurs well for the application of relatively simple models to more complex swirling flows.

Chapter 5

Electrical Impedance Tomography

5.1 Background to Experimental Work

The flow within a hydrocyclone, as discussed in the preceding chapters, is complex, and there would be little justification for accepting the predictions of a CFD model without some form of verification. Visual observation of phase concentrations within the hydrocyclone is not feasible, owing to the relative opacity of oil. Attempts to measure these phase concentrations by intrusive techniques would alter the flow within the hydrocyclone, and invalidate any measurements taken. The difference in conductivities between kerosene and brine (the two components to be used in the author's work) is large (a factor of 10^7). It is therefore reasonable to suppose that this difference may be exploited, and non-intrusive electrical measurements may yield some insight into the phase concentrations within the hydrocyclone.

A preliminary study [19], to be discussed more fully in section 5.3, established that measurements of electrical impedance did vary with concentrations of brine and oil within the hydrocyclone.

Accordingly an experimental programme was planned, in which the techniques of electrical impedance tomography were to be developed to provide information about the behaviour of the flow in a dewatering hydrocyclone.

5.2 Electrical Impedance Tomography

The general process of reconstructing the image of a plane section through a body via non-intrusive measurements is known as tomography, and the particular variant discussed in this chapter is called electrical impedance tomography. Much of the early work on this subject was carried out in order to make use of the technique as a diagnostic tool for medical purposes. An overview of this field of application is given in [20]. However, a Process Tomography Group has been established at UMIST, precisely for the purpose of applying this technology to industrial processes. To a large extent this chapter is built on foundations laid by this group.

In electrical impedance tomography (henceforth referred to as EIT), measurements of electrical properties at the perimeter of a vessel are made, and these are used to reconstruct a picture of electrical conductivity over a cross-section through the vessel. It is then possible to infer the composition across this plane, given a suitable relationship between volume fractions of each of the components within the vessel and the resulting local effective resistivity.

5.3 Electrode Configuration

A study by Thew and Becker [19] showed that along the conical wall of a brine-filled hydrocyclone,

$$\text{impedance} \propto (\text{distance})^{-0.2}.$$

This counter-intuitive result is thought to be a consequence of the 'electric double layer' formed at the electrodes (for details of this effect the reader is referred to Atkins [21]). This effect is one example of the general effect known as 'contact impedance', and Dickin et al. [22] suggest a way of circumventing it, which they refer to as the 'four electrode adjacent pair measurement protocol'. In this method current is passed between a pair of adjacent electrodes, and the voltage measured between a different adjacent pair of electrodes, where all adjacent pairs of electrodes have the same distance between them.

This protocol was not followed in [19], making the results presented there difficult to interpret. The resolution of the image which can be obtained using this technique

increases as the number of electrodes used is increased. However, using more electrodes also makes the task of image reconstruction more difficult. Dickin et al. [22] recommend the use of 16 or 32 electrodes evenly spaced around the circumference of the vessel. It is stated in [23] that some image reconstruction algorithms will not work with too few measurements.

Accordingly, the four electrode protocol was used throughout the experimental work described here. However limitations of space around the test vessel meant that only twelve electrodes could be fitted. Full details of the experimental equipment are given in section 5.3.2

5.3.1 Real time data acquisition

The experimental rig used by Dickin et al. included a digital voltage generator, which was found to be more flexible and accurate than analogue alternatives and a dedicated 8-bit processor for analogue to digital conversion of the resulting data. This latter retained the data in a battery operated memory unit and passed it via an RS232 serial link to the computer used for data processing when required. As mentioned above 16 equally spaced electrodes were used in their experiments, yielding 104 (= 16*13/2, since the roles of injecting and measurement electrodes are symmetric) separate measurements of potential drop between electrode pairs.

The data-gathering potential of this equipment recommended by Dickin et al. is of the order of 1000 frames per second. This vastly exceeds the possible rate of interpreting the data, owing to the computational requirements of this stage.

5.3.2 Equipment

The experiments described here were performed using a flow rate of 40 litres per minute with various concentrations of oil and water. The brine was pumped through the rig using compressed air, while a centrifugal pump was used to pump the oil. The components flow through separate flow meters and are mixed using a centrifugal pump running at 1000 rpm.

The combined flow was then run through a cylindrical duct with an internal diameter

of two inches (5.08cm), with twelve equally spaced 4 mm stainless steel screws mounted on a plane perpendicular to the axis of the duct.

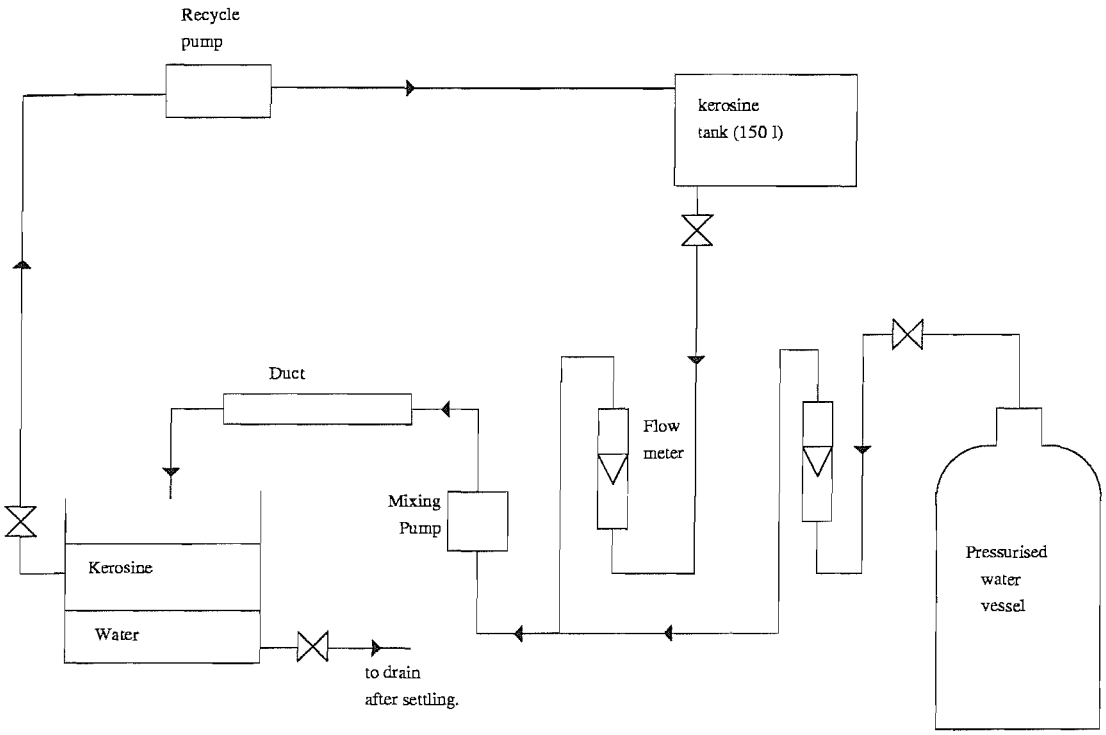

Figure 5.1: The Tomography Rig

Figure 5.1 shows the hydraulic aspects of the rig.

A Churchill Wave monitor generating a current independent peak output of 950 mV alternating current was used as a current injection source. This wave meter is capable of generating a square wave signal at several different frequencies. The frequency chosen was 10 KHz, after discussion with Professor Williams of the Camborne School of Mines. It is a source of concern that the peak output of the wave monitor may be too low, given the minimum level of potential difference measurable with the voltmeter used. Current was injected at two adjacent screws, and voltage measurements were taken at all adjacent pairs of electrodes.

The voltmeter used in these experiments was a Datron 1065 digital multi-meter, capable of measuring voltages in tens of a microvolt. It is necessary to be able to make voltage measurements over a wide dynamic range — from $O(10^1)$ to $O(10^{-4})$ volts. The amplifier used should be capable of a high level of common mode rejection, since the signal the voltage measuring electrodes share would otherwise drown out the differences between them. The Datron multi-meter claims to have common mode rejection of over

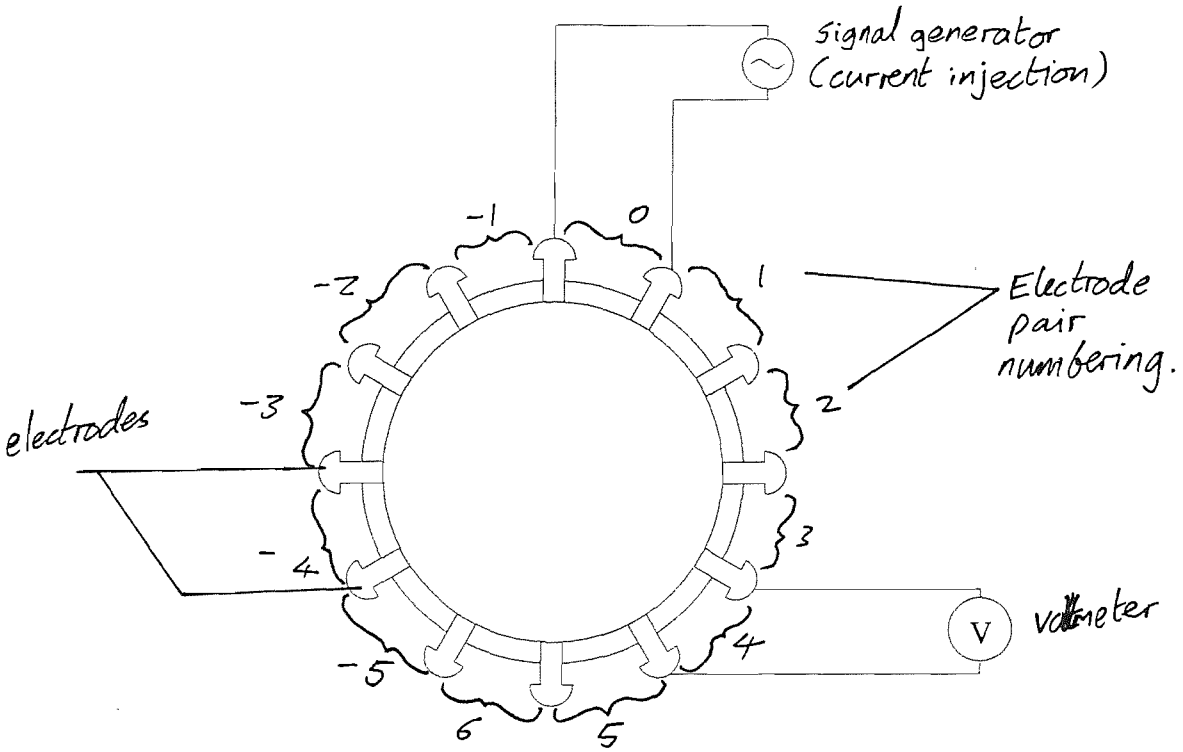

Figure 5.2: Electrical Aspects of the Rig

90dB for signals between direct current and 60Hz. Ideally one would like the voltmeter to have a very short response time, so that $n(n-1)/2$ measurements can be taken sufficiently rapidly to form a snapshot of the flow in the vessel. This is not possible with the Datron multi-meter; a settling time of less than half a second is claimed. In practice, however, it was often considerable longer. In these experiments, however, the lack of high speed multiplexing, and the assumption that the flow was in a steady state made this feature less important.

A schematic view of the electrical measurement equipment used is shown in figure 5.2.

5.3.3 Experimental methodology

To improve conductivity of water a 2% by weight solution of salt (NaCl) was used. The salt was measured in a bucket, and mixed into the water in a tank and allowed to dissolve before being pumped into the pressure vessel.

Initially the rig was run with oil in a loop through the coalescer (to remove water). During this process the voltage across a pair of measurement electrodes was observed to decrease considerably, presumably as small water droplets were removed. The appearance of the fluid would also clear to a translucent amber from a muddy brown.

The oil flow rate was adjusted to give the desired total flow rate and the electrical measurements taken, then oil flow rate decreased and water flow rate increased in increments of 5 l/min.

5.4 Initial Difficulties

An initial problem with this configuration was the difficulty in obtaining an adequate signal to noise ratio: e.g. compared with a typical Wave Monitor output voltage of 143 mV, 'noise' values (i.e., a potential difference measured between two adjacent electrodes with no current injection from the Wave Monitor) of between 5 and 15 mV made any attempts at reconstruction futile.

Subsequently it was noticed that the Wave Monitor gave different peak outputs on different channels, and that the highest (947 mV on Channel 3) gave much improved signal to noise ratios.

However, the most significant reductions in noise came from re-mounting the duct vertically. It transpired that some oil had remained trapped at the top of the duct while it was mounted horizontally, and that the low flow rates used up to this point (approximately 10 l/min) were insufficient to clear this oil film, whose adherence to the electrodes appears to have been the major cause of this problem. A higher flow rate of 40 litres per minute was also adopted.

A policy was subsequently adopted of running pure brine through the rig at the end of an experimental run, in order to prevent oil contamination of the electrodes, and to avoid oil-water interfaces other than in the run-off tank which might promote the formation of an emulsion.

5.4.1 Voltage Measurements

This section presents some data from the tomographic process.

Electrode Pair	ΔV (mV) Run number			
	1	2	3	4
-5	1.87	2.25	22	50
-4	2.45	3.2	44	15.7
-3	2.7	14.7	24	12
-2	11.9	5.4	116	27
-1	253	240	340	290
0	947.8	947	948	947.3
1	659	678	460	320
2	12.3	9.1	190	85
3	5.2	5.3	4.6	17
4	2.9	3.0	172	35
5	2.4	2.52	12	16
6	2.3	2.44	18	20

Table 5.1: Electrical measurements from a tomographic study of a cylindrical duct

Table 5.1 shows electrical measurements made for a variety of flow rates and concentrations of oil and water. The conditions for each run are summarized in table 5.2. In each case the current injection electrodes form the pair labelled 0 in table 5.1 and the other pairs of electrodes are numbered relative to this pair.

We would have expected that the voltage measurements should not depend on the conductivity of the mixture, until the volume fraction of oil was high enough to block any electrical measurements. We would also expect that the voltage measurements should be symmetric. Neither of these suppositions would appear to be accurate. It is not surprising that the measurements in the case of pure oil give wayward results: pure oil is highly resistive, and the currents passed through it are likely to be sufficiently low to cause measurement difficulties. It is possible that capacitative effects are relevant here, and also that the electrodes became contaminated with oil, or were fixed into the duct in such a way that a fluid could be trapped in the cavity. The discrepancy between results

Run	Q_{total} (l/min)	Q_{oil} (l/min)	Q_{water} l/min
1	40	20	20
2	50	25	25
3	40	40	0
4	40	35	5

Table 5.2: Case details

for electrode pairs 1 and -1 is particularly disturbing, and no explanation has been found for this.

5.4.2 Current Measurements

In the light of the somewhat disappointing results for voltage measurements, it is heartening to have more positive results for current measurements. These are, in effect, measurements of bulk conductivity of the flow. The minimum flow-rate of oil that could be measured was 15 l/s, while the maximum flow-rate of brine that could be produced was a little over 30 l/s. Conductivities were measured at three total flow-rates: 20, 30 and 40 l/min, with 5 l/min increments in the water and oil flow rates.

These results, given in table 5.3, show the expected behaviour: the current drops off exponentially as the oil concentration increases.

These results are plotted in figure 5.3. The current is plotted on a logarithmic scale, against the volume fraction of oil, and it may be seen that the results for different flow rates collapse onto a single curve. For volume fractions of oil less than 0.6 the measured current stays in the milliamp range, while above this value there is a rapid jump to microamps, as the oil component becomes continuous and acts as an insulator. This means that any attempt to use tomographic measurements to determine local conductivities use current measurements accurate over a large range of values. It is clear from this result that varying the global concentration of oil has a dramatic effect on the electrical properties of the mixture. It follows from this that with more data-capture methods capable of a larger number of more accurate measurements than was possible in this study electrical

Q_{total} l/min	Q_{oil} l/min	Q_{water} l/min	I_{inj} mA
40	40	0	7.0e-3
40	35	5	10.2e-3
40	30	10	54e-03
40	25	15	2.58
40	20	20	3.19
40	15	25	3.91
34	0	34	4.85
30	30	0	5.5e-03
30	25	5	70e-3
30	20	10	90e-03
30	15	15	3.04
30	0	30	4.36
20	15	5	76e-3
20	0	20	4.38

Table 5.3: Current measurements for a variety of flow rates

impedance tomography would be a suitable method for investigating the behaviour of oil and water flows non-intrusively.

5.5 Mathematics

The measurements made of voltage and current must be translated into values of the resistivity throughout the vessel being studied: this reconstruction process is at the heart of tomographic methods. It is desirable, if possible, to make this process computationally cheap so that data can be monitored in real-time.

The equation which describes the distribution of potential across a body with varying resistivity follows from charge conservation:

$$\nabla.(\rho^{-1}\nabla V) = 0 \tag{5–1}$$

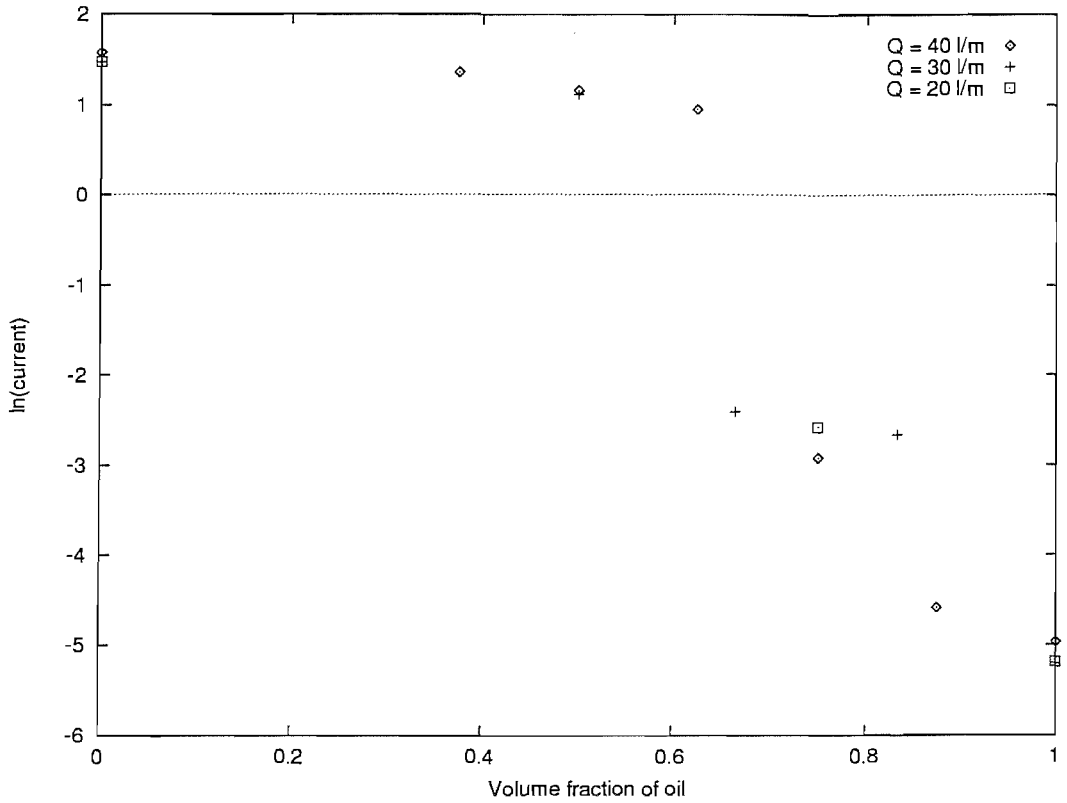

Figure 5.3: Current Injected vs. Volume Fraction of Oil, for Various Flow Rates

, where ρ is the resistivity of the medium. with the boundary condition

$$\rho^{-1}\frac{\partial V}{\partial \mathbf{n}} = J_0, \tag{5–2}$$

where J_0 is the normal component of current flux density on the surface of the body. To solve this for ρ makes the system a non-linear inverse boundary value problem, with mixed Neumann and Dirichlet boundary conditions, since potential rather than current is the measured quantity.

Many methods have been proposed for solving this problem: [23, 24] represent only a small sample. Many of these are designed for speed of use, and involve solving a linearized version of 5–1,5–2. In the case of the author's proposed research, speed is not perhaps so important as in clinical applications. Dickin et al. suggest that this method could be used to investigate inter-particle dynamics within a vessel: the less ambitious objective of determining time averaged concentration contours would not require the same speed of image processing, and the assumption of axisymmetry for these contours might also make this task easier.

5.6 Reconstruction of Tomographic Images

5.6.1 Achievable Performance

Dickin et al. quote some impressive results from their experiments: the 16 electrode configuration discussed above made it possible to detect changes of resistivity above 5%, and this is the region in which resolution in worst. They also have provide some reconstructed images of perspex and metal plugs in a saline solution in a 9cm diameter tank. Both are reproduced well, in the same image, despite very different resistivities.

5.6.2 Reconstructing Volume Fractions

Once resistivities within the vessel are known, then it is necessary, in the context of multi-component flow, to deduce from this the volume fractions of each component. Dickin et al. recommend the use of one or other of the effective medium theories (EMT) developed by Bruggeman [25], Meridith and Tobias [26], or others. These empirical relationships were tested by Dickin et al. in controlled experiments, and showed themselves to accurately represent the volume fractions. Some further tests of these simple empirical theories may be appropriate, since accurate results are particularly important in the phase inversion regime.

5.7 Results and Conclusions

A simple reconstruction algorithm was programmed, based on the material in [20], and used in an attempt to analyse the experimental data summarised above. However, the electrical measurements made during the course of this work were too few, and too noisy, to allow a detailed reconstruction of the local resistivities inside the test duct for each flow.

It has become clear that either the gain of the voltmeter, or the potential difference of the generator must be increased, in order for the results to be reconstructed for a wide range of mixtures.

However, it has at least been possible to demonstrate the potential of the technique: the electrical properties of the emulsion have been shown to depend on the concentra-

tions of the two phases, regardless of flow rate, and the voltage measurements made are consistent, to the limits of experimental accuracy, with a homogeneous emulsion of oil and water.

The use of EIT for monitoring hydrocyclones is now an established technology,[27], with sophisticated systems now available to monitor behaviour of hydrocyclone installations in an industrial context (focussing particularly on the air core). If nothing else, then the work describes here helps to demonstrate the possibility of applying such methods to liquid-liquid hydrocyclone flows.

Chapter 6

Computational Models — A Review

6.1 Introduction

This chapter begins with a brief outline of the widely used finite volume method for solving the equations of motion for fluid flow computationally. This methodology underpins most of the models discussed later in this chapter, as well as the commercial codes CFX and Fluent used by this author. Only a brief overview is given here; more details may be found in [28].

An overview of techniques used to model turbulence in computational fluid dynamics is then given, in order to provide a framework for the discussion of the individual turbulence models presented in the subsequent papers.

We then proceed to discuss and evaluate various computational models of the hydrocyclone in the literature. The majority of these are two-dimensional axisymmetric models, since this formulation drastically reduces the number of cells needed to create a model of the hydrocyclone, and thus reduces the memory and time require for its solution by computer. However, some more recent papers describe three dimensional models.

We shall see that turbulence modelling is of fundamental importance in hydrocyclone modelling. Each of the models discussed in this chapter uses a different turbulence model, most of which are devised by the authors specifically for the hydrocyclone. It is widely accepted that the k–ϵ model, while computationally cheap and widespread for solving engineering flows, is unsuitable for modelling the hydrocyclone but the papers reviewed here do not show a consensus on which model should replace it. This is partly because the

more elaborate and more flexible differential Reynolds' stress models were too demanding given the computational resources available at the time these papers where written. The importance of turbulence modelling is a theme taken up in later chapters where this author's work on the computational modelling of hydrocyclones is described.

6.2 An Overview of The Finite Volume Method

The finite volume method for solving the Navier-Stokes equations is widely used, and covered by a number of textbooks, in particular that of Patankar [28]. Most of the work described in Chapter 6 uses this method, as does the original research described in Chapter 8.

6.2.1 Fluid Flow Equations

We begin with the Navier-Stokes equations of incompressible fluid flow:

$$\begin{aligned} \frac{\partial \mathbf{v}}{\partial t} + (\mathbf{v}.\nabla)\mathbf{v} &= -\frac{1}{\rho}\nabla p + \nu\nabla^2\mathbf{v} \\ \nabla.v &= 0 \end{aligned}$$

The equation governing transport of a scalar, ϕ, by a fluid may be put in the generic form

$$\frac{\partial \phi}{\partial t} + (\mathbf{v}.\nabla)\phi = \nabla.(\Gamma_\phi \nabla\phi) + S_\phi, \qquad (6\text{–}1)$$

where S_ϕ is a source term for the variable ϕ. Equation 6–1 thus incorporates the effect of convection, diffusion and creation (or destruction) of the scalar quantity ϕ.

Additionally, each component of the Navier-Stokes momentum equations may also be written in this form, by incorporating into the source term S terms arising from the differentiation of the unit vectors, in non-Cartesian coordinate systems. As we shall see later, turbulence models usually require the modelling the transport of one or more scalar quantities, thus again making use of equation 6–1.

This allows the same computational framework to be used to solve all the equations, except that of continuity, relevant to the fluid flow.

6.2.2 Discretization of the equations

The finite volume method derives its name from the simple physical derivation of the discretized form of the equations it uses. The flow domain is divided into a number of quadrilateral boxes (in two dimensions), as shown in figure 6.1. This figure shows an arbitrary cell P in the domain of the flow, and the neighbouring cells N, S, E, W (for north, south, east and west), and the interfaces between cells, labelled n, s, e and w.

In order to discretise equation 6–1 for cell P only these nearest neighbours need be used, where we assume for simplicity that the grid is orthogonal. Equation 6–1 is integrated over the control volume P.

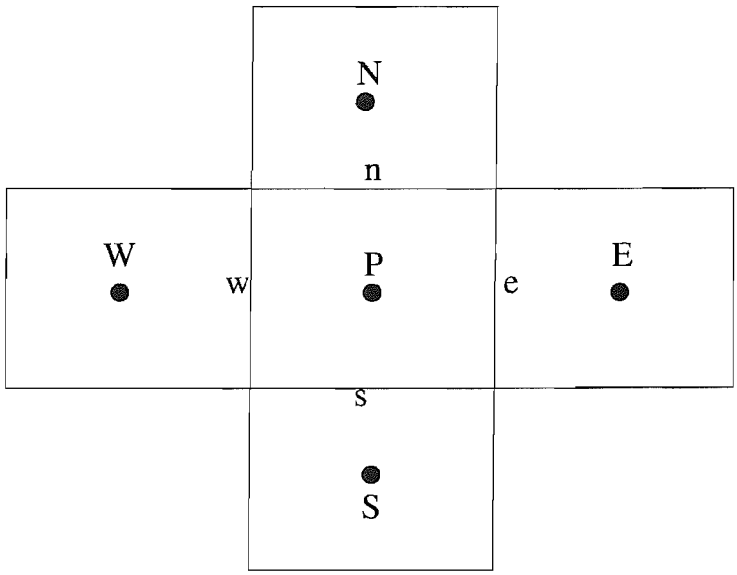

Figure 6.1: A cell in a finite volume grid

Clearly the flux of ϕ into the box by advection in the x direction is $\rho(u_e\phi_e - u_w\phi_w)$. Since the values of *phi* are only calculated at the centres of cells the values at the interfaces between cells must be found by interpolation.

The diffusive component of equation 6–1

$$\int_V \nabla.(\Gamma_\phi \nabla\phi)dV$$

is transformed by using the divergence theorem into a surface integral

$$\int_{\partial V} \Gamma_\phi \nabla\phi.\mathbf{dS}. \tag{6–2}$$

This can then be discretized using central differences.

6.2.3 The Pressure Equation

The Navier-Stokes equations do not contain a transport equation for pressure; this means an alternative procedure must be used to calculate this quantity. The method described here is the SIMPLE algorithm, discussed by Patankar [28]. This method and variations on it are the most widespread in commercial finite-volume CFD packages.

The method starts from a guessed initial pressure field, which is used in the solution of the velocity equations. Since the pressure field is incorrect, these velocities do not satisfy the continuity equation. It is therefore necessary to calculate corrections to the velocity and pressure fields. The continuity equation is then used to construct an equation for a pressure correction, which can be used to calculate a velocity field which does satisfy continuity. In practice the pressure correction equation is simplified to form a straightforward elliptical equation.

This process of calculating the velocity field, updating the pressure field, and correcting the velocities is carried out iteratively until the solution converges.

6.2.4 Solution of Linear Equations

A linear system of equations must then be solved at each iteration for each equation. Since this step is only part of the solution process, and the coefficients of the linearized equations are themselves not accurate it is not appropriate to solve the linear equations exactly, and one of a number of approximate methods is used.

Engineering Turbulence Models

Engineering models for turbulence are developed from the unsteady Navier-Stokes equations:

$$\frac{\partial v_i}{\partial t} + v_j \frac{\partial v_i}{\partial x_j} = -\frac{1}{\rho}\frac{\partial p}{\partial x_i} + \nu \frac{\partial^2 v_i}{\partial x_j \partial x_j}, \tag{6–3}$$

$$\frac{\partial v_i}{\partial x_i} = 0, \tag{6–4}$$

where v_i denotes the velocity in the i direction, p denotes pressure, and ρ and ν denote density and kinematic viscosity.

Instead of trying to solve these equations directly, however, the dependent variables of these equations v_i and p are subjected to the Reynolds' decomposition into mean and fluctuating components; $v_i = V_i + v_i'$, $p = P + p'$, where capital letters denote the time-averaged components of the variables, and primes are attached to the unsteady components, whose time averages are zero. Substituting these forms into equation 6–3, and taking the time-average of this system of equations yields

$$\frac{\partial V_i}{\partial t} + V_j \frac{\partial V_i}{\partial x_j} = -\frac{1}{\rho}\frac{\partial P}{\partial x} - \frac{\partial \overline{v_i' v_j'}}{\partial x_j} - \nu \frac{\partial^2 V_i}{\partial x_j \partial x_j}, \tag{6–5}$$

$$\frac{\partial V_i}{\partial x_i} = 0, \tag{6–6}$$

where an overbar represents the time averaging operator. This system resembles the steady Navier-Stokes equations, except for the inclusion of the divergence of the Reynolds' stress tensor $-\overline{v_i v_j}$.

In order to close this system of equations it is necessary to propose a model for the Reynolds' stresses in terms of the mean flow quantities. This is the point of departure for the models used in engineering CFD calculations.

The Reynolds' stresses form a second rank tensor, and the averaged Navier-Stokes equations also contain the second rank mean stress tensor. It is natural to attempt to link the two by some simple relationship. It is customary to consider separately the deviatoric stress tensor (which has zero trace) from the pressure gradient; this is then postulated to be proportional to the deviatoric Reynolds' stress tensor. Thus

$$-\left(\overline{v_i' v_j'} - \frac{2}{3}\delta_{ij} k\right) = \nu_T S_{ij} \tag{6–7}$$

where $S_{ij} = \frac{1}{2}\left(\frac{\partial v_i}{\partial x_j} + \frac{\partial v_j}{\partial x_i}\right)$ is the mean stress tensor, and $k = \frac{1}{2}\overline{u_i' u_i'}$ is the turbulent kinetic energy. The assumption that the two stress tensors may be linked in this way is known as the Boussinesq eddy viscosity hypothesis. It is also necessary to postulate a form for the turbulent viscosity, ν_T, in terms of the mean flow quantities.

This method for producing a model for the Reynolds' stress tensor is used by a family of models. These are known as isotropic turbulence models, since they impose no preferred direction on the flow other than that of the mean stress tensor. Such models are straightforward to implement; it is simply necessary to augment the laminar viscosity of the fluid by a 'turbulent viscosity' which varies throughout the flow field. Such models are distinguished by their method of determining such a viscosity.

This family of turbulence models includes the mixing length model, k–ϵ model, the k-ω model, the k-f models and others [29].

The k–ϵ model in particular is widely used in engineering CFD, as a result of its relative simplicity, and reasonable predictions in a wide variety of cases.

However, it is known [30],[3]that the k–ϵ fails in some cases, particularly that of confined swirling flows, where the effects of the anisotropy of turbulence are important. Faced with this difficulty researchers have shown an understandable reluctance to reject the k–ϵ model, and have attempted to modify it in such a way as to be suitable for these flows also.

Examples of this include [31],in which two separate (but proportional) turbulent viscosities were used in different directions, and [30], in which the requirement that the two viscosities be proportional was lifted. A disadvantage of such *ad hoc* modifications of the k–ϵ model is that one cannot be sure of their validity outside the range of situations for which they have been tuned. Another method used to enhance the k–ϵ method is to use a modified equation for ϵ; such models are described in [32] and [33].

However there are many situations (swirl burners, swirling jets) where the k–ϵ model, in one form or another, is widely used, and gives good agreement with experimental data. It is desirable therefore to characterise quantitatively the regimes for which isotropic turbulence models may be used, and those where they are inapplicable.

As the availability of powerful computer hardware becomes more widespread, it increasingly becomes feasible to use more sophisticated turbulence models for the flows that require them. The differential Reynolds' stress model [34] is now included as an option in many commercial CFD codes. This model requires that a transport equation be solved for each independent component of the Reynolds' stress tensor, incorporating production, redistribution, diffusion and dissipation terms. Various sub-models have been proposed for these terms, creating a family of differential Reynolds' stress models. In practice the models used in commercial CFD packages are fairly similar in structure [35]. These additional equations must be solved as well as an equation for ϵ; this means solving 7 partial differential equations for turbulence effects, in addition to 4 for the mean flow quantities. The computational burden imposed by this method of modelling turbulence is significant, particularly since the coupling between the mean flow equations and the

turbulent equations can no longer be achieved in terms of a turbulent viscosity.

In practice this leads to numerical instability of the resulting system of equations, and thus requires considerable relaxation of the numerical method. This in turn increases the computational effort involved in solving the equations.

The closure used for the k–ϵ model assumes that the Reynolds' stresses $\mathcal{R}$ are proportional to the mean stress tensor, so that turbulence may be modelled by increasing viscosity by the inclusion of the eddy viscosity, ν_T.

$$\nu_T = C_{v1}\frac{k^2}{\epsilon}, \tag{6–8}$$

where C_{v1} is an empirically determined constant, of which a typical value is 0.09 [36]. Both k and ϵ in this model are assumed to obey transport equations including convection, diffusion, production and dissipation terms. Such equations can be derived from the exact Navier-Stokes equations, but when this is done the equations include terms involving third order correlations of the fluctuating velocities. This means that, in order to close the model at this level, models for these terms in the k and ϵ equations must be constructed.

Markatos [36] gives a detailed review of these models and the modelling problems involved in closing the equations for k and ϵ.

6.2.5 Renormalized group theory k–ϵ Model

The renormalized k–ϵ model is a variant of the k–ϵ model which has been derived using the mathematics of renormalized group theory[32]. It has the advantage that the empirical constants associated with the k–ϵ model are derived theoretically. The model also uses a different form of the ϵ equation from the standard k–ϵ model. It has been claimed,[37], that this version of the model copes more successfully with the anisotropic turbulence associated with swirling flows.

In practice, the results obtained from this model by the author (using CFX) proved not to be significantly different from those obtained with the k–ϵ model. In particular it shares the defect of predicting a profile for swirl velocity more akin to that of solid body rotation than the Rankine combined vortex we expect in strongly swirling flows.

6.2.6 Algebraic stress model

The algebraic stress model is derived from the differential stress model, based on the observation that for some classes of flow the production and dissipation of turbulent components is likely to dominate their advective transport. This allows a considerable simplification of the solution of the equations for the Reynolds' stresses, and a corresponding reduction in the computational difficulty of solving these equations. However, in practice, using the implementation provided by CFX it turned out to be even more difficult to achieve convergence with this model than with the full differential stress model.

6.3 CFD models of Hydrocyclones

The complexity of the internal flow field in a hydrocyclone means that analytical models alone cannot reproduce all the details of the machine's behaviour. Many workers have thus opted to use computational models in the hope of being able to predict the relative motions of the light and heavy components of the feed mixture, and thus evaluate the performance of different hydrocyclone geometries. It is thought that the ability to do this would be a valuable aid to the design process, since CFD modelling is quicker and cheaper than prototyping a large number of different geometries. In order for this process to be viable it is necessary that a model for the effect on viscosity of the concentration of the dispersed phase can be devised.

A particularly controversial feature of the models discussed below is the appropriate turbulence model for this swirling flow: no two groups of workers use the same model, and preferences range from simple mixing length models to elaborate algebraic stress models.

6.4 Dependent variables

In creating a computational model for the flow in a hydrocyclone the choice must be made whether to solve the fluid flow equations in the primitive pressure-velocity form, or in the stream function-vorticity form. In view of the relative simplicity of the latter formulation it is surprising that only one group of workers (Hseih et al. [38, 39]) has

used it. Indeed Gupta [40] in his comprehensive book on swirling flows asserts that '... it is generally convenient to retain pressure and velocity as dependent variables, rather than introduce the stream function and vorticity.' One possible explanation for this preference among workers on hydrocyclones is that most of the models in the literature are designed to predict the behaviour of particle separating hydrocyclones, which are open to the atmosphere, and hence have an air core. Having dispensed with the pressure as a variable in their numerical model Hseigh et al. are forced to determine the air core as the smallest radius for which their numerical method converges. However, in the context of the de-watering hydrocyclone this would not cause difficulties, as the hydrocyclone is not open to the atmosphere. Another reason why pressure-velocity formulations are preferred is because the primitive variables correspond to quantities that engineers both measure and use when reasoning about flows.

All other workers (Dyakowski and Williams [41]; Boyson et al. [42]; Hargreaves and Silvester [3]; and Pericleous et al. [43]) use pressure and velocity as their dependent variables.

6.5 Boundary Conditions

There is a widespread agreement about the boundary conditions to be used in a hydrocyclone model. Indeed, so standard are the boundary conditions for such flows that descriptions in some of the papers reviewed are rather terse.

6.5.1 Axis of symmetry

The assumption of axisymmetry means that the boundary conditions there are easy to establish: Here, by virtue of symmetry, the radial and tangential components of velocity are zero. The same assumption implies that derivatives of all other quantities with respect to radial distance[1] vanishes at the axis.

[1]Note that cylindrical polar (r, θ, z) coordinates are invariably used in these models.

6.5.2 Inlet

The purpose of assuming the flow to be axisymmetric is to reduce the problem from three dimensions to two dimensions. However, the inlet is not symmetric about the axis, and the flow is also expected to deviate from axisymmetry in the upper conical region of the hydrocyclone. To take full account of this would require a three dimensional model, and it is felt preferable by all workers to model the inlet as a toroidal region, thus giving it the same symmetry as the rest of the hydrocyclone.

6.5.3 Exit Planes of Vortex Finder and Underflow Orifice

In order to preserve the rotational character of the flow Pericleous et al. extend the solution domain here and use a boundary condition derived from decaying swirl flow in a pipe, namely

$$\frac{dp_{ext}}{dr} = \rho \frac{v_{\theta_{ext}}^2}{r}, \tag{6–9}$$

where $v_{\theta_{ext}}$ is a fixed proportion of the velocity in the adjacent 'cell' of the discretised geometry.

In these areas Hargreaves and Silvester [3] have the most surprising choice of boundary condition: they assume plug flow in the axial direction across both these planes, so that the swirl velocity (tangential velocity component) is zero on each of these planes. The model subsequently predicts flows unlike those found experimentally, especially in these regions, and the authors conclude that this boundary condition is unsatisfactory.

Boysan et al. [42] assume, less controversially, that the axial derivatives of all quantities across these planes are zero.

6.5.4 Near Cyclone Walls

Again, considerable agreement between authors is found on this subject, with the unanimous choice being a logarithmic wall function.

6.5.5 Conclusions

The boundary conditions used in this authors' work as described in chapters 8 and 7 are as follows:

Inlet

For axisymmetric models the inlet height, h_{inlet} should be that of the inlet in the physical model. For a volume flux Q and a (physical) inlet cross-sectional area of A_{inlet} through a hydrocylone, the velocity given by $v_\theta = \frac{Q}{A_{inlet}}$ is used as the inlet condition for tangential velocity.

The radial velocity at the inlet is set to make the volume flux through the axisymmetric model the same as that of the physical model, i.e., we set $v_r = \frac{Q}{\pi D}$.

The axial velocity at the inlet is assumed to be zero.

6.6 Turbulence Models

As stated in the introduction to this section this is by far the most controversial feature of the models, although all workers in the field use models which link the Reynolds' stresses to mean flow quantities. The alternatives, such as large eddy simulation, are not yet sufficiently developed to be useful in such a complex flow. A useful review of some of the relevant literature is given by Duggins and Frith [30]. In particular they cite experimental work by Lilley and Chigier which shows that turbulent viscosities are anisotropic in strongly swirling flows, such as those in a hydrocyclone, and that the turbulent viscosity components $\mu_{r\theta}$ and μ_{rz} are the most important, and further that these have quite different distributions radially across the flow. Further reviews are included in the paper by Hargreaves and Silvester [3], and the book by Gupta et al. [40].

6.6.1 Pericleous et al.

These authors use the mixing length hypothesis, the simplest possible turbulence model. This model has the advantage of being governed by only one empirically specified con-

stant. The model used is:

$$\mu_t = \rho\lambda^2 \left| \frac{\mu_0}{\rho\lambda^2} + \frac{\partial v_\theta}{\partial r} - \frac{v_\theta}{r} \right|, \tag{6–10}$$

where ρ is density, and λ is the mixing length. The form of this equation is the same as that used by Bloor and Ingham [6], and the extra term is introduced here, as there, to ensure that turbulence does not vanish in the forced vortex, where shear is zero. The authors assume the mixing length to be a constant given by $\lambda = D_0/30$ where D_0 is the diameter of the cylindrical part of the hydrocyclone.

6.6.2 Hseih and Rajamani

These authors use a modified mixing length model, given by

$$\mu_t = \rho\lambda^2 \left(\left| \frac{\partial v_\theta}{\partial r} - \frac{v_\theta}{r} \right| + \left| \frac{\partial v_z}{\partial r} \right| \right). \tag{6–11}$$

The mixing length, λ is assumed to depend on r and the (laminar) viscosity of the fluid locally, which varies with dispersed phase concentrations. The form of the mixing length is the same for all the components, however, the empirically determined coefficients are taken to be different in different components of the momentum balance equation (which is converted into equations for angular momentum, the azimuthal component of vorticity, and the stream function in this paper). The form of the mixing length is designed to fit experimental data, rather than for any physical reasons, and is accordingly not reproduced here. This model is perhaps the simplest possible which still takes into account the anisotropy of the flow.

6.6.3 Duggins and Frith

This paper [30] begins with a review of previous work on strongly swirling flows. The authors share the conviction of Pericleous et al. that the widely used k–ϵ model is, in its standard form, inappropriate to this context, since it assumes the flow to be isotropic. However Duggins and Frith [30] argue that to revert to the mixing length hypothesis is a step backwards, and they present in this paper a modified k–ϵ model. As mentioned in the introduction to this section they assert, with reference to experimental data, that the dominant components of turbulent viscosity are $\mu_{r\theta}$ and μ_{rz}. Again referring to

the experimental data they assert that the k–ϵ model captures the shape of the μ_{rz} component well enough, but not that of the $\mu_{r\theta}$ component. Accordingly they introduce for this component of turbulent viscosity a model due to Rochino and Laven [44]:

$$\mu_{r\theta} = \rho C_w^2 r^2 \left| \frac{\partial v_\theta}{\partial r} - \frac{v_\theta}{r} \right|, \tag{6–12}$$

where C_w is an empirically determined constant ($C_w = 0.028$).

It is curious that having attempted to build a turbulence model on foundations provided by experimental data, the authors do not present any verification of their model.

6.6.4 Hargreaves and Silvester

The turbulence model presented in this paper [3] is more sophisticated those described above. The authors accept that the standard k–ϵ model is inappropriate, but consider that a full Reynolds'-stress transport model would be prohibitively expensive computationally. By way of compromise they suggest a system of equations which incorporates two transport equations for Reynolds'-stress components: namely $\overline{v_z' v_z'}$ and $\overline{v_\theta' v_\theta'} - \overline{v_r' v_r'}$, where primes denote fluctuating quantities, and subscripts indicate the direction of velocity components. Other Reynolds'-stress components are deduced from algebraic stress relations, or from the definition of turbulent kinetic energy, k. The result of all this sophistication is unclear, since the boundary conditions were modelled in an unsatisfactory way. These were then altered, but results continue to show discrepancies from those measured using laser Doppler anemometry techniques.

6.6.5 Boysan et al.

These authors propose a yet more complicated turbulence model. The model used is an algebraic stress closure model (ASM), in which the full transport equations for the Reynolds'-stresses are modified. These equations can be written schematically as

$$T_{ij} = P_{ij} - \frac{2}{3}\epsilon\delta_{ij} + \psi_{ij}, \tag{6–13}$$

where T_{ij} represents the combined convection and diffusion terms, P_{ij} represents the production of Reynolds'-stresses, ϵ is the dissipation of turbulent kinetic energy, and ψ_{ij} represents the redistribution of Reynolds'-stresses, due to interaction with the pressure

field. It is this last term which provokes the use of models this complex: in standard k–ϵ models this term is neglected since the turbulence is assumed to be isotropic. This equation can be derived from the Navier-Stokes equations, but it is necessary to introduce a model for the pressure strain term. As well as using such a model, Boysan et al. introduce an algebraic model for the convection of the Reynolds'-stresses, on the grounds that convection and diffusion of these quantities is not crucial to the success of equation 6–13 in this context. Equation 6–13 must still be combined with the customary k–ϵ transport equations to complete the system.

The model does show good agreement with experimental results obtained by Linden. Incidentally the cyclone modelled in this paper was a gas cyclone, of about 8 inches diameter, and thus not so strongly swirling as the hydrocyclones investigated elsewhere. However, the model has been criticized by Duggins and Frith [30] for its complexity, and by Hargreaves and Silvester [3] for using a fixed algebraic pressure strain model.

6.6.6 Dyakowski and Williams

Dyakowski and Williams [41] set out specifically to model small diameter hydrocyclones, with correspondingly stronger swirl. They consider the above described model of Boysan et al. to be inappropriate in this context, and describe it as a shortcoming of previous models that they take no account of the effect of rotational flow on the normal components of the Reynolds' stresses. In order to take this into account, for the highly curved streamlines which they consider, Dyakowski and Williams propose a yet more elaborate turbulence model: the Reynolds' stresses being calculated from the formula

$$\tau_{ij}^{t} = \frac{2}{3}k\delta_{ij} - 2C_{\tau_1}\frac{k^2}{\epsilon}S_{ij} - C_{\tau_1}\frac{k^3}{\epsilon^2}\left(\epsilon_{ijk}S_{jk} + \epsilon_{jkm}S_{ik}\right)\Omega_m, \qquad (6\text{–}14)$$

where Ω_m is the m^{th} component of the mean vorticity vector ($\Omega = curl(V)$), S_{ij} is the mean rate of strain tensor, and ϵ_{ijk} is the alternating tensor. This formulation is discussed by W.C.Reynolds in Bradshaw [29], who comments that it gives the right form of normal stress anisotropy, but does not alter shear stresses which have to be modelled separately. The shear components of the Reynolds' stresses are calculated from the k–ϵ transport equations, except for $\mu_{r\theta}$. For this component a variation on the formula 6–12 due to

Rochino and Laven[44] is used, namely:

$$\mu_{r\theta} = \rho l_{r\theta}^2 \left[\left(\frac{\partial v_z}{\partial r} \right)^2 + \left(r \frac{\partial}{\partial r} \left(\frac{v_\theta}{r} \right) \right)^2 \right]^{1/2}, \tag{6-15}$$

where the length scale $l_{r\theta}$ is taken to be a constant. The agreement achieved between the model and experimental results is good, although the comparisons are not extensive. This study is perhaps the most pertinent to the author's project, since the model is designed for small diameter hydrocyclones, with correspondingly strongly swirling flows.

6.6.7 Conclusions

With the continuing advances in computer hardware more sophisticated turbulence models are now affordable than was the case when most of the work described above was performed. The differential Reynolds' stress model is now a feasible option, and its ability to capture the behaviour of a strongly swirling anisotropic flow-field makes it a natural choice for CFD models of hydrocyclones. Chapter 7 provides evidence that isotropic turbulence models (such as the k–ϵ model) are inadequate for such flows. Specially developed turbulence models for hydrocyclones, as used in several of the papers reviewed above, are no longer necessary and the need to make simplifying assumptions about the form of the Reynolds' stress tensor and to fit various parameters empirically reduce the generality of such models. Accordingly, the original research described in this thesis uses the differential Reynolds' stress model, as implemented in CFX.

6.7 Modelling the Dispersed Phase

There are two distinct methods for modelling the behaviour of the dispersed phase in the hydrocyclone: stochastic particle tracking, as in [42, 3] and mean flow phase coupling, as in [43, 38]. Both make use of the Lagrangian equations of motion for a particle.

The latter approach uses equations similar to those presented by Bloor and Ingham in this context (as described in Section 3.7) to determine the relative motion of the particles with respect to the fluid. The equations of motion for the fluid are then solved iteratively: first the continuous phase equations of motion are solved, particle motion relative to the continuous phase is used to calculate local particle concentrations, and these in turn are

used to calculate effective local densities and viscosities of the composite fluid, and the process is repeated until it converges. Pericleous et al. [43] obtain good results for the predicted grade efficiency curve using this method.

The stochastic particle tracking method relies on the assumption that the particles' motions are independent, and is thus only applicable to dilute dispersions. The differential equations for particle motion are solved relative to the computed flow of the continuous phase, with the effects of turbulence being incorporated by assuming that the fluctuations in velocity components have a Gaussian distribution. This model requires a considerable computational effort to predict a grade efficiency curve, and the models presented in [42] and [3] both overestimate the separation efficiency of the hydrocyclone for large particles. This approach is, in any case, unsuitable for the large volume fractions of the dispersed component to be investigated by this author; potentially the separation of oil and water could lead to regions in which either is almost pure.

6.8 Three dimensional models

With the increase in available computing power, some researchers [45], [46], have begun to develop three dimensional models of the hydrocyclone. The main advantage of such models is the accuracy with which they can handle the non-axisymmetric flow near the inlet.

Slack and Wraith [46] modelled a hydrocyclone whose flow field had been investigated experimentally, using the commercial code Fluent. They used three turbulence models: the k–ϵ model, the renormalized group theory version of the k–ϵ model, and the differential Reynolds' stress model built into Fluent. They found that only the latter predicted the Rankine vortex profile for azimuthal velocity. Using this model their computed results were a good fit for the experimental results of Knowles.

Ma *et al.* [45] developed a three dimensional model of an air cyclone using both the standard and RNG k–ϵ models. They do not report their computed azimuthal flow field. However, the cyclone correction curves (calculated using the Lagrangian equations of motion for each particle) are not a good fit to the experimental data.

6.8.1 Conclusions

With the computer hardware available to the author full three-dimensional models of a hydrocyclone were not feasible. Chapter 7 describes a simple three-dimensional model intended to guide the axisymmetric modelling of cyclone inlets.

In the future, three dimensional models will allow consideration of aspects of hydrocyclone geometry which cannot be captured accurately in axisymmetric models, such as specific details of inlet and outlet design. However, it is likely that in view of their relative computational economy axisymmetric models will remain useful design tools for hydrocyclones for some time to come.

6.9 Discussion: The De-Watering Hydrocyclone

The author's field of study is the de-watering hydrocyclone, in which a dispersion of (relatively) dense water is to be separated from a continuous oil phase. Previous experimental work on this problem has led to a commercially viable product, but there is room for improvement in the design to enhance separation efficiency. There are considerable difficulties associated with operating a hydrocyclone separator in this regime:

- Oil is more viscous than water, so that:
    1. Drag on water droplets is high so that droplet migration to the cyclone wall is slow.
    2. Water droplets can be sheared apart, either by high mean stresses or by turbulent eddies, into smaller droplets, and separation efficiency decreases with decreasing droplet size.
- The density difference between the components is small, requiring large centrifugal force-fields to exploit it, and this leads to high shear, and the problem mentioned above.
- At a critical range of volume fractions phase inversion occurs: water becomes the continuous phase containing dispersed oil droplets. In the transition range of volume fractions the effective viscosity of the composite fluid becomes much higher than

the viscosity of either phase in isolation. This phenomenon hinders the settling out of water droplets and hence reduces separation efficiency.

As was mentioned above, the choice of model used for turbulence is the major difference between these authors whose work is reviewed in this chapter. It may be useful to present a summary of the models used and their advantages and disadvantages.

- Mixing length model
  - This model is the simplest in widespread use, and is computationally very economical.
  - The mixing length (which characterises eddy size and gives rise to an eddy viscosity) is calculated using empirical relationships involving 'constants' (which may vary within a hydrocyclone and between geometries).
  - The model thus depends on experimental validation whenever significant modifications are made to the geometry or flow regime.
- k–ϵ model
  - This model is moderate in its computational demands – two additional differential equations must be solved to determine an eddy viscosity (which varies spatially).
  - It has become the standard model in engineering CFD, and specifically turbomachinery.
  - It assumes turbulence is isotropic, which is not the case in hydrocyclones.
- modified k–ϵ (including RNG k–ϵ model)
  - Such models vary in their computational demands, but most are comparable to the k–ϵ model.
  - They can allow for anisotropy, on an *ad hoc* basis.
  - These models are brittle – being 'tuned' for one regime, they can not be relied upon when conditions are changed.

- Algebraic stress
  - These models require the additional computational effort (relative to the k–ϵ model) of requiring algebraic relations to be solved for each component of the Reynolds' stress tensor.
  - They can account for some degree of turbulence anisotropy.
  - They can have convergence problems, and neglect important terms to form algebraic relations from differential equations
- Differential stress model
  - This is the most computationally demanding model in engineering use, requiring the solution of differential equations for each component of the Reynolds' stress tensor.
  - It can account well for anisotropy.
  - It is not well established in industrial practice, as a result of its computational demands.

It seems reasonable, therefore, to anticipate that a combination of experimental, theoretical and computational modelling will be required in order to assess the effects of relatively simple design (i.e., geometry) changes on the separation efficiency of the hydrocyclone.

Chapter 7

Turbulence anisotropy and CFD modelling of hydrocyclones

7.1 Introduction

[1]

The flow field inside a hydrocyclone is complex; even with a single component of flow the anisotropic turbulence within the device makes accurate computational results difficult to obtain. However, a computational model of a de-watering hydrocyclone would be a valuable alternative to extensive experimental studies. The increasing maturity of the science of CFD, and the rapidly increasing capabilities of widely available computing hardware makes developing such a model an increasingly attractive possibility.

In this chapter a measure for turbulence isotropy is proposed, and used to show the increasing inadequacy of scalar eddy viscosity models with increasing swirl. The assumption of axisymmetry is examined. This assumption is always made in computational models of the hydrocyclone, on the grounds of computational economy. However, while this is a reasonable approach, it is necessary to consider carefully the boundary conditions for the model; in particular for the turbulent quantities.

[1]This work was originally published in the proceedings of the Hydrocyclones '96 Conference[47]. It is reproduced here, largely intact, as quantitative evidence of the problems caused by an injudicious choice of turbulence model.

7.2 Measuring Turbulence Isotropy

7.2.1 Isotropy

In the laminar Navier-Stokes equations the kinematic viscosity, ν, acts as an isotropic coefficient of diffusion. The class of turbulence models resulting from consideration of the time-averaged Navier-Stokes equations can be considered as defining more complex forms for the diffusion coefficient of momentum. The diffusion term arising in the averaged momentum equations (6–5) can then be written as

$$\frac{\partial}{\partial x_j}\left(\nu_{ik}\left(\frac{\partial U_k}{\partial x_j}+\frac{\partial U_j}{\partial x_k}\right)\right) \tag{7–1}$$

Isotropy of turbulence is thus defined in terms of the isotropy of the second rank tensor ν. The most general form of a second rank isotropic tensor is

$$\nu_{ik} = Ar_i r_k + B(\mathbf{r}\delta_{ik}), \tag{7–2}$$

where $\mathbf{r}$ is the position vector. It is clear that the term proportional to $r_i r_k$ is unphysical in a model for turbulent viscosity, and the remaining term is equivalent to prescribing an eddy viscosity. Thus a turbulent flow is isotropic precisely in so far it can be predicted with an eddy viscosity model. Although the failure of such models in strongly swirling flows has been reported ([3], [30]) it is here sought to quantify the departure of the turbulence from isotropy, and to show the correlation between this behaviour and increasing swirl.

7.2.2 The Theory

In order to quantify the anisotropy of a turbulent flow field we must have some way of accurately predicting it. Measurements of second order velocity correlations which present sufficient detail for this purpose are not available for the strongly swirling flows investigated here. Accordingly CFD calculations using the differential Reynolds' stress model have been used as a reference. This model, although not perfect, is widely accepted to be the most elaborate (and accurate) turbulence model typically available for engineering flows. In particular it is the most complicated model built into the CFD package CFX, used in the work described here.

Denote the deviatoric mean stress tensor by $\mathbf{S}_{d_{ij}}$, and the deviatoric Reynolds' stress tensor by $\mathbf{\Sigma}_{d_{ij}}$. Then the hypothesis that we seek to test is that it is possible to write

$$\mathbf{\Sigma_{d}}_{ij} = \nu_T \mathbf{S_{d}}_{ij}. \tag{7–3}$$

with some relationship for ν_T. Equation 7–3 may be taken as a definition of isotropic turbulence; the turbulent effects have no preferred direction.

The above equation may be written

$$\mathbf{I} \propto \mathbf{\Sigma_{d}}_{ij}^{-1} \mathbf{S_{d}}_{ij}, \tag{7–4}$$

where I is the identity matrix, it is possible to develop a measure of the deviation of the right hand side of this equation from a multiple of the identity tensor. However, such a method is unsatisfactory. Both stress tensors enter into the averaged momentum equations only in terms of their divergence, so that the equation which must hold for isotropy is

$$\nabla . \mathbf{\Sigma_{d}}_{ij} = \mathbf{S_{d}}_{ij} . \nabla \nu_T + \nu_T \nabla \mathbf{S_{d}}_{ij}. \tag{7–5}$$

There are 6 constants of integration involved in the transition from the differential form (7–5) to the integrated form (7–3). Although some constraints may be imposed between these constants as a result of the form of the eddy viscosity hypothesis, we may not expect the integrated form to hold exactly when using the differential Reynolds' stress model.

The equation (7–5) must be manipulated before it can be used in a CFD calculation. First the equation is integrated over a control volume V to give

$$\int_V \nabla . \mathbf{\Sigma_{d}}_{ij} \, dV = \int_V \mathbf{S_{d}}_{ij} . \nabla \nu_T \, dV + \nu_T \int_V \nabla . \mathbf{S_{d}}_{ij} \, dV. \tag{7–6}$$

The divergence theorem may then be used to transform two of the volume integrals to surface integrals:

$$\int_S \mathbf{\Sigma_{d}}_{ij} . \, \mathbf{dA} = \int_V \mathbf{S_{d}}_{ij} . \nabla \nu_T \, dV + \nu_T \int_S \mathbf{S_d} . \, \mathbf{dA}, \tag{7–7}$$

where $\mathbf{dA}$ is taken to be an outward normal to the cell.

The equation discretizes in a straightforward manner.

$$\sum_i \Sigma_{\mathbf{d}ij}.\mathbf{A}_i = V\mathbf{S}_{\mathbf{d}ij}.\nabla\nu_T + \nu_T \sum_i \mathbf{S}_{\mathbf{d}ij}.\mathbf{A}_i, \tag{7–8}$$

where i ranges over the faces of the cell. Or,

$$\sum_i \Sigma_{\mathbf{d}}.\mathbf{A}_i - V\mathbf{S}_{\mathbf{d}}.\nabla\nu_T \propto \sum_i \mathbf{S}_{\mathbf{d}}.\mathbf{A}_i, \tag{7–9}$$

The stresses at cell faces are evaluated by means of linear interpolation from neighbouring cell centres.

Equation (7–9) allows a straightforward parameterization of isotropy; denoting by $\mathbf{a}$ and $\mathbf{b}$ the left and right hand expressions of (7–9) we define an isotropy parameter, η, by

$$\eta = \frac{\mathbf{a}.\mathbf{b}}{|\mathbf{a}||\mathbf{b}|}. \tag{7–10}$$

7.3 The Simulations

A series of simulations of the flow in a conventional hydrocyclone was performed, based on a geometry (hydrocyclone number 1) described in [39]. This hydrocyclone has diameter 75mm, and a total cone angle of 20°. One deviation from the circumstances assumed in [39] was that the cyclone was assumed to be operating without an air core. This was partly a result of a desire not to complicate the model unduly, and also a reflection of the status of this work as a preliminary to the authors' work on liquid-liquid hydrocyclones operating without gas-cores. It is not felt that this departure will have too deleterious an effect on the model's worth as an indicator of the usefulness of the various turbulence models considered, since the air core in an operating flow is typically within the solid-body core of the flow, and matches onto it without disrupting the liquid flow.

A series of simulations was performed using this geometry with varying swirl, using the commercial CFD code CFX. The degree of swirl was characterised in the first instance by the inlet swirl angle, a parameter which requires some explanation. In the axisymmetric simulation a section of the side wall of the hydrocyclone is designated as an inlet. In CFX it is necessary for the flow at an inlet to have a component of velocity perpendicular to the inlet, in order for the flow to enter the solution domain. The radial velocity was thus fixed for all the simulations in order to give a flow-rate of 67 kg/min (1.12 m^3/s),

as used in [39]. The azimuthal inlet velocity may then be adjusted arbitrarily, without affecting the volume flux through the device. The inlet angle, α is then defined to be $\arctan(v_\theta/v_r)$.

Although this parameter may be used to characterize the intensity of the swirl before the simulation is carried out, afterwards the swirl number, which seeks to measure the ratio of the axial flux of axial momentum to the axial flux of azimuthal momentum,

$$S = \frac{\int_0^{R_{wall}} V_\theta |V_z| r^2 \, dr}{R_{wall} \int_0^{R_{wall}} V_z^2 r \, dr}, \tag{7–11}$$

may be calculated. This is one popular definition of swirl number [48], several other definitions exist of similar parameters. An additional post-processing step was the calculation of the split ratio, F, where F is the ratio of volumetric flux through the overflow to the total volumetric flux through the device.

The calculations were performed using a grid with 15 subdivisions radially, and 40 axially on the cyclone body. Extended outlets were used in order to mitigate the effects of the downstream boundary conditions, which were of zero gradient type. The solution method used was the finite volume method, as described in [28], using the hybrid differencing scheme. Attempts to use higher order schemes resulted in numerical instabilities.

Each of the simulations took of the order of 3 hours of CPU time on a Sun Centre 1000 computer. This is largely a result of the need for considerable numerical under-relaxation during the solution of the discretized equations; attempts to accelerate convergence usually lead instead to divergence of the numerical method. Given the high computational cost of the solution method, it is understandably desirable to use more economical turbulence models where possible.

7.4 Results

Table (7.1) tabulates the split ratios, pressure drops and swirl numbers for each of the simulations. We see that, as would be expected, the split ratio F, the pressure drop

Swirl Angle α (°)	Pressure Drop ΔP_{io} (Pa)	Split Ratio F	Swirl Number S
10	4.19×10^3	0.776	0.024
20	4.33×10^3	0.776	0.048
30	4.78×10^3	0.783	0.079
50	6.27×10^3	0.792	0.149
70	1.16×10^4	0.842	0.160
80	1.97×10^4	0.896	0.391

Table 7.1: Summary of Computational Results

ΔP_{io} across the hydrocyclone and the swirl number, S, all increase with the degree of swirl at the inlet.

Figures 7.1, 7.2, 7.3, 7.4, 7.5 show contour plots of η throughout the body of the hydrocyclone at different flow inlet angles. Note that although these contour plots all use the same range of colours, the numerical values of η vary from plot to plot.

For the 20° shown in Figure 7.1 inlet the flow throughout much of the hydrocyclone is isotropic, with values of η greater than 0.7. The exception is an annular region near the inlet. Figure 7.2 shows that for the 30° case the region inside the vortex finder remains isotropic, with $\eta > 0.7$. Throughout much of the conical part of the hydrocyclone η remains 0.4 or above, but it is remarkable that for this case, with a swirl number of less than 0.05 the assumption of isotropic turbulence begins to be quite inaccurate.

The 50° and 70° cases shown in Figures 7.3 and 7.4 continue the trend of increasing anisotropy in the cyclone body, with values of η dropping to 0.3 for much of the conical part of the hydrcocyclone. With the 70° and 80° cases shown in Figures 7.4 and 7.5 we may see that even the region inside the vortex finder has become anisotropic.

An interesting development throughout his series of flows is the way in which the region of negative η develops. At low inlet angles there is an annular region of negative η just inside the inlet, but as the angle increases this shrinks until at 80° it has almost entirely vanished. This arises because at low inlet angles the flow at the inlet is primarily

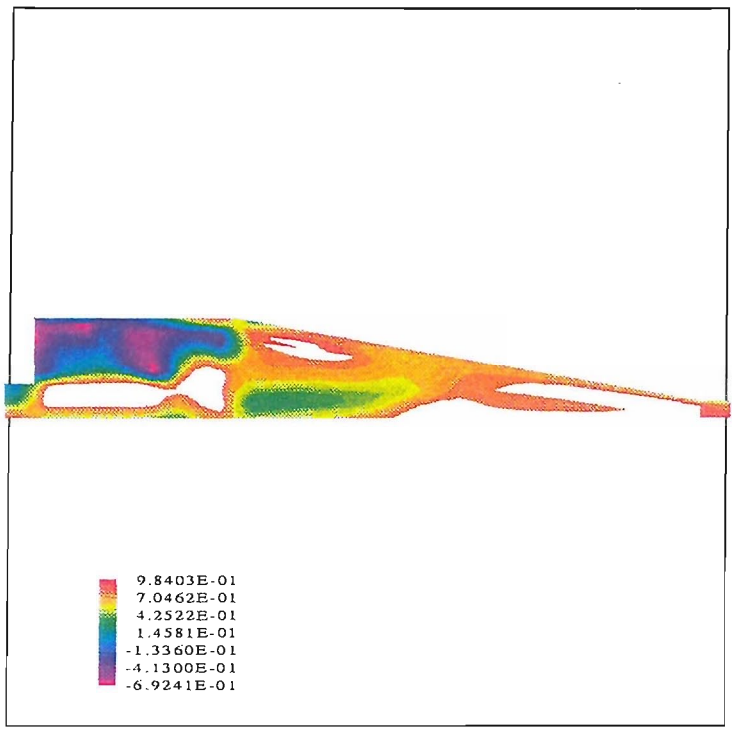

Figure 7.1: Isotropy for 20° inlet angle

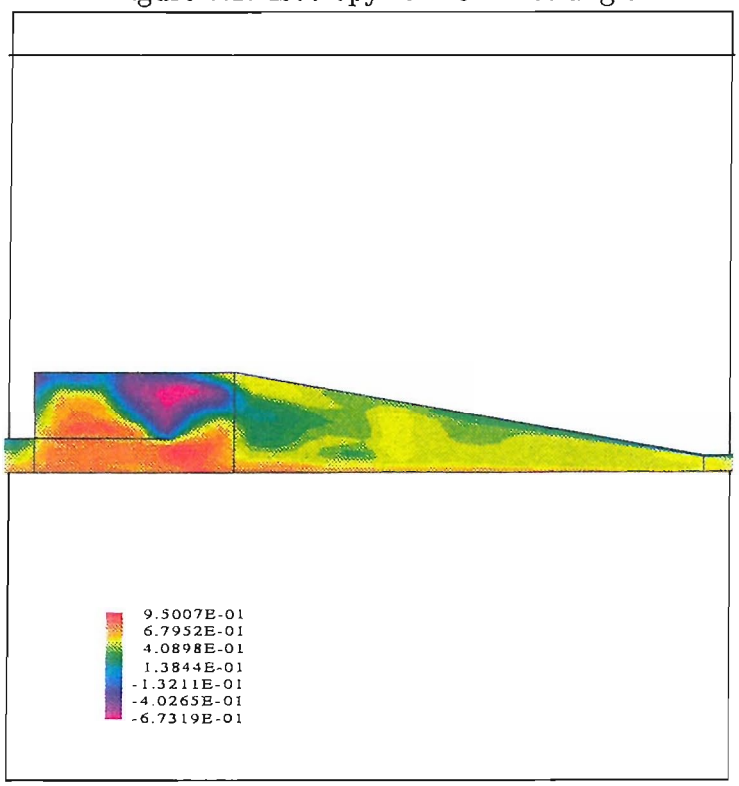

Figure 7.2: Isotropy for 30° inlet angle

radially inwards towards the vortex finder and creates a highly turbulent mixing region as it converges. As the inlet angle increases the increasing dominance of swirl on the flow

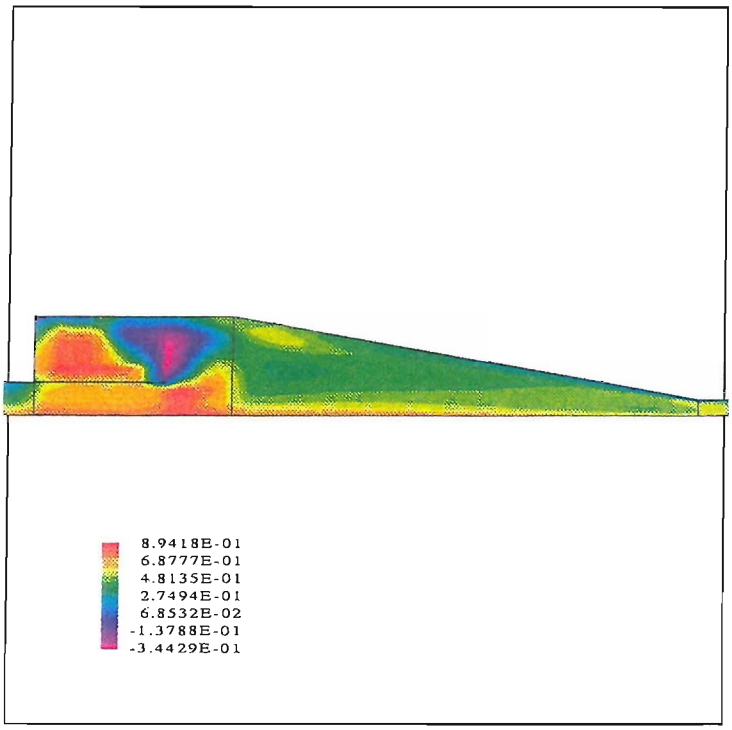

Figure 7.3: Isotropy for 50° inlet angle

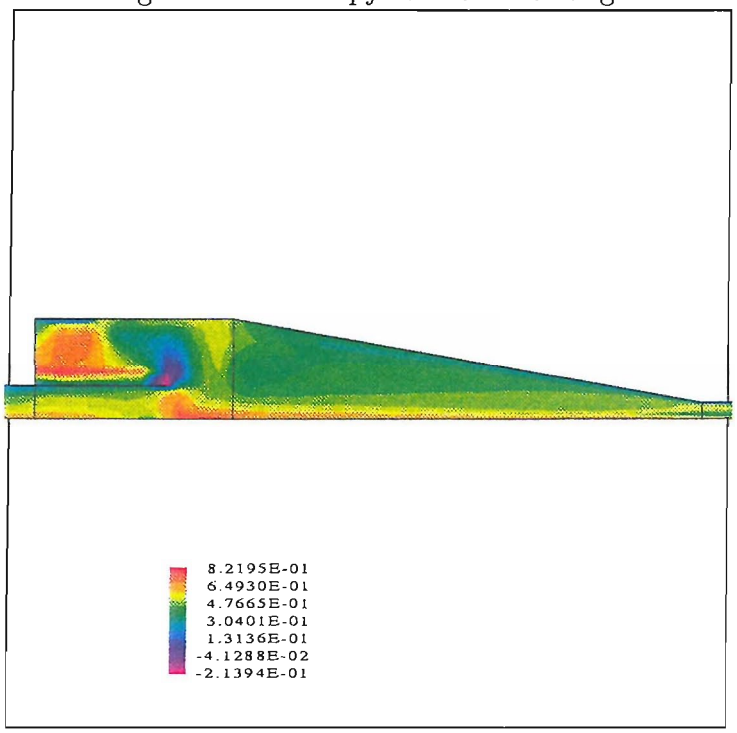

Figure 7.4: Isotropy for 70° inlet angle

field causes it to take on the pattern of a hydrocyclone with flow entering at the inlet and moving down the outside wall before reversing to exit via the overflow exit.

In conclusion we note that the assumption of isotropic turbulence is only reasonable

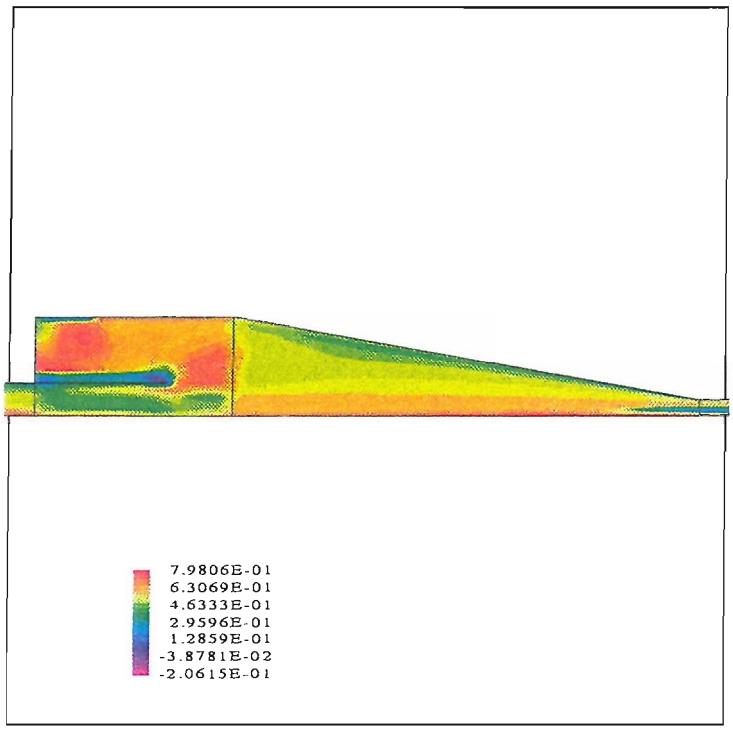

Figure 7.5: Isotropy for 80° inlet angle

at an inlet angle of 20°; even the 30° case shows a significant departure from isotropy. It follows that the k–ϵ model, or any similar two equation model of turbulence, cannot be used to predict any cyclonic flow of even moderate swirl.

7.5 Three Dimensional Modelling

7.5.1 Introduction

Most computational models of hydrocyclones make the assumption that the flow field is axisymmetric, and solve for the flow only on a cross-section of the device. While there is no reason to suppose this procedure is invalid, it requires careful attention to the boundary conditions specified at the inlet. In practice, the single or twin tangential inlets of a hydrocyclone mean that the flow comes into the cyclone chamber by way of a sudden expansion.

In an axisymmetric model of a hydrocyclone, where the inlet is modeled as a ring on the wall of the device, the effects of the expansion are not modelled. If the boundary conditions imposed for the turbulent quantities k and ϵ those appropriate to fully

developed pipe flow, as given below in equations 7–12, then there exists the possibility that these quantities are seriously underestimated; the boundary conditions for an axisymmetric model must represent the values of any turbulent quantities just within the cyclone chamber.

This is particularly important in the case of liquid-liquid hydrocyclones, since the effects of turbulent shear at the inlet may have an important effect on droplet break-up in the region near the inlet. This in turn has an important effect on separation performance.

7.5.2 The Simulation

The computational expense of a fully three dimensional model of a hydrocyclone is prohibitive. However, it is possible to use a much simplified three-dimensional model of the inlet region as a guide to setting realistic conditions for an axisymmetric model. Accordingly a model was developed in which the cyclone chamber was represented by a cylinder (75mm in diameter), with two tangential inlets of cylindrical cross-section (25mm in diameter). This was modeled using CFX. The turbulent boundary conditions inside the inlet pipes were taken to be those deduced from fully developed pipe flow [49]:

$$k_{inl} = C_{p_1}|V_{inl}|^2 \tag{7–12}$$

$$\epsilon_{inl} = \frac{k_{inl}}{C_{p_2}}D \tag{7–13}$$

where $C_{p_1} = 0.002$ and $C_{p_2} = 0.3$ are empirical constants, and D is the inlet diameter. The turbulence model used was the differential Reynolds' stress model.

The geometry was modeled using 96 subdivisions axially, and a 16 by 16 body-fitted grid across the circular cross-section of the cyclone body. The cyclone body was extended axially sufficiently far, it is hoped, that the downstream zero-gradient boundary conditions should have little impact on flow quantities near the inlet region. In any case, the size of this simulation made it difficult to accommodate on a shared computer. The simulation took approximately 3 hours of CPU time, on a SUN Centre 1000 computer, for 500 iterations of the outer loop of the SIMPLEC procedure described in [28]. Surprisingly, this number of iterations was sufficient to obtain adequate convergence, and the model

was much less prone to numerical instabilities than in the axisymmetric case. However, the computational burden of this simulation makes it clear that three dimensional models are still unsuited for investigating realistic hydrocyclone geometries.

7.5.3 Discussion of results

The results, as presented in Figures 7.6 and 7.7, show peaks in turbulent intensity just beyond the junction of the inlets and the cyclone body. This is to be expected; the flow at the inlets can be thought of as driving the flow within the hydrocyclone, and significant shear would be anticipated in this region. The peaks in the values of ϵ are particularly significant; with a peak intensity four orders of magnitude above the typical value elsewhere in the cyclone body. It may be that the computational model exaggerates the height of these peaks, but, even so, the effect of such localised peaks in turbulence intensity is likely to have a profound effect on liquid-liquid separation.

It is clear from these results that the standard inlet conditions for k and ϵ in axisymmetric simulations represent considerable underestimates. The simple inlet design used in this model is not representative of the state of the art in liquid-liquid hydrocyclones, and the results achieved go some why to indicating why this is: the peak in turbulence represents an undesirable level of shear, and could be expected to lead to droplet break-up and a corresponding degradation in separation performance.

Although this case is quite extreme in its demonstration of the turbulence peaks, the phenomenon demonstrated is likely to be significant in hydrocyclones with more carefully designed inlets. With increasing power, and improved geometry creation tools for CFD modelling, the most productive method for modelling of cyclones would be to combine axisymmetric models of the whole geometry, which are quick to set up and run, with 3D models of the inlet and the upper part of the cyclone. The latter class of models would allow inlet designs to be developed which minimised turbulent shear effects, and promoted an axisymmetric flow-field. These models could also be used to derive more suitable boundary conditions for the axisymmetric cases.

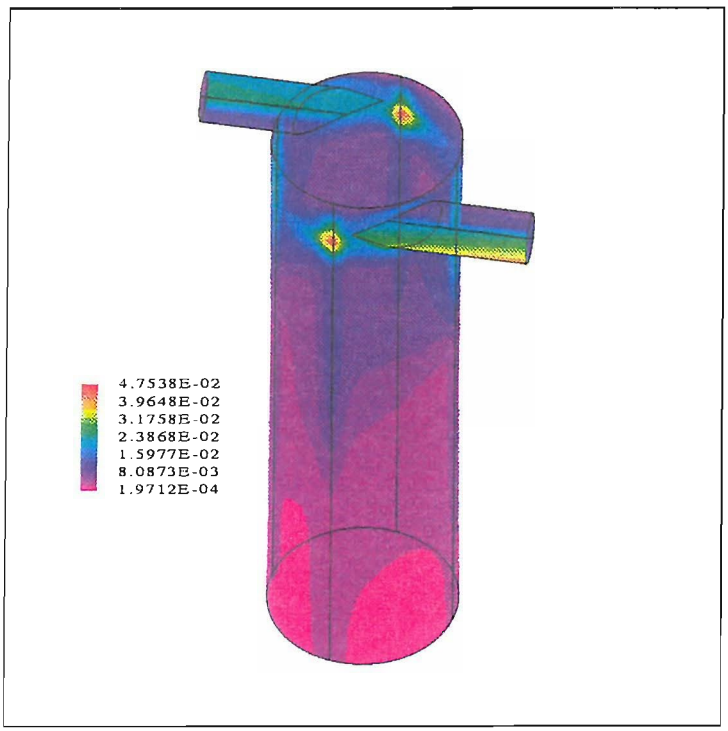

Figure 7.6: Turbulent Kinetic Energy

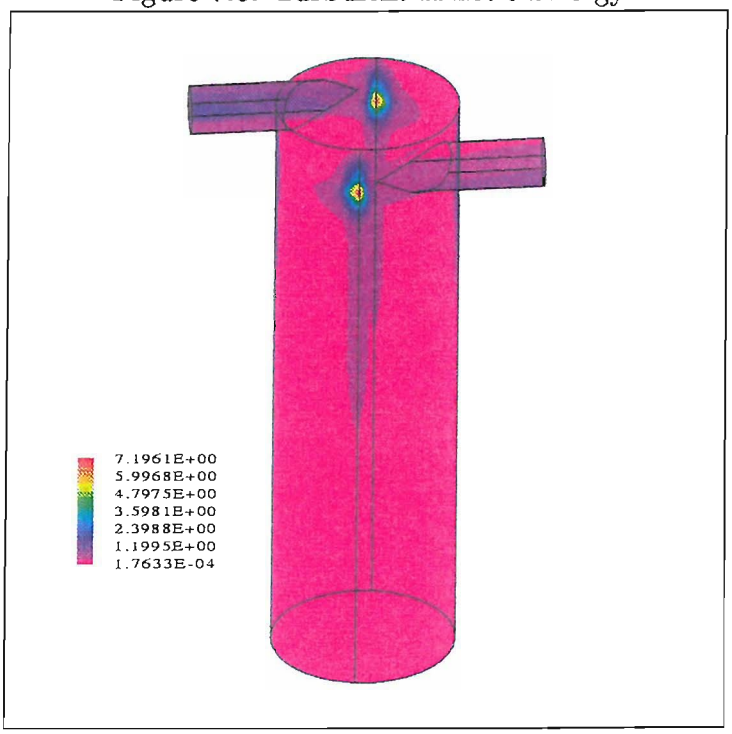

Figure 7.7: Rate of Dissipation of Turbulence Kinetic Energy

7.6 Conclusions

The shortcomings of the k–ϵ model for modelling swirling flows are well-known in the literature on hydrocyclones: each of the authors whose work is reviewed in Chapter 6

uses a more complex model. The innovation of this chapter is in the introduction of a method for quantifying the isotropy of turbulence, and thus for establishing the range of applicabilty of the k–ϵ turbulence model. The need to develop such a quantitative method was suggested to the author by A. D. Fitt, however the technique for achieving this, as well as the computations described in this chapter are the sole work of this author.

The results of this study show that for moderate swirl (swirl numbers of 0.1 or higher) the k–ϵ model is unsuitable and must be replaced by a model capable of reproducing anisotropic turbulence effects. It is interesting to note that the algebraic stress model, as implemented in CFX, although in theory capable of reproducing anisotropic flow fields, has proved impossible to converge in strongly swirling flows; a difficulty acknowledged by AEA Technology [50], the authors of the code.

It is worth noting that it is not simply the k–ϵ model which is inadequate for cyclonic flows: any isotropic turbulence model will also necessarily fail under these conditions. While empirical evidence for this phenomenon has been reported previously [3],[30], this is the first attempt known to the author in which an attempt has been made to quantify turbulence anisotropy throughout the flow-field. The definition of anisotropy given here is not appropriate only to cyclonic flows, but could be applied more generally. For instance, when planning a programme of CFD research for any turbulent flow a single model could run with the differential Reynolds' stress model, isotropy calculations performed and the results used to determine whether or not the k–ϵ model would be suitable for the remainder of the calculations.

It should be noted, also, that the definition of isotropy used here is does not itself depend on computational modelling. Both the mean velocities and correlations of turbulent velocities can be measured using, for example, laser doppler anemometry. The calculation of isotropy described above could readily be adapted to use these data.

Three dimensional simulations of the inlet region have shown that this region contains zones of high turbulence intensity, whose effect on droplet breakup is likely to be significant. While these results do not preclude the use of axisymmetric models for liquid-liquid hydrocyclones, they suggest that the boundary conditions for inlet turbulence must be reconsidered. A combination of three dimensional studies to address issues specific to the inlet region with axisymmetric models of the rest of the hydrocyclone is likely to be the

most productive method for hydrocyclone modelling in the near future.

Chapter 8

CFD modelling — Initial Work

8.1 Introduction

This chapter describes the author's own work on developing computational models of a hydrocyclone, using the commercial package CFX. It will be seen that strongly swirling flows in axisymmetric geometries are a challenge to the numerical stability of finite volume solvers. Much of this chapter is concerned with an empirical assessment of the factors which affect the convergence of the numerical method; the end result is a methodology for solving such flows which is put to extensive use in the next chapter.

Trials of different turbulence models available in CFX confirm what Chapter 6 has already suggested; the choice of turbulence model is of fundamental importance in producing a model of a hydrocyclone whose behaviour matches that observed experimentally.

As described in Chapter 6 a variety of models of hydrocyclones have been developed previously, differing mostly in the turbulence models used. While some work has been done to demonstrate the inadequacy of the k–ϵ model of turbulence in strongly swirling flows [42],it has been one of the objectives of the author's work to provide rigorous and quantitative criteria which govern the choice of turbulence model.

Computer technology continues to improve, and calculations which were prohibitively expensive only a few years ago are now routine. Various workers have sought to minimize the computational expense of their calculations, on the computers available to them, while at the same time making accurate predictions.

However, in the past limitations of time and computer power often made it necessary

to devise special purpose turbulence models for the hydrocyclone, with parameters which had to be determined from experimental data. This practice is undesirable, since we may never be sure that the models or the parameters are appropriate for other flows than those for which they have been tuned. It is an important goal in computational fluid dynamics to develop turbulence models of general utility which do not need adjusting for each new type of flow: certainly this is a necessity if computational models are to be useful in predicting the behaviour of new hydrocyclone geometries. We shall see that the differential Reynolds' stress model of turbulence is a plausible candidate for such a model, at least for use in modelling the flow in hydrocyclones.

8.2 Numerical stability

8.2.1 Iterative methods and under-relaxation

The equations to be solved for a differential stress turbulence model calculation of the flow in a hydrocyclone constitute a system of 12 non-linear coupled partial differential equations. These are discretised and solved using variants on the SIMPLE algorithm described in [28]. This a method in which the solution is iteratively improved from an initial guess by linearizing the equations at each step to calculate coefficients for a system of linear partial differential equations. These are solved, and the new values of the velocities and turbulence quantities are then used in turn to construct the coefficients of the linear equations for the next iteration.

Like many iterative methods for solving equations this method can be unstable, and a general recipe for stabilizing iterative methods is by damping the solution. in other words, when a new value for some quantity (q_{new}, say) is calculated using the old value q_{old} one replaces q_{old} not with q_{new} itself, which is a solution only to an approximation of the problem, but with $q_{old} + \frac{q_{new} - q_{old}}{D}$, where the value D is a damping, or under-relaxation, factor. As an alternative (or complement) to the use of under-relaxation factors in their pure form, in computational fluid dynamics the damping factor is often prescribed on physical grounds such the 'false time steps' described below.

8.2.2 False time steps

Although the calculations discussed here all assume that the flow is time independent, CFX allows the user to specify so-called false time steps to control the evolution of the flow.

This procedure is readily explained with reference to Laplace's equation

$$\nabla^2\phi = 0. \tag{8–1}$$

If we replace this equation with the time-dependent equation

$$\frac{\partial\phi}{\partial t} - \nabla^2\phi = 0, \tag{8–2}$$

then we may regain the original form in the limit as $\frac{\partial\phi}{\partial t}$ tends to zero. This technique may be used to solve the original equation: if we solve equation 8–2 using a time-marching technique, and the solution converges to a steady state, then this solution is also a solution to equation 8–1.

This technique can also be used for the Navier-Stokes equations. The implementation differs from a true unsteady solution in that the values calculated at each time are not stored, but only used in calculating the solution at the next time-step. Also the method used for updating the solution at the next time-step need not be designed to calculate the transient behaviour of the fluid flow, since the time marching procedure is an artifice to obtain a steady state solution, which means that a more computationally efficient method can be used for integration in time.

8.2.3 Additional Convergence Methods

Initial eddy viscosity iterations

The more sophisticated turbulence models such as the differential Reynolds' stress model are more suitable for complex flows, but they are particularly unstable in the initial stages of the flow calculation. Accordingly there is an option to use a specified number of steps with an eddy-viscosity turbulence model initially, after which the solver switches to the Reynolds' stress closure. The number of iterations is 200 by default, but can be adjusted for a particular geometry.

Deferred correction

Often numerical divergence is seeded by the behaviour of the modelled turbulence quantities. This behaviour is particularly problematic in grids with non-cuboidal cells, where the contribution from the diagonally opposite neighbouring cells must be taken into account [51]. In order to minimize this problem CFX allows the user to specify that the contribution to the equations for the turbulent quantities of cross terms should be ignored for part, or all, of a calculation.

8.3 A controlled numerical experiment

A single hydrocyclone geometry, whose dimensions were taken from Smyth [1], was used in an attempt to determine the influence and interplay of the various variables which affect numerical stability. The grid and the various control parameters described above were varied, and the number of iterations completed before numerical divergence halted the simulation was recorded for each case.

8.3.1 The grids

CFX allows only structured grids composed out of hexahedral blocks, which degenerate to quadrilaterals for the two dimensional grids of interest here. Non-orthogonal grids complicate the solution process by making it necessary to include contributions to the transport equations from neighbours not sharing an edge. However, non-orthogonal grids are a necessity in modelling hydrocyclones.

The grid along each edge, subject to consistency requirements, may be specified to be either such that the interval between successive grid points is either a constant or follows a geometrical progression. A problem with CFX is that, when two edges meet with one edge shorter than the other the algorithm for producing grids following a geometric progression produces inconsistencies in the grid. This can limit the degree of control that the user has over the grid. An attempt to circumvent this difficulty by altering the arrangement of blocks for the problem is described below.

The grids shown in Figures 8.1 to 8.5 are plotted with a scaling in the radial direction

of ten times that in the axial direction. This is necessary to allow the whole geometry to be shown, however it must be borne in mind that even the finest axial divisions used (in grid 4, Figure 8.4) has a cell aspect ratio of approximately 10 to 1, comparing the axial and radial subdivisions. The first two grids used in this experiment shared the same axial subdivisions, but with 30 (grid 1, Figure 8.1) and 40 (grid 2, Figure 8.2) radial divisions. This allows a test of whether finer radial division improves numerical stability.

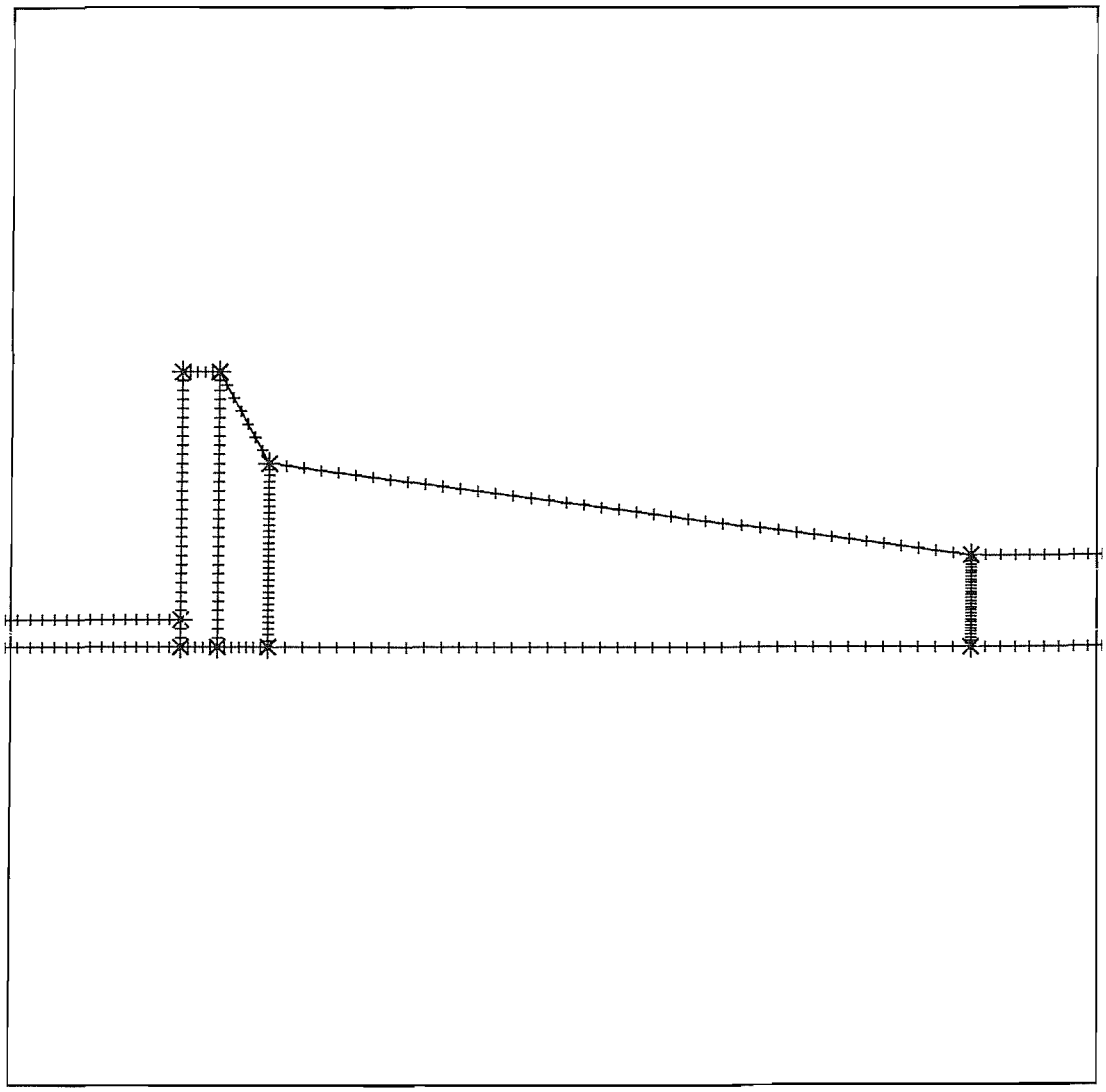

Figure 8.1: Grid 1

Grid 3 (Figure 8.3) has only 20 radial divisions, but double the previous number of axial divisions for each block.

Grid 4 (Figure 8.4) employs a new design: the block structure of overflow pipe is extended right through the hydrocyclone itself, although the wall itself ends at the top of

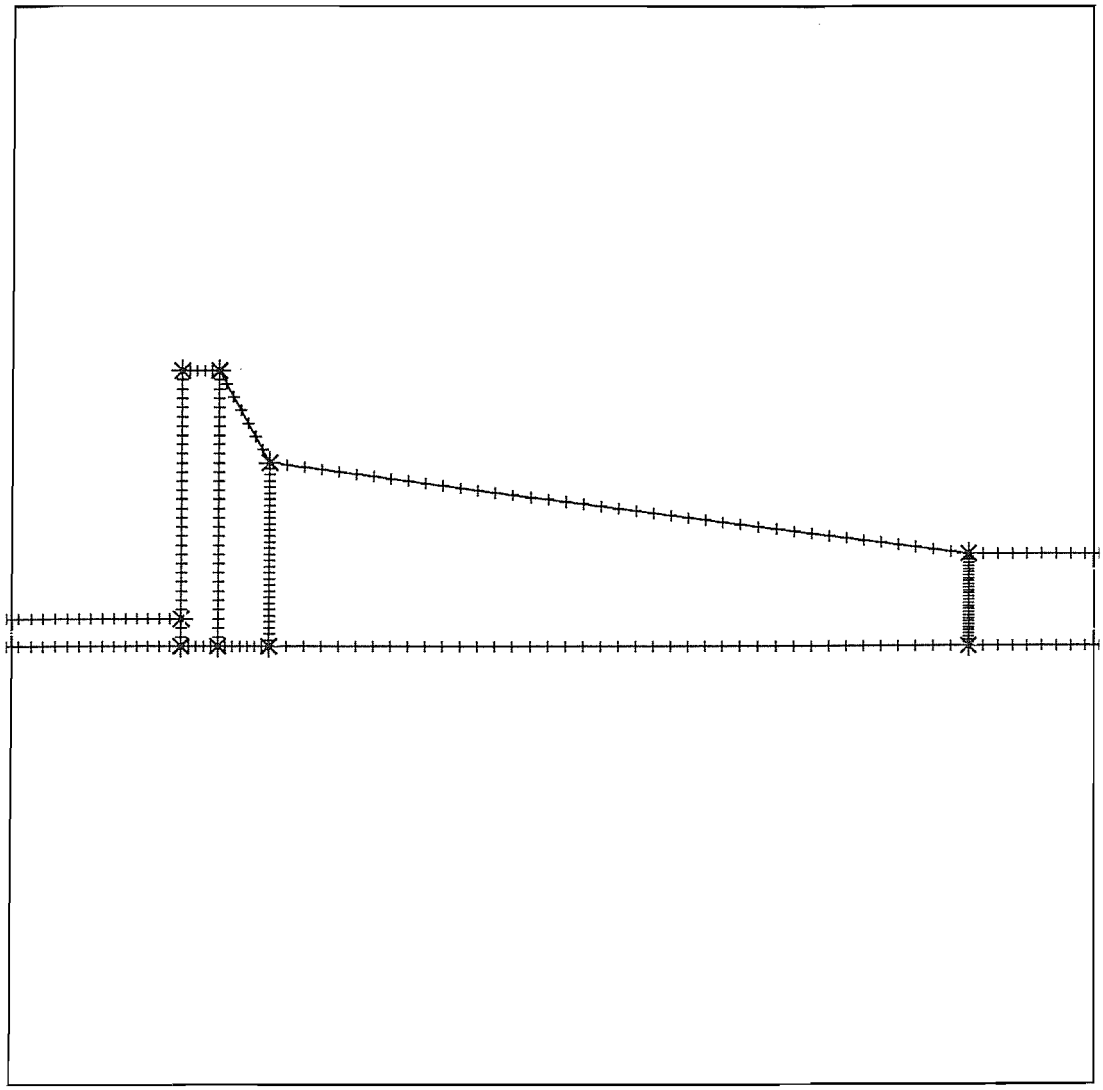

Figure 8.2: Grid 2

the cyclone since this design includesno vortex finder. This allows the grid to be varied radially on the overflow, where past experience shows that divergence can often be seeded, independently from the conical part of the hydrocyclone geometry. Results for this grid are summarised in Table 8.3

Grid 5 (Figure 8.5) is a variation on grid 4 in which the axial division of the grid on the lower conical part of the hydrocyclone is made according to a geometrical progression, so as to achieve a greater level of continuity between the grid in this section with that of the upper conical section and the straight pipe below it.

Grid 6 is in fact identical to grid five, but a FORTRAN subroutine was used to set a free vortex profile as an initial guess for the swirl velocity, for reasons outlined in section

Radial divisions	False time steps (s)	Eddy viscosity factors	Under relaxation its.	Iterations
30	10^{-3}	0.3	200	706
30	10^{-2}	0.3	200	406
30	10^{-2}	0.3	100	320
30	10^{-4}	0.3	200	1882
40	10^{-3}	0.3	200	664
40	10^{-2}	0.3	200	408
40	10^{-2}	0.3	100	303
40	10^{-4}	0.3	300	1561

Table 8.1: Results from Grids 1 and 2

8.3.2

8.3.2 Initial conditions

Observation of calculations in progress show that instability is often associated with the progression inward of swirl velocity. The initial conditions used by CFX are that the flow is everywhere at rest. The boundary conditions for the flow are then satisfied, and the flow evolves from this state. This is disadvantageous in the context of strongly swirling flows, since initially a strong axial flow is established, in order that the fluid entering from the inlet is removed via one or both of the outlets, and the superposition of a swirling flow on this pre-established axial flow leads to convergence problems.

False time steps (s)	Under relaxation factors	Eddy viscosity its.	Iterations
10^{-3}	0.3	300	2000
10^{-2}	0.3	100	1680
none	0.3	50	1573

Table 8.2: Results from Grid 3

Accordingly, an attempt was made to begin the simulation with a more realistic swirl velocity profile. It was assumed that a free vortex swirl velocity profile would be suitable,

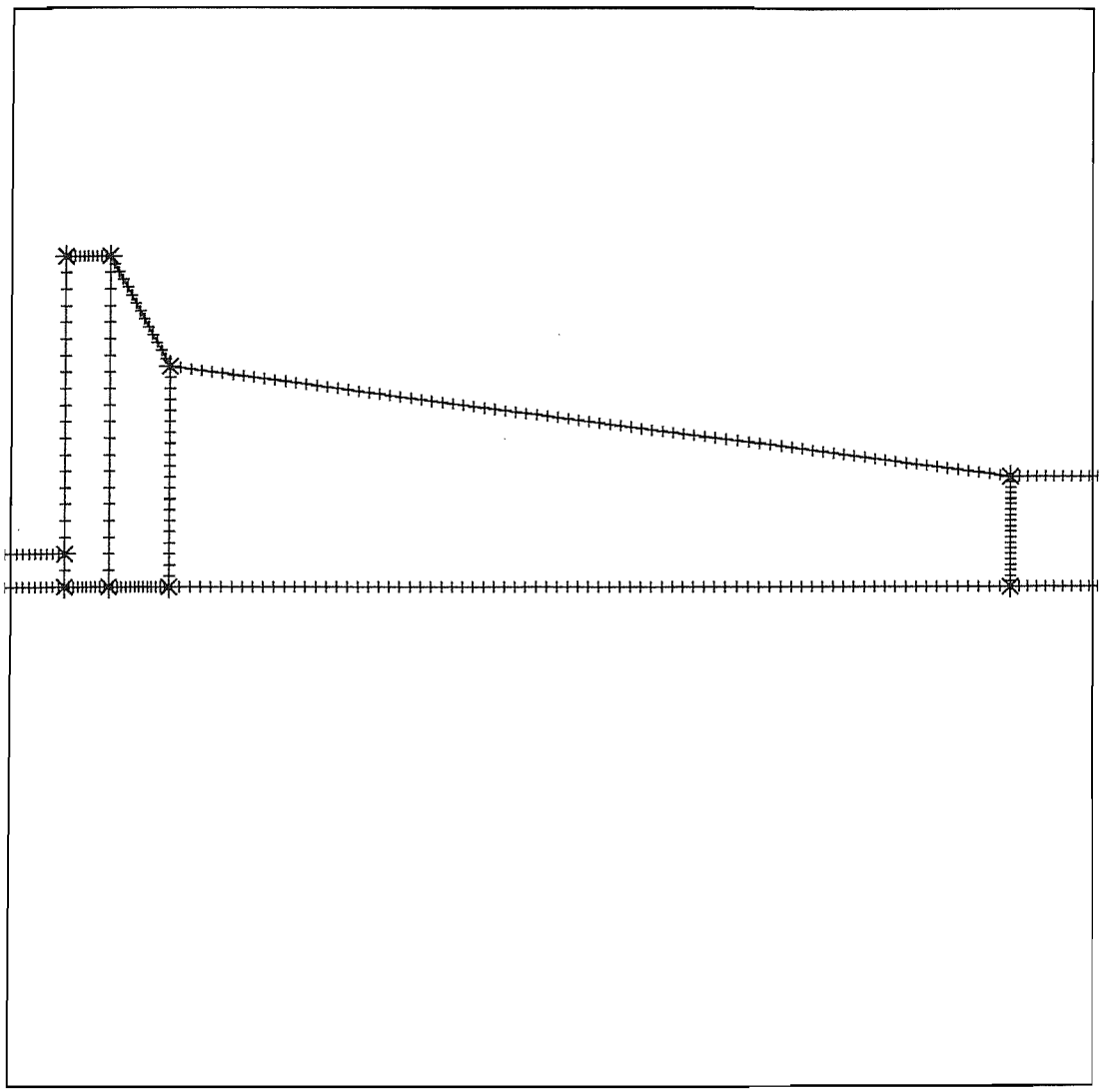

Figure 8.3: Grid 3

since the viscosity of the fluid near the axis would soon damp the singularity which would otherwise appear there. In fact the method used by CFX of storing the velocities at the cell centre means that the value of swirl velocity at the cells adjacent to the axis will initially only be unphysically large, rather than infinite, there.

A problem with this approach is that the turbulent quantities in the interior of the geometry are also considered to start at zero, and the transition between zero and the values which they should eventually obtain is coupled to the values of the velocity. Using the default initial guesses the turbulent quantities should evolve in tandem with the velocities; in this case it would be preferable for the turbulent quantities to evolve with as little effect as possible on the velocities, at least until realistic values are obtained.

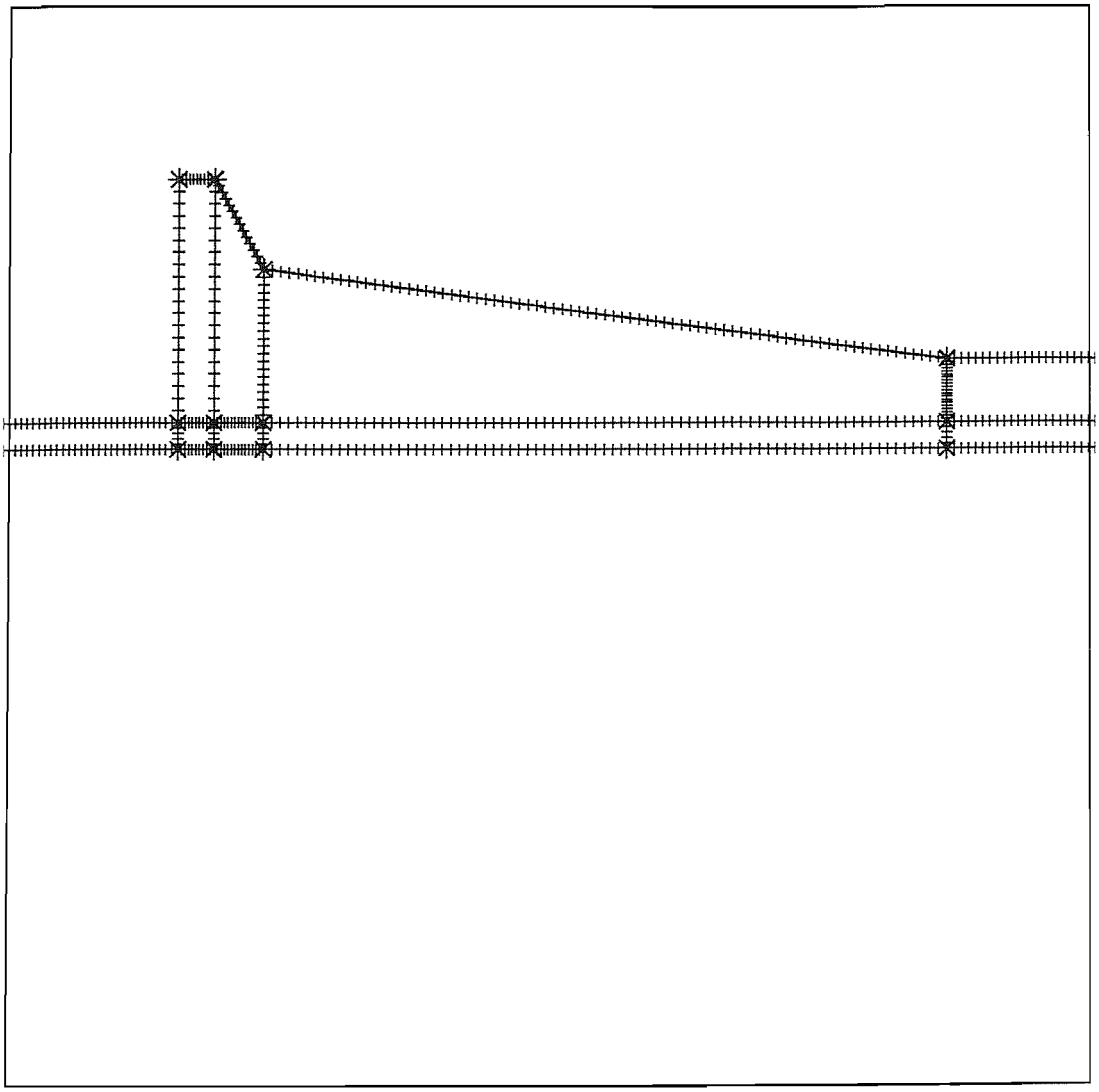

Figure 8.4: Grid 4

8.3.3 The results

The results for grids 1 and 2 are shown in Table 8.1. We may see that, in these cases, a setting of under-relaxation factors less than the default of 0.7 is necessary for the calculation to progress any distance at all. As might be expected, starting with many iterations of the eddy viscosity model — which does not give free vortex profiles for swirl velocity — is not a successful strategy.

It may be inferred from this table that increasing the number of radial subdivisions makes the calculation process less stable. This is consistent with the view that calculations should be more stable as the aspect ratio of the grid approaches unity. Unfortunately, with such an anisotropic geometry as that of the dewatering hydrocyclone the

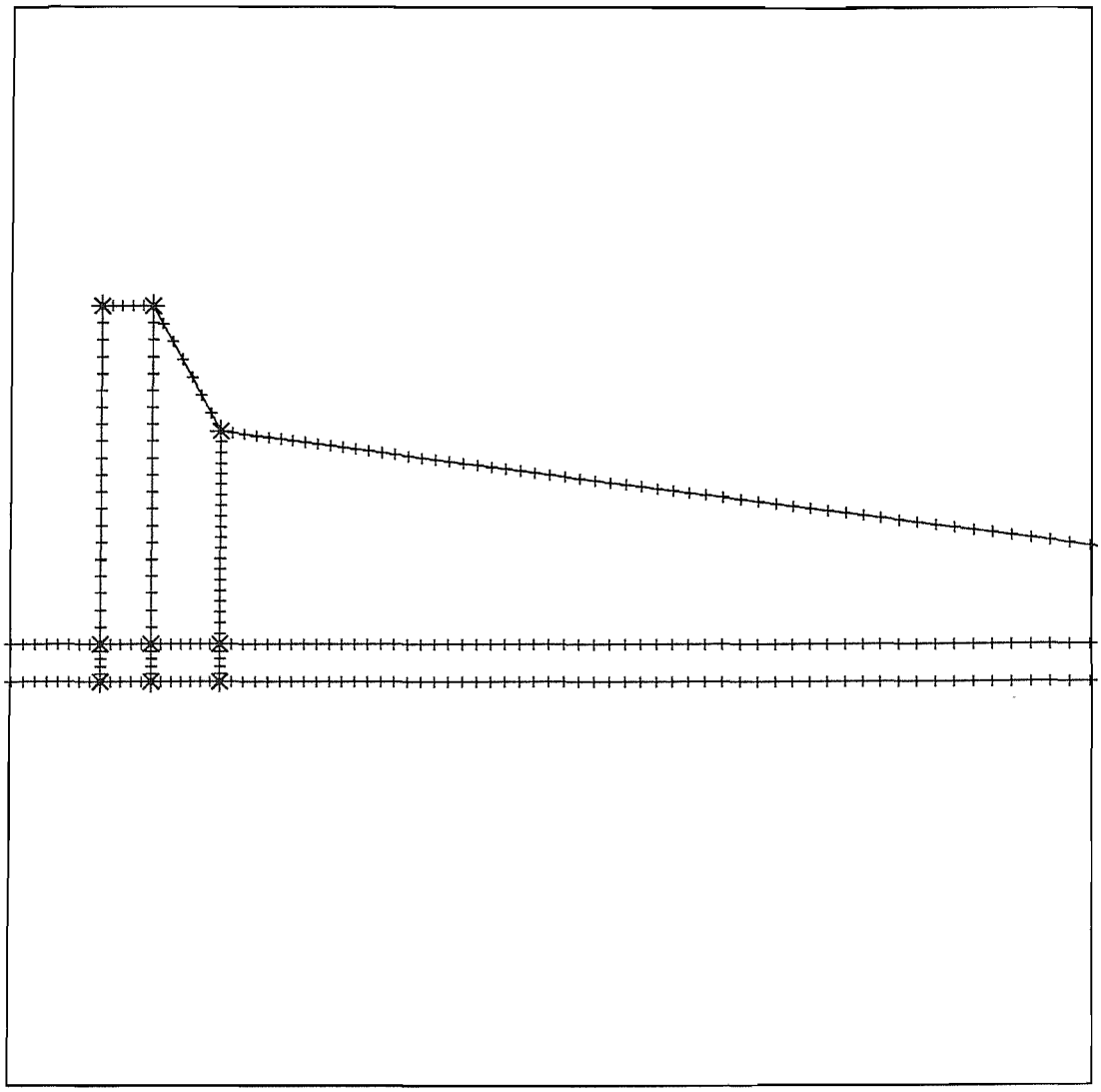

Figure 8.5: Grid 5

computational size of such a grid makes such aspect ratios infeasible. Grids 1 and 2 have cell aspect ratios of approximately 30 and 40 respectively, and it may be inferred that such ratios are not conducive to numerical stability. This is unfortunate, since it makes more sense to concentrate the grid in the radial direction, where steep gradients may be expected, at the expense of the axial direction, in which changes will be more gradual.

Grid 3

As Table 8.2 shows, this grid (shown in Figure 8.5) lends further weight to the hypothesis that the grid should be as isotropic as possible. The improvement in numerical behaviour of this grid over grids 1 and 2 is marked.

False time steps (s)	Under relaxation factors	Eddy viscosity its.	Iterations
none	none	200	279
10^{-2}	none	50	367
10^{-3}	none	200	956
10^{-4}	none	200	2000

Table 8.3: Results for Grid 4

False time steps (s)	Under relaxation factors	Eddy viscosity its.	Iterations
none	0.3	50	365
10^{-3}	0.3	10	292
10^{-3}	0.3	100	989

Table 8.4: Results for Grid 5

Grid 4

This grid, which has 5 radial divisions in the radius of the overflow pipe, and 20 outside this region, and shares its axial division scheme with grids 1 and 2, was also used to experiment with using the default values of the under relaxation parameters for all variables. This was done because it was believed that the increased resolution of the grid near the axis would in itself improve the stability of the calculation, and thus that the values of the under-relaxation factors chosen would be of less significance.

The results for this grid summarised in Table 8.3 do appear to bear this out: for similar values of false time steps the number of iterations completed is greater than that of either of grids 1 and 2.

Grid 5

Results for this grid are summarised in Table 8.4. The improvement with this grid over grid 4 is not sufficient to conclude that the degree of continuity between axial subdivision schemes at the transition from the upper to the lower conical section of the hydrocyclone is significant.

8.3.4 Grid 6

Run	False time steps (s)	Eddy viscosity its.	Under relaxation factors	Iterations
1	None	30	0.3	87
2	10^{-1}	50	0.3	81
3	10^{-1}	100	0.3	83
4	10^{-1}	10	0.3	83
5	10^{-2}	0	0.3	69
6	10^{-3}	50	0.3	62
7	10^{-3}	10	0.3	78
8	none	0	0.7	23
9	10^{-3}	5	0.7	28
10	10^{-3}	10	0.7	29
11	10^{-3}	20	0.3	90
12	10^{-4}	20	0.3	65
13	10^{-4}	50	0.3	58
14	10^{-4}	50	0.3	58
15	10^{-4}	50	0.3 (velocities only)	264

Table 8.5: Results for Grid 6

Results for grid 6 are summarised in Table 8.5. In all these calculations the false time steps were applied to all transport equations. There is some scope for applying the false time step procedure to some equations, but not others, and in fact this approach has been more successful.

With the sixth set of calculations — those using a free vortex as an initial guess — more success was achieved by using under-relaxation only on the main flow equations.

8.3.5 Transient solutions

Why a transient solution to a steady problem ?

Instead of using false time steps as described above, it is possible to solve the flow as a transient problem. This is an attractive possibility since the difficulties in convergence are attributable to the evolution from a poor set of initial conditions. CFX provides adaptive time stepping for transient flows, which is a useful extension and likely to be more suitable than using the fixed false time steps.

The most obvious drawback with this approach is that the time taken to achieve convergence may be longer than with the assumption of steady state. However,the high levels of damping in the steady state simulations described above make it seem reasonable to try.

Results

This approach was not a success. The possibility of adaptive control of the time step meant that the simulations were kept from divergence throughout the full extent of the run. However the results, although far from full convergence, did not appear to be making progress towards a sensible solution. In one instance the pressure appeared to have settled to a value of -10^9 Pascal throughout the cyclone, and flow was consistently entering the cyclone through the overflow exit.

8.4 A final model

Using the insight derived from the above experiments another grid was designed. This grid had the block arrangement of grids 4 and 5, and also a more refined mesh in the axial direction. After 12 thousand iterations, using false time steps of 10^{-3} seconds initially, and later time steps of 10^{-6} as the solution began to show a tendency to diverge, the flow field was converged to a reasonable extent. Study of the intermediate flow field showed that there was an unphysical peak in the azimuthal velocity in the overflow pipe which is likely to have been the cause of the numerical instability. However, this region is a considerable distance downstream, and thus unlikely to contaminate the validity of the

flow field within the cyclone body.

Figure 8.6 shows the vector field in a dewatering hydrocyclone. It may be seen that there is a strong flow towards the underflow outlet near the wall of the hydrocyclone, as well as a central region of axially reversed flow. Additionally, the vectors are coloured by the magnitude of swirl velocity which would otherwise not be shown since it is perpendicular to the plane of this cross-section. It may be seen that the peak tangential velocities are about midway between the inlet and the vortex finder, and we conclude that the Rankine combined vortex structure has developed.

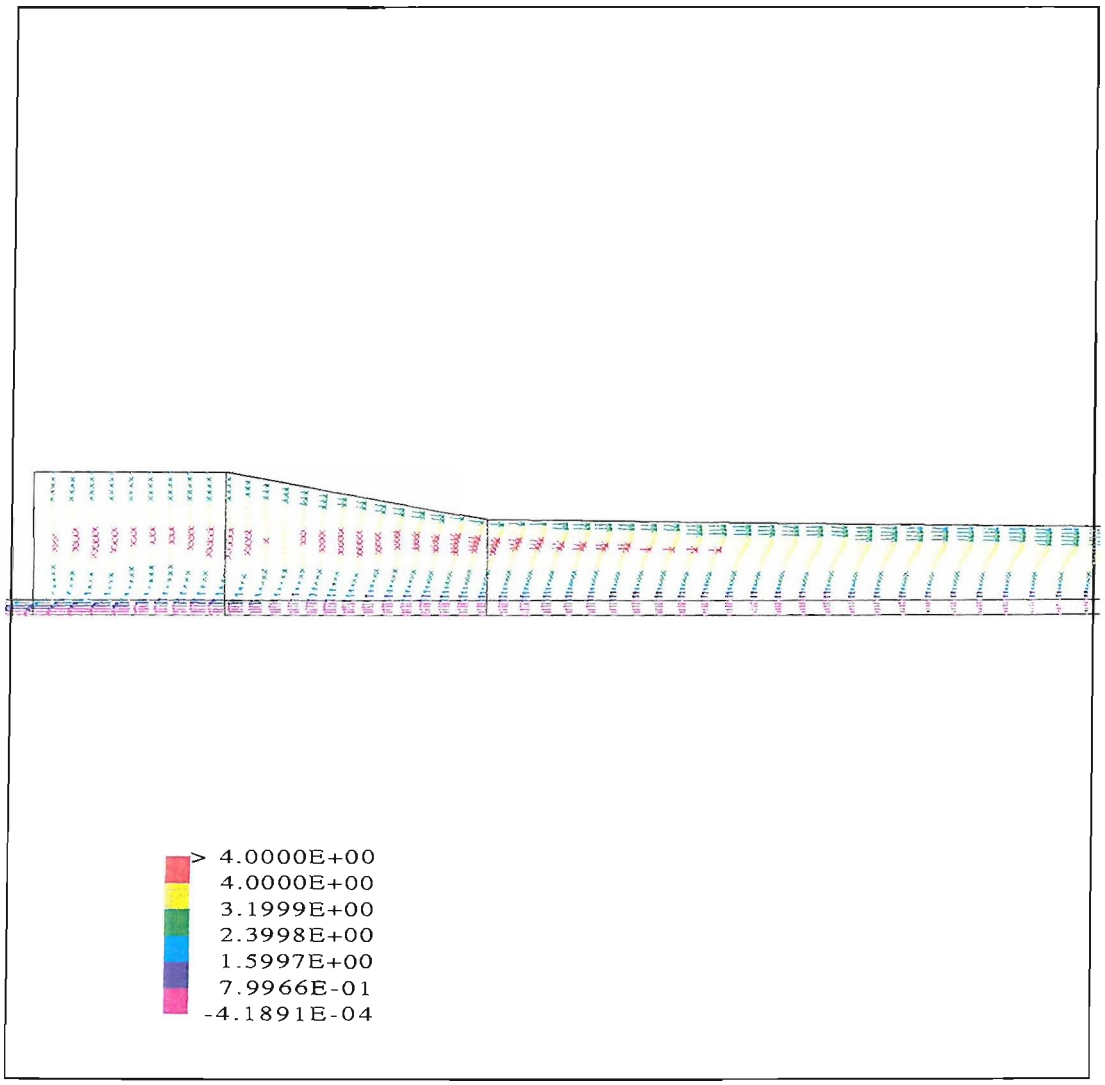

Figure 8.6: Swirl Velocity in a Dewatering Hydrocyclone

8.5 Conclusions

The flow inside a hydrocyclone remains a challenging problem for computational fluid dynamics. The relative simplicity of the geometry in comparison to other machinery of engineering interest is offset by the difficulty of attaining convergence which arises from the combination of the differential Reynolds' stress model and the high azimuthal velocities within the flow field.

The computation must balance the desire to achieve a converged flow field quickly with the need to avoid the numerical divergence which can result from rapid changes in the guessed values of the variables in the iterative solution process. A series of computational experiments was performed in an attempt to determine an optimal set of relaxation factors which would allow the solution to proceed as quickly as is possible without causing divergence. In addition, the effect of the discretization of the hydrocyclone geometry on the success of the computation was investigated.

These experiments shows that:

- The aspect ratio of the computational grid is the most important factor affecting the convergence of the solution. The minimum axial-to-radial aspect ratio used in this study was about 10, and this is limited by available memory on the computers used. This aspect ratio is calculated at the top (and thus the widest part) of the hydrocyclone; as the hydrocyclone narrows with the same number of radial subdivisions the cell aspect will increase dramatically. This is undoubtedly an important reason for the difficulty encountered in converging models of liquid-liquid hydrocyclones relative to those of more conventional design. The geometries described in Chapter 7 where much easier to model successfully than those in this Chapter. Solving this problem mostly amounts to a need for greater computer power – both RAM and CPU speed need to be increased over that used in these studies for studies of slender hydrocyclone geometries to be a routine matter.

- The choice of damping mechanism and the coefficients chosen for each of the equations are capable of having a profound impact on the numerical stability of the CFD calculations. For divergence to be averted false timesteps of 10^{-3} seconds have been found to be necessary, together with under-relaxation factors of 0.3.

- The use of a grid refined at the axis offers some improvement in numerical stability, although less than the effect of changing the typical aspect ratio of a grid element.
- The imposition of a free vortex swirl velocity profile as an initial condition appears from this evidence to be too crude, since the variables have not evolved to this point together.
- The use of a number of initial iterations using an eddy-viscosity model to allow a flow-field (albeit one unrepresentative of fully developed cyclonic flow) to become established seems to be necessary before switching to the differential stress model. On the basis of the models described in this chapter 200–300 seems to be an appropriate number of iterations for this.
- There is some evidence, from the examination of the computed flow fields from calculations where divergence had begun, to suggest that the divergence can be instigated by the inward movement of swirl velocity reaching the join between the upper and lower conical sections of the hydrocyclone. This is understandable since here two distinct non-orthogonal grids meet.

It seems unlikely that any combination of under-relaxation factors, false time steps and grid will allow the solution to proceed without any human intervention. However, a successful computation of the flow field in a de-watering hydrocyclone geometry has now been accomplished, with only the occasional adjustment of damping parameters.

Now that this has been achieved, it is possible to begin to consider testing the model for plausibility against experimental data. One important aspect of hydrocyclone behaviour which it is important to be able to reproduce accurately is the variation in the split ratio (defined as the ratio of flow exiting via the overflow to that exiting via the underflow) as a function of the relative pressures at these outlets. If the model is accurate in this respect then it is desirable to consider turbulent two component models; these, after all, are fundamental to the proposed goal of developing a cyclone model with useful predictive capacity.

Chapter 9

CFD modelling of a dewatering hydrocyclone

9.1 Introduction

Having discussed the development of a methodology for creating CFD models of hydrocyclones in the previous chapter we now turn to the application of these techniques to a hydrocyclone geometry of industrial interest.

This chapter is concerned with a series of models of the design used by Sinker [2] for dewatering use, the 35NS18 geometry shown in figure 9.1.

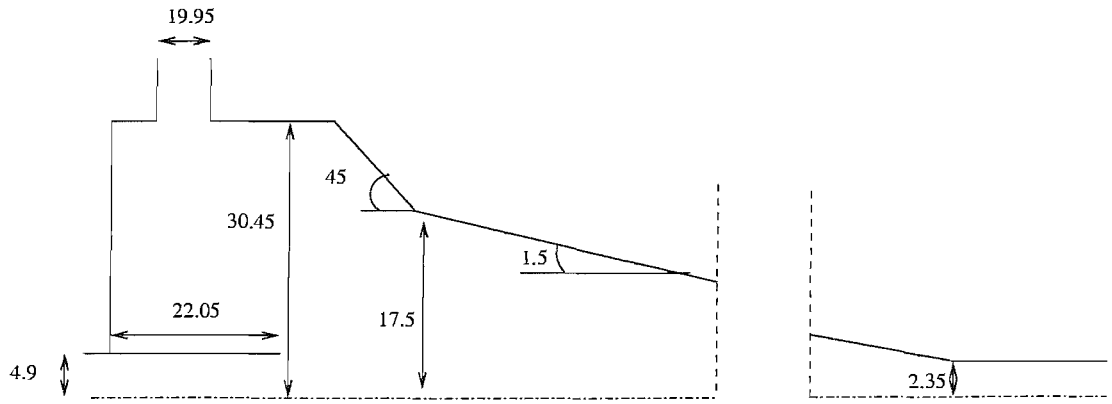

All lengths given are in mm,
and all angles in degrees.

Figure 9.1: The 35NS18 hydrocyclone geometry

9.2 Questions to be addressed

In modelling this geometry we use CFD to answer several questions of interest to cyclone designers, namely

Definition of core radius. The radius of the inner core of the flow in a hydrocyclone can be defined in two different ways; either as the radius for which the tangential velocity attains its maximum, or as the radius at which the vertical velocity is zero. The former definition gives the radius where the centrifugal force will be largest, while the fluid inside the radius of zero vertical velocity will be discharged at the overflow exit of the hydrocyclone. If these two radii are significantly different separation performance will be sub-optimal.

The relationship between split ratio and pressure difference between outlets. Since the dewatering hydrocyclone runs sealed and without an air core the split ratio can be controlled by adjusting the pressures at the overflow and underflow by means of valves downstream of the exits. Matching the split ratio to the inlet concentrations of the two components is important in achieving optimal separation performance, so understanding this relationship is of considerable operational value.

The effects of split ratio on the flow-field. Computational models of the hydrocyclone produce a complete description of the flow-field inside the device. Analyzing the effect of split ratio on the velocity components inside the device can yield a useful qualitative understanding of its effect on separation performance.

Optimization of cyclone performance through geometric changes The ultimate goal of this work is to use CFD techniques to design hydrocyclones with better performance than those currently existing by altering geometric parameters. This chapter will discuss the feasibility of such a programme of optimization.

In addition the use of Lagrangian and Eulerian techniques for multi-component flow modelling will be discussed.

9.3 Modelling the NS35S18 hydrocyclone

9.3.1 Boundary conditions

All the single component models discussed in this chapter use the 35NS18 geometry running with water at 60 litres per minute. The geometry was modelled in a plane, using the assumption of axial symmetry.

The circular inlet of the physical hydrocyclone is of diameter 19.95 mm; accordingly a toroidal region of this height was used in the computation. The radial velocity was set to give the correct volumetric flow-rate, Q, for such an inlet, while the tangential velocity was from that in the (physical) inlet pipe, assuming plug flow. This gives the inlet boundary conditions:

$$\begin{aligned} v_r &= \frac{Q}{\pi D_s} = -0.262 \text{ ms}^{-1} \\ v_\theta &= \frac{4Q}{\pi D_2^2} = 3.199 \text{ ms}^{-1} \\ v_z &= 0 \end{aligned}$$

Two kinds of boundary conditions were used at the outlet; the fractional mass flows at each outlet and the pressure at the outlet. The former boundary conditions were used with CFX, while the latter were used in some supplementary models using the commercial code FLUENT.

The Differential Reynolds' Stress model for turbulence was used for all the models discussed in this chapter.

9.3.2 Comparison of CFD codes

The use of CFX for modelling hydrocyclones is described in detail in the previous chapter. Towards the end of the period of research described in this thesis the author had the opportunity to use the commercial CFD code FLUENT 4.5 to model the same geometry. This code, like CFX, is a structured finite-volume solver of the type described in [28], and offers broadly similar functionality.

One specific advantage of FLUENT is that it allows pressure outlet boundary conditions to be specified in such a way that any flow entering the domain at such an outlet can have turbulent quantities specified. While it is undesirable to have flow entering via an outlet it is even less desirable for this to cause numerical divergence. Inspection of CFX data showed that flow entering the domain via the overflow outlet often occurred as a symptom of a model in the process of diverging. Since the divergence was usually first observed in the equations for turbulent quantities (particularly ϵ) it is quite likely that this inflow was, at least partially, responsible for the observed divergence.

The much better stability of the otherwise similar FLUENT models under these conditions adds further weight to this hypothesis. The relative ease of convergence of FLUENT, and the more powerful hardware available to run it combined to produce several converged solutions in the space of a few days.

Apart from this, essentially the same methodology was used to develop axi-symmetric solutions using FLUENT as was used for CFX.

9.4 Results

9.4.1 Split ratios and pressures

The relationship between split ratio and pressure drop is shown in Table 9.1, where the split ratio, F, is defined to be the proportion of the volumetric flux through the hydrocyclone which reports to the overflow exit:

$$F = \frac{Q_{\text{overflow}}}{Q_{\text{inlet}}}. \tag{9–1}$$

It should be noted that the 'natural' split ratio of this hydrocyclone, defined as the split ratio when the overflow and underflow pressures are the same, is between 10% and 20%. There is thus a strong bias towards the underflow exit, and to achieve values of F above 50% a strong pressure gradient is required from the underflow to the overflow.

Also, the boundary condition used in the CFD models is applied uniformly to each of the exits, whereas in practice there would be a radial pressure gradient to balance the effects of the swirl at the outlet. These two effects combine to produce the physically unrealistic effect of outlet pressures at the underflow greater than those at the inlet. The

pressures recorded in this table are those at the outer extreme of the outlet pipe, measured 10 diameters downstream of the exit of the cyclone itself, and thus these unphysical pressure values are unlikely to contaminate the flow upstream, within the hydrocyclone. To demonstrate this consider that the values of pressure at an axial station 0.5 m downstream from the cyclone top wall in the case with a nominal back pressure of 15×10^5 Pa range from 1×10^5 Pa (at the axis) to 6.4×10^5 Pa (at the cyclone wall. This axial station is near the underflow exit of the hydrocyclone, and the pressures remain below the inlet value of 6.98×10^5 Pa, as we would expect, and show the appropriate variation with radius.

Split ratio (%)	Pressure (Pa)			ΔP_{io}	ΔP_{iu}
	Underflow	Overflow	Inlet		
10	3.72×10^5	2.81×10^5	6.36×10^5	3.55×10^5	2.64×10^5
20	6.77×10^4	1.134×10^5	4.08×10^5	2.95×10^5	3.413×10^5
48.5	-1.93×10^5	2.1×10^3	3.76×10^5	3.74×10^5	5.69×10^5
53.4	1.96×10^5	2.3×10^3	1.094×10^5	1.07×10^5	-1.866×10^5
67.9	9.72×10^5	1.3×10^3	5.38×10^5	5.37×10^5	-4.34×10^5
85.8	14.59×10^5	6.1×10^3	6.98×10^5	6.92×10^5	-7.61×10^5

Table 9.1: Pressure drops and split ratios for CFD models of 35NS18

In [2] a set of experimental data is presented for this geometry running with gas oil with values of F between 60% and 90% at 60 l/min. For this case ΔP_{io} remained approximately constant at 2 Bar, while ΔP_{iu} increased from 1 Bar, for F=90% to 4 Bar at F=60%.

The density of gas oil is 850 kgm^{-3}, compared with 1000 kgm^{-3} for water, so that we would expect the pressure drop to be higher using water. However, even with this correction the effects of the pressure boundary condition in the FLUENT model preclude a direct comparison. If we assume that the FLUENT boundary condition adds a constant pressure to the outlet then we may attempt a comparison.

The experimental data for gas oil gives an increase of 3 Bar in ΔP_{iu} to produce a change in F from 0.9 to 0.6. Correcting this by $\rho_{\text{water}}/\rho_{\text{oil}} = 1000/850 = 1.18$ gives a a change in pressure drop of 3.5 Bar over this range. The computational results above

for water predict an an increase of ΔP_{iu} of 3.27 Bar to produce a change of F from 0.86 to 0.68. While this results does not constitute conclusive agreement between the CFD model and experiment, it is encouraging.

9.4.2 Flow field

For each of the CFD models the values of the axial and tangential velocities were extracted at the axial stations $x = 0.03$ m, $x = 0.1$ m and $x = 0.2$ m.

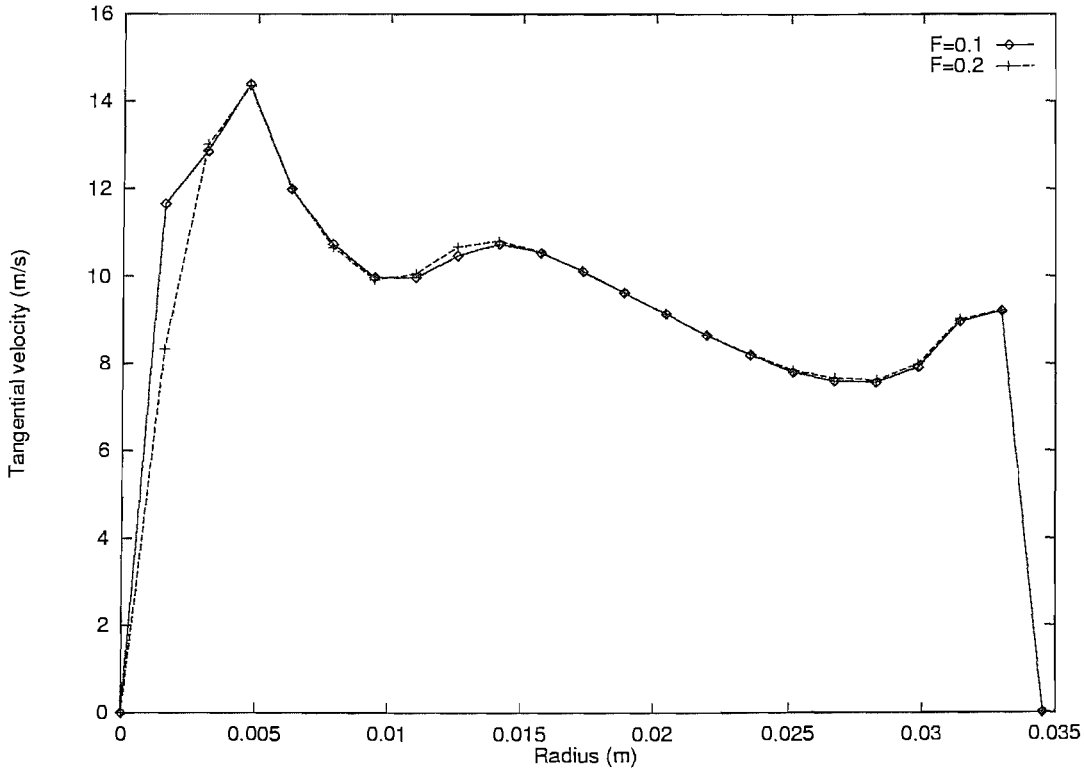

Figure 9.2: Tangential velocity at $x = 0.03$, using CFX

Figures 9.2 and 9.3 show the results for tangential velocity at $x = 0.03$. Both codes show a tangential velocity profile similar to the Rankine combined vortex, with tangential velocity increasing rapidly from zero at the axis to a peak a few millimetres away and then tailing off. The FLUENT simulations show a more straightforward decay of v_θ compared to those preformed with CFX. This is likely to be attributable, at least in part, to the better convergence and somewhat finer mesh of the FLUENT simulations.

We see that there is reasonable good agreement in these graphs on the radial location and value of the maximum tangential velocity. This is shown to be between 13 and 17 ms^{-1}, or 4.1 to 5.3 times the value at the inlet.

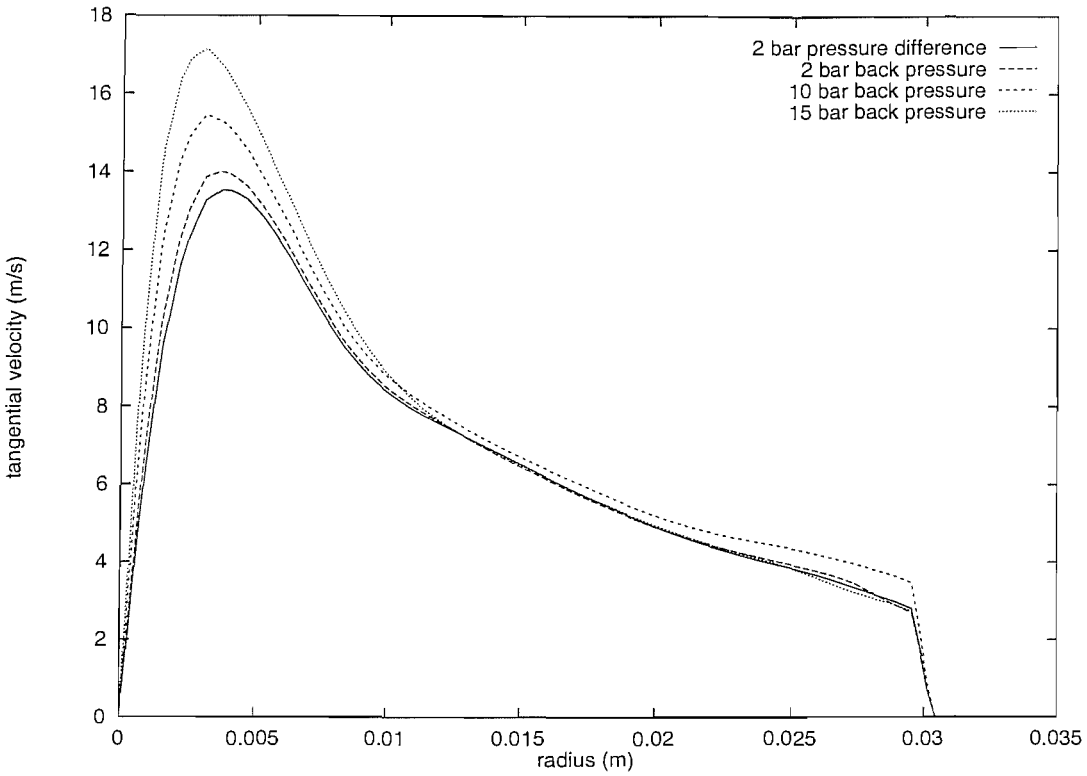

Figure 9.3: Tangential velocity at $x = 0.03$, using FLUENT

In addition the FLUENT results show that the maximum value of the tangential velocity increases as the back-pressure from the underflow to the overflow, and thus the split ratio F, is increased.

The axial velocities at this axial station are shown in Figures 9.4 and 9.5. Note that in all of the simulations described in this chapter the underflow exit is located at the most positive x position of the simulation. This means that flow towards the overflow corresponds to a *negative* axial velocity on the graphs displayed in this section.

The CFX results of Figure 9.5 reproduce well the expected flow towards the underflow in the near wall region. The FLUENT results do not show this as clearly. Both codes show a region between $R = 10$mm and $R = 20$mm where flow is towards the underflow. The results for the FLUENT cases with 10 and 15 Bar back-pressure, for which $F > 60$ %, show the axial velocity profiles which come closest to the flow one might expect inside a cyclone, with a pronounced flow reversal from $R < 10$mm to the axis. For smaller values of F the reversed axial flow is increasingly reduced in velocity towards the axis. The CFX results for small split ratios show an even more complex behaviour near the axis: there is an 'outer' region of flow within the core which flows towards the overflow, within

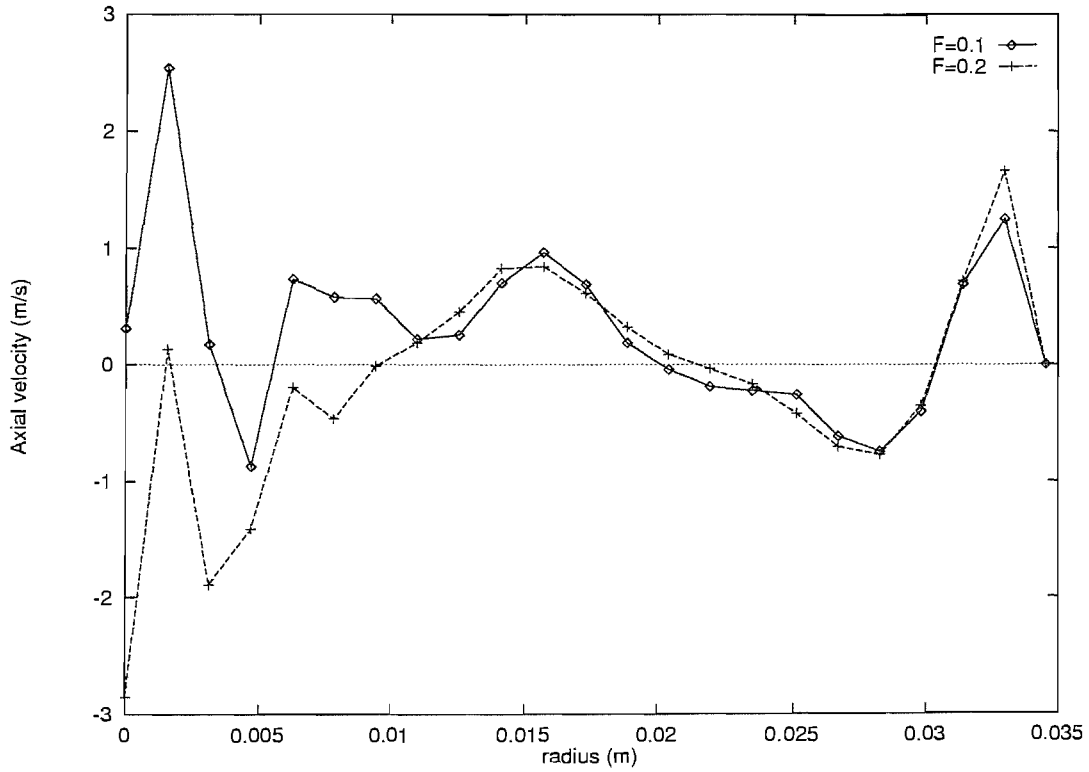

Figure 9.4: Axial velocity at $x = 0.03$, using CFX

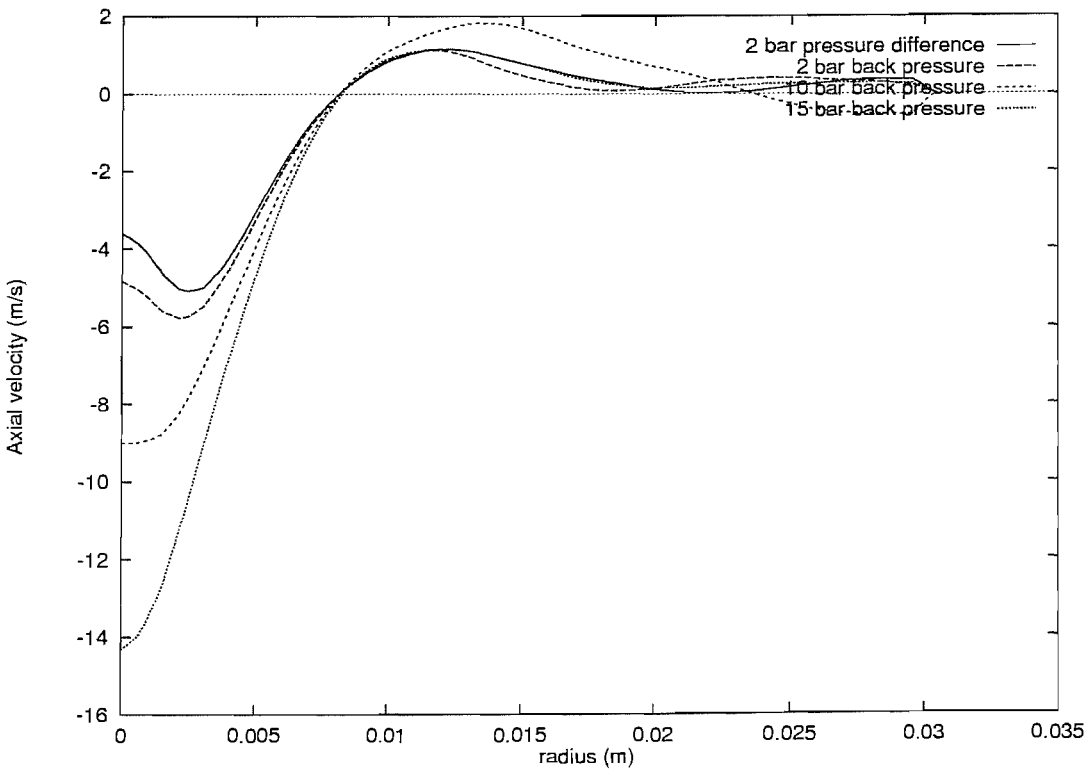

Figure 9.5: Axial velocity at $x = 0.03$, using FLUENT

which (for the lowest value of F) there is a region flowing towards the underflow. For $F = 0.2$ the flow is only rest brought to rest, and the innermost region once again flows towards the overflow. Such features of the flow are likely to be detrimental to separation efficiency: we expect the less dense component to collect near the axis, so any reduction in the velocity towards the overflow in this region will decrease the efficiency with which this component is conveyed to the overflow. Re-reversal within the core could also cause some of the less dense component (in this case, oil) to be discharged from the underflow, and the sharp axial velocity gradients predicted by the CFX simulations will give rise to turbulent shear forces in this region which could cause the breakup of water droplets in this region (since the flow near the axis is unlikely to be pure oil), reducing the likelihood of the water droplets being eliminated from the oil stream.

The velocity profiles shown below at $x = 0.1$mm are qualitatively similar. The CFX velocity profiles in Figures 9.6 and 9.8 are somewhat smoother at this axial station. The decay in tangential velocity away from the axis is still more marked in the FLUENT simulations (Figure 9.7), however.

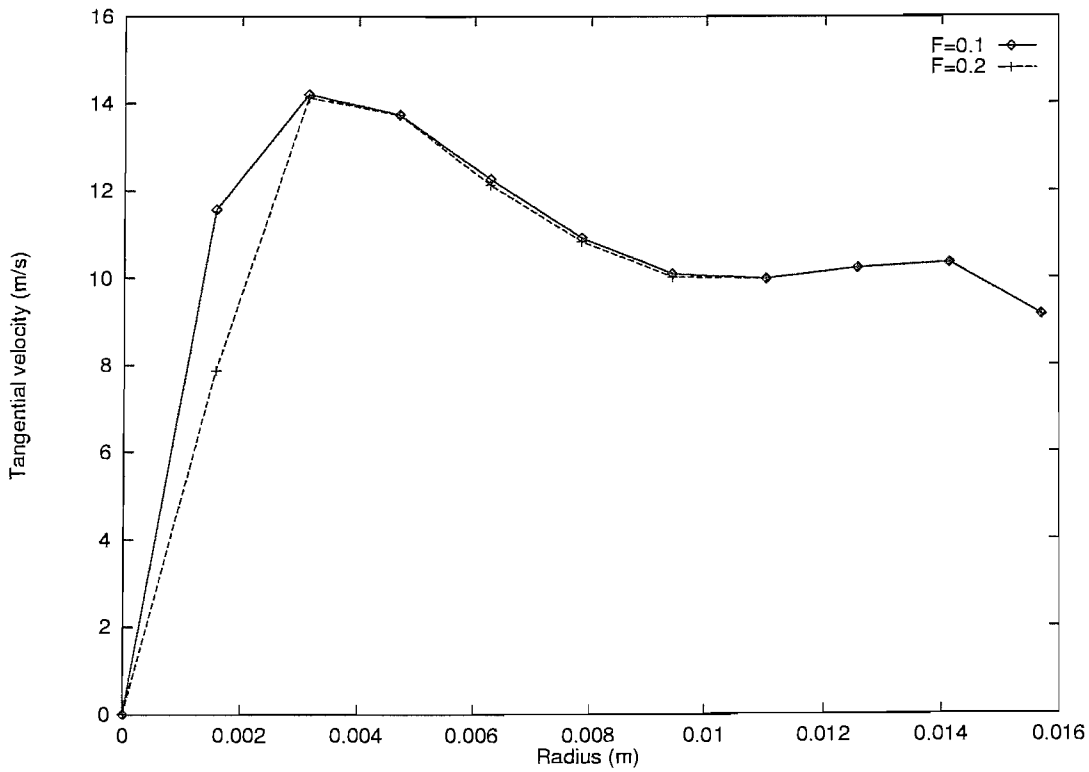

Figure 9.6: Tangential velocity at $x = 0.1$, using CFX

At this axial station the axial velocities predicted by FLUENT (Figure 9.9) and those

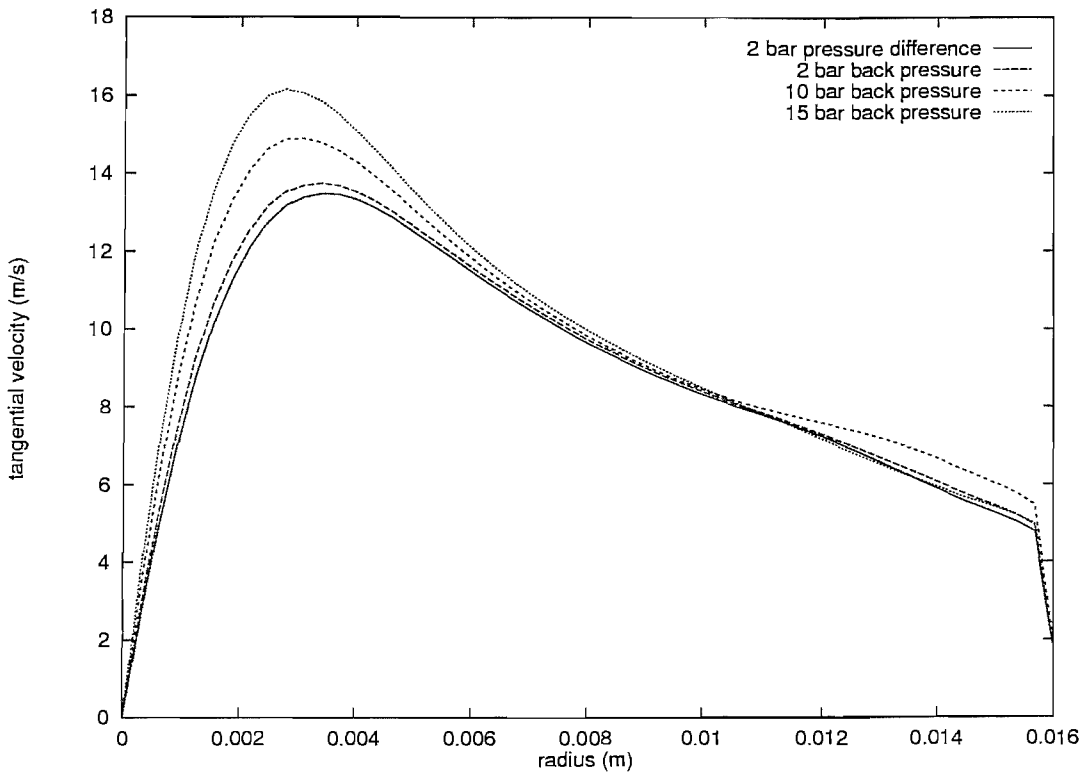

Figure 9.7: Tangential velocity at $x = 0.1$, using FLUENT

of the CFX models (Figure 9.8) are in better agreement in the near wall region; both show a flow towards the underflow in this region increasing in velocity until just inside the wall before the flow is brought to rest at the wall boundary.

The axial velocity profiles at this station have similar features to those at $x = 0.03$ – the reversed flow at the axis is well defined for the highest split ratios, but is reduced as F decreases, with both CFX simulations showing annular regions with flow in opposite directions.

Figures 9.10 and 9.11 show the axial and tangential velocities for five axial stations for the FLUENT model with a 2 bar (positive) pressure difference between the overflow and underflow exits.

Figure 9.10 shows that the radial position at which the axial velocity is zero moves inwards as the underflow outlet is approached. However, it may be seen from Figure 9.11 that the location of the maximum tangential velocity varies very little over the length of the hydrocyclone.

Figure 9.12 shows the axial velocities plotted against radial distance non-dimensionalised with the maximum radius at each axial station. This graph shows that for the three

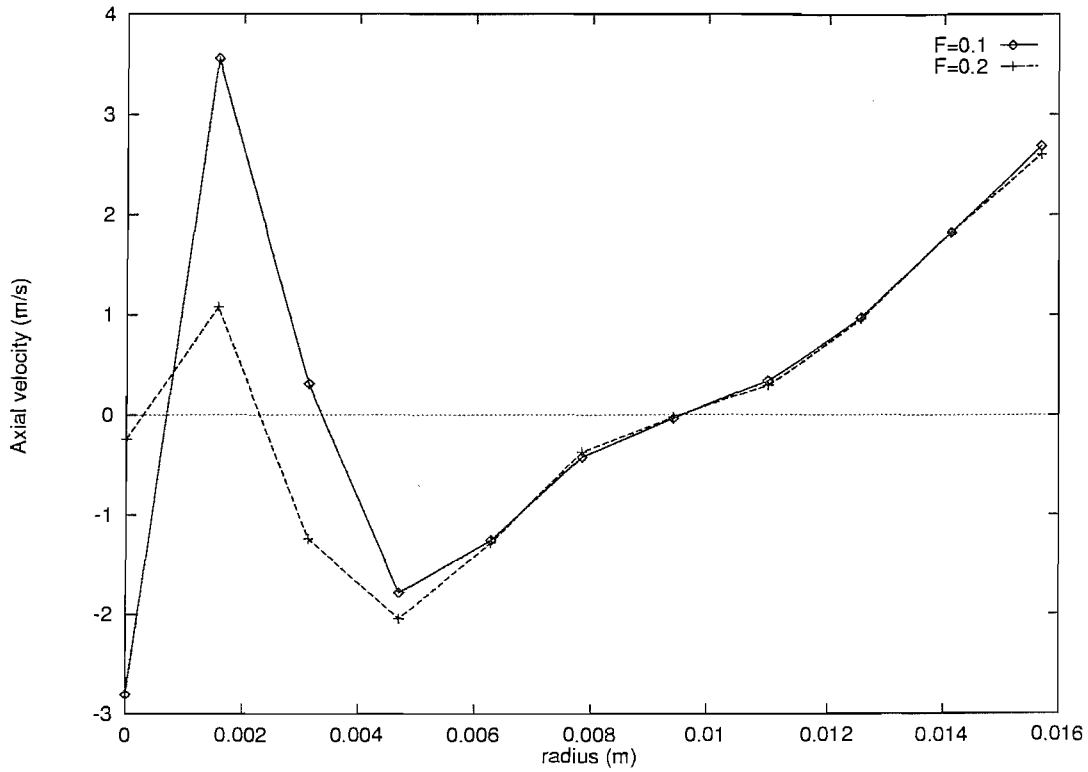

Figure 9.8: Axial velocity at $x = 0.1$, using CFX

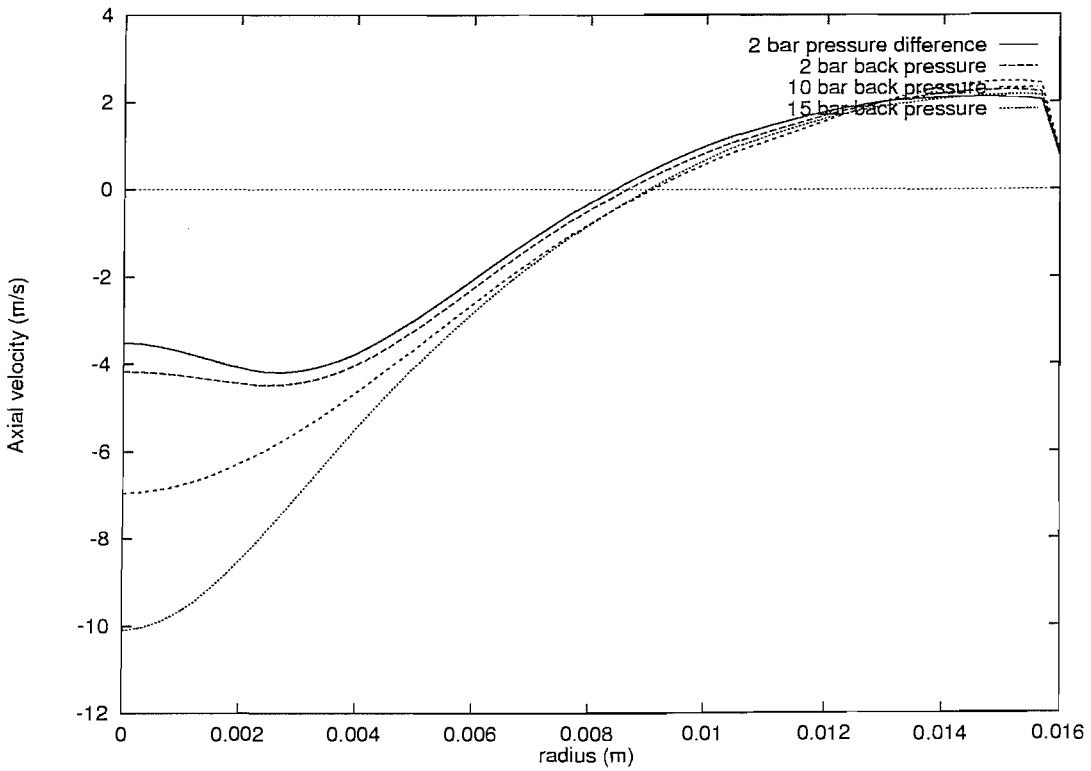

Figure 9.9: Axial velocity at $x = 0.1$, using FLUENT

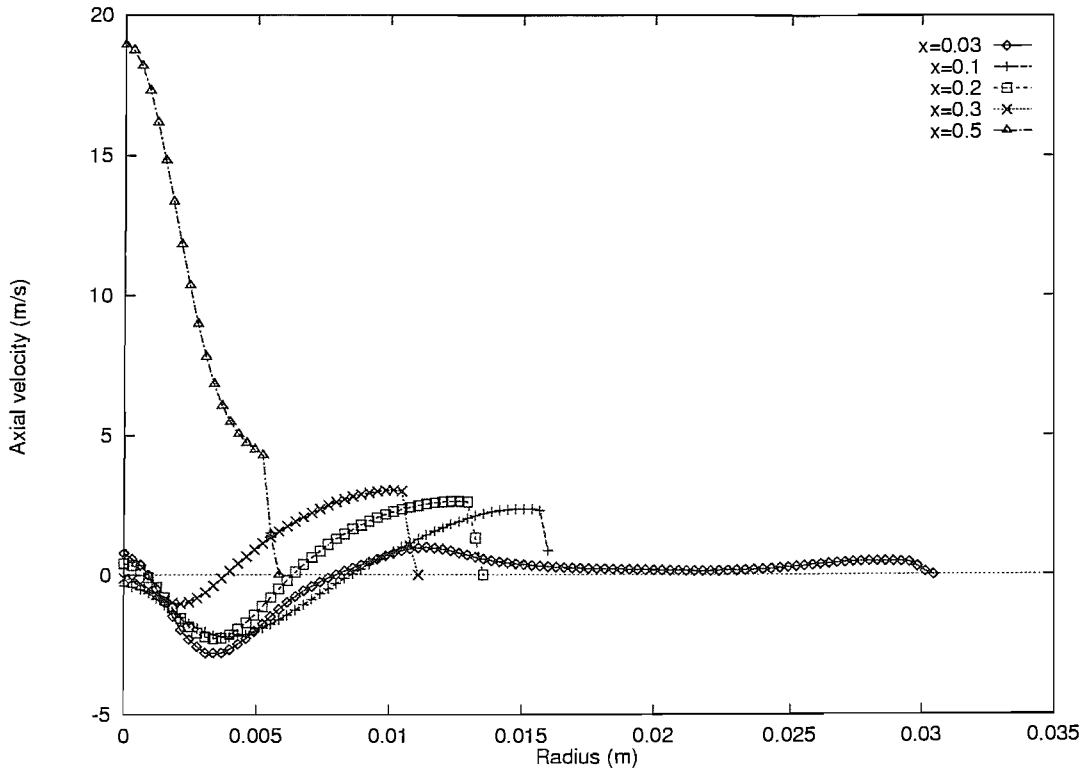

Figure 9.10: Axial velocities for 2 bar pressure drop, using FLUENT

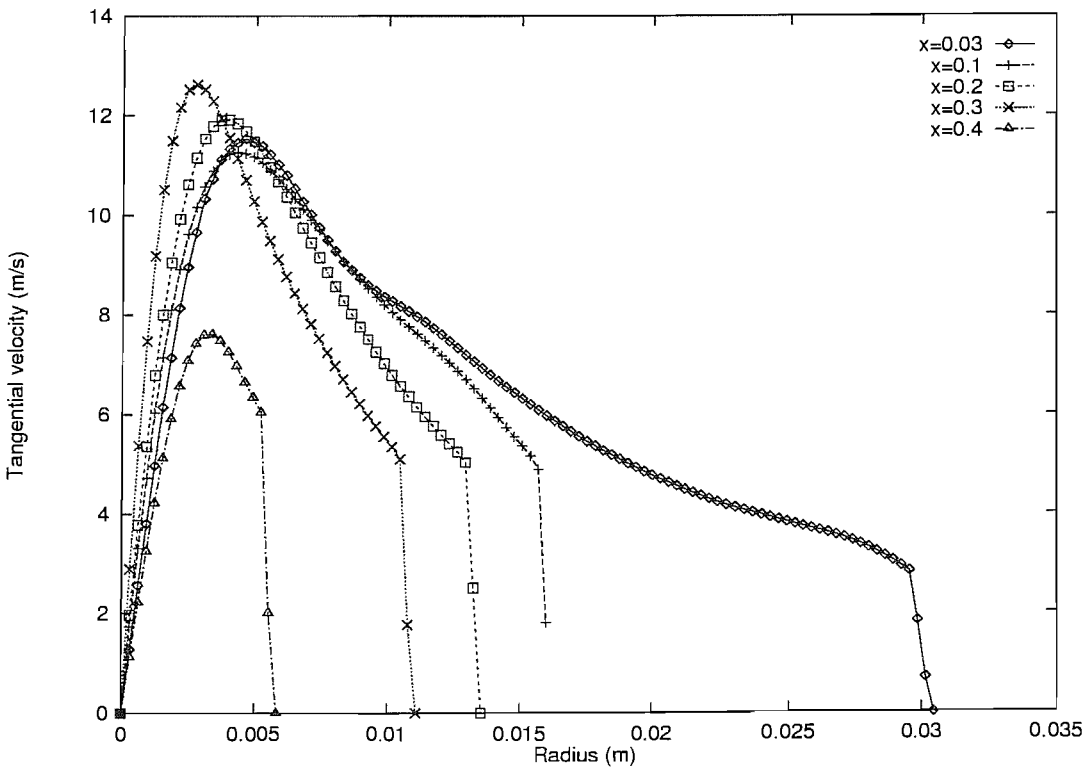

Figure 9.11: Tangential velocities for 2 bar pressure drop, using FLUENT

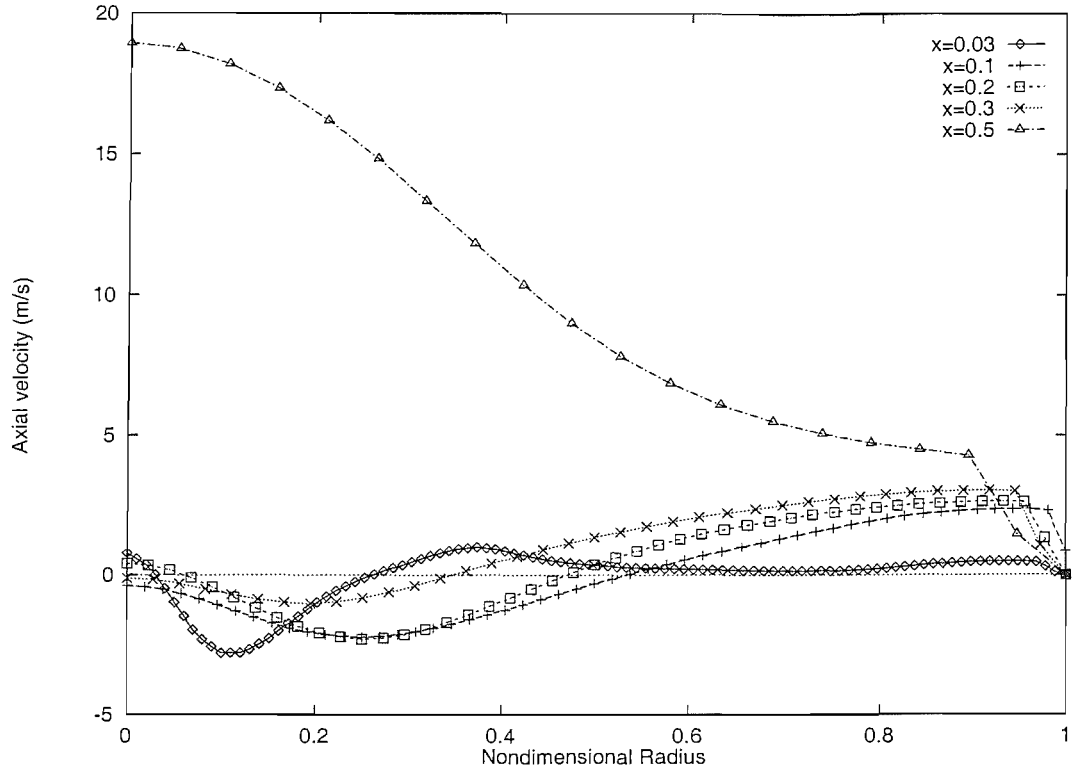

Figure 9.12: Axial velocities vs. dimensionless radius for 2 bar pressure drop, using FLUENT

middle axial stations, away from the effects of the outlets and the top wall of the hydrocyclone, the axial profiles are quite similar.

9.4.3 Core radius

The above plots show that the two definitions of the radius of the core flow give different results. The definition which requires the axial velocity to be zero will also depend on the axial station to be considered. In quantifying these radii the axial station $x = 0.1$m has been selected. Table 9.2 gives shows R_{v_θ}, the radius of the maximum tangential velocity, and R_{v_z}, the radius of zero axial velocity, for each of the models described.

This table shows that R_{v_θ} is less than R_{v_z} towards the top of the hydrocyclone for each of the models considered. This means that flow can be conveyed to the overflow exit without having passed through the full centrifugal force which the flow can generate. Separation would be better served if R_{v_z} were less than R_{v_θ}. It is quite possible that alterations to the geometry could achieve this.

F (%)	R_{v_θ} (mm)	R_{v_z} (mm)
10	5.0	5.8
20	5.5	9.5
48.5	3.4	8.4
53.4	3.4	8.6
67.9	3.1	8.9
85.8	2.7	8.9

Table 9.2: The radius of the core flow, calculated two different ways

9.5 Multi-component modelling

9.5.1 Discrete particle tracking

In the mineral processing community it is common to treat a liquid/solid flow by first solving for the fluid flow field in the absence of any particles, and then to determine the motion of the particles by releasing particles from the inlet and following their trajectory.

This method is only appropriate for systems in which particle-paricle interactions can be neglected (i.e., the discrete phase comprises no more than 1% by volume of the flow). This is not the case in the flows of interest to this author, but the simplicity of this modelling approach made it desirable to use this technique to gain insight into the likely behaviour of individual droplets despite its shortcomings in describing the physics of the flow when both of the components are present in significant amounts.

Consider a particle of mass m moving with (vector) velocity $\mathbf{v}_p$, subject to a force $\mathbf{F}$. Its motion will be governed by Newton's second law of motion, so that

$$m\frac{d\mathbf{v}_p}{dt} = \mathbf{F}, \tag{9–2}$$

This method was used by Bloor and Ingham [5] in an analytical context and discussed in section 3.7, it may be recalled that they modelled $\mathbf{F}$ in equation 9–2 as consisting only of difference between the "centrifugal" force induced by density difference in a swirling flow field and the drag force.

Similarly in CFX the force $\mathbf{F}$ is also modelled as a sum of forces:

$$\mathbf{F} = \mathbf{F}_D + \mathbf{F}_P \tag{9–3}$$

The drag force F_D is given by

$$\mathbf{F}_D = \frac{1}{8}\pi d^2 C_D |v_{rel}| v_{rel}, \tag{9–4}$$

where C_D is a drag coefficient, and v_{rel} is the velocity of the particle relative to the fluid and the pressure gradient force $\mathbf{F}_P$ is given by

$$\mathbf{F_P} = -\frac{1}{4}\pi d^3 \nabla.P. \tag{9–5}$$

Since the radial component of the pressure gradient provides the centripetal force to balance the rotation of the continuous fluid, the same pressure gradient will cause the less dense particle to be accelerated inwards to the centre of the hydrocyclone.

It is possible to use this method to find particle concentrations by considering the release of many different particles, and this information can be used to calculate a new estimate for the viscosity of the bulk fluid. This process can be incorporated into the main flow solution algorithm in order to account for the influence of particle motion on the main flow.

9.5.2 Tracking particles with CFX

In order to create an axi-symmetric model in CFX it is necessary to define and mesh a geometry in 3 dimensions, such that the mesh in the Z direction is one cell thick. The two sides of the Z cells are then identified in CFX's command language, and the Z direction is identified with θ. However, when used to track particles CFX produces a file in which an entry is made every time that a particle crosses the boundary of a cell in the computational grid, including the Z boundaries.

As a particle moves towards the axis of the hydrocyclone its tangential speed will, typically, increase, while the distance in the θ direction that it has to travel to cross this boundary decreases with its radial position. Consequently, particle tracking in CFX is dominated by the writing of huge files so that

1. Particle tracking is very slow.

2. Data produced for particle tracks are too large to manipulate.

3. The computer available to the author on which to run CFX did not have sufficient disk space to create particle tracks.

9.5.3 Eulerian multi-phase modelling

An introduction to the subject of Eulerian multi-phase modelling was given in Section 4.3, in the context of the flow within a (two dimensional) circular region. As was explained there, such models represent the two components by means of a volume fraction field which represents the "probability" in some sense of a spatial position being occupied by either component. It is not yet established how models of turbulence can be incorporated into such a model, particularly the complex differential Reynolds' stress models which this thesis has argued are necessary to describe strongly swirling flows such as are found in a hydrocyclone.

Nonetheless, CFX incorporates a two component model and allows the use of a differential stress model in conjunction with it.

However, such models require twice as much memory per cell as single component models, and take approximately three times as long per iteration. In addition, when a cyclone geometry was modelled the computation failed before a single iteration could be completed. It seems that the two component model, with an axisymmetric mesh, has difficulty in modelling small axial outlets.

9.6 Conclusions

9.6.1 Achievements

An axisymmetric model has been presented for the single component flow in a dewatering hydrocyclone. The relationship between the two possible definitions of the axial core of the flow has been investigated, and this has lead to the conclusion that the separation performance of the 35NS18 design of hydrocyclone could still be improved.

The relationship between the pressures at the outlets and the split ratio has been determined, and the effects of these parameters on the flow field has been described.

It has been shown that the flow inside this geometry of hydrocyclone splits cleanly into a two streams discharging into the two outlets only if the split ratio, F is above 60%.

9.6.2 CFD as a design tool

The computer power necessary for CFD to become part of the design process is now becoming widely available. The difference in performance between the (single user) SGI Octane workstation equipped with 512 megabytes of RAM on which the later FLUENT simulations were performed and the shared University computer used for the earlier CFX simulations reduced the time taken to converge a solution from several days to a few hours.

This quantitative increase in speed also enables a qualitative change in working methods – since the solution develops rapidly it is possible to monitor its progress and draw conclusions from its behaviour in a way that was previously impractical. Such rapid feedback is a crucial factor in being able to adjust the many parameters governing the numerical aspects of the solution so as to develop a methodology for successfully and reliably converging solutions.

With sufficient computational resources, a wide range of geometries could be investigated so that the effects of varying the geometrical parameters of the cyclone could be established. Such a process could lead to cyclone designs better than any available now for specific conditions.

Throughout the period when most of the work described in this thesis took place the lack of computer power available to the author has been the limiting factor in performing such an analysis. The necessary computational facilities are now sufficiently readily acquired that such a programme of research is now feasible in a time-scale which would allow CFD to become an integral part of the design process for hydrocyclones.

Chapter 10

Conclusions and Directions for Future Work

10.1 Introduction

The initial goal of this project was to develop and validate a model of two component flow in a dewatering hydrocyclone. While this has not proved feasible with the resources of time and money available, many lessons have been learned about the use of computational fluid dynamics in complex flows. This chapter summarizes what has been learned about the current state of the art in modelling such flows.

10.2 CFD – current achievements

CFD is now increasingly practical to calculate hydrocyclone flow fields. However, care is needed on the following points:

- The choice of turbulence models is crucial to an accurate numerical model of a hydrocyclone. The k–ϵ model is inadequate, since it assumes isotropy of turbulence; the differential Reynolds' stress gives results which compare well to experimental studies, and is computationally usable on today's computers.
- The solution grid plays an important role in the stability of the calculation, but *a priori* results are not available for the strongly coupled systems of differential

equations in many variables used in hydrocyclone modelling, so empirical methods are required.

- The choice of under-relaxation factors to allow the solution to converge in a reasonable time, while avoiding numerical instability is difficult. These parameters must also be empirically determined; some usable values have been established, but they may need to be varied for different problems.

- Particle tracking is practical, although the assumption of axisymmetry complicates the setting of inlet conditions. The current state of the art (as implemented in CFX) does particle tracking separately from the main flow solution, and models turbulence as isotropic stochastic disturbances of the particles' velocities, which is not ideal in the case of a hydrocyclone.

- Models for the flow of two immiscible liquids, in a regime where turbulence is anisotropic are not at all well developed. CFX uses a simple generalization of the single phase model for this case, which is not extensively validated. This model certainly predicts separation of two components of differing densities, but whether the predictions of the internal flow field are accurate it is not currently possible to say.

Models have been developed which can successfully predict the relationship between the axial pressure drop (which is set by the hydrocyclone operator) and the split ratio in a hydrocyclone with single phase flow. Predictions of particle classification efficiency may also be made, although these match experimental data less well for larger volume fractions of water injected.

Two phase models of the hydrocyclone are hampered by the tentative nature of the theory, numerical instability in the solution of the model, and a shortage of experimental data against which to validate the results.

10.3 Tomography

Electrical impedance tomography is a difficult specialist technique, requiring equipment and expertise beyond that available in this study. However, the limited experimental

studies carried out have shown that the conductivity of oil and water mixtures can be used to determine the gross volume fractions of the two components, using an effective medium theory. This means that electrical impedance tomography techniques are certainly appropriate for this problem, but it is would be necessary either to invest in some expensive hardware, or to collaborate with researchers specializing in this area.

It would be possible to develop an online monitoring and control system which used tomographic sensors to determine the concentrations within a hydrocyclone, in real time, and used these to set be used for online monitoring and control, with improved equipment.

10.4 Two phase modelling and validation

The use of a full electrical impedance tomography system would make it possible to validate two phase flow models. At the moment such models for liquid-liquid flows are much behind their single phase counterparts, partly because they are necessarily more complex, but also because there is a shortage of experimental data with which to compare predictions. The obstacles in the way of developing a practical two phase model of a hydrocyclone are substantial; such effects as the turbulence-induced breakup and coalescence of particles must be considered, as well as the possibility of different components being continuous in different regions (as well as the regions of oil droplets embedded in water droplets themselves embedded in larger oil droplets which may occur during the transition between these two regimes). It is also quite possible to develop mathematical models which seem physically reasonable, but give rise to unphysical requirements for boundary conditions.

In practice it would be advisable (and probably necessary) to start developing models for this problem in the simplest possible setting, using tomography to measure concentrations; one might begin with turbulent pipe flow, and then progress to adding a swirl component, and gradually increasing this to levels that allow separation to occur. This would make it possible to postpone the treatment of anisotropic turbulence models until a validated k–ϵ model for this problem had been developed.

While it may be difficult to attract industrial sponsorship for such a program, it is the author's opinion that the fundamentals of turbulent liquid-liquid flows require

considerable study before real progress can be made on complex applications.

Bibliography

[1] I C Smyth. *Cyclonic Dewatering of Oil.* PhD thesis, University of Southampton, 1989.

[2] A B Sinker. *An experimental Study of Droplet Stability and Separation Performance in Dewatering Hydrocyclones.* PhD thesis, University of Southampton, 1995.

[3] J H Hargreaves and R S Silvester. Computational fluid dynamics applied to the analysis of deoiling hydrocyclone performance. *Trans. I. Chem. E.*, 68:365–383, 1990.

[4] D F Kelsall. A study of the motion of solid particles in a hydraulic cyclone. *Trans. I. Chem. E.*, 30:87, 1952.

[5] M I G Bloor and D B Ingham. Theoretical investigation of the flow in conical hydrocyclones. *Trans. I. Chem. E.*, 51:36–41, 1973.

[6] M I G Bloor and D B Ingham. Turbulent spin in a hydrocyclone. *Trans. I. Chem. E.*, 53:1–6, 1975.

[7] M I G Bloor and D B Ingham. Boundary layer flows on the side walls of conical cyclones. *Trans. I. Chem. E.*, 54:276–280, 1976.

[8] M I G Bloor and D B Ingham. The flow in industrial cyclones. *J. Fluid Mech.*, 178:507–519, 1987.

[9] M I G Bloor and D B Ingham. The influence of vorticity on the efficiency of the hydrocyclone. In Pickford [52], pages 41–50.

[10] M I G Bloor and D B Ingham. On axially symmetric flow models for hydrocyclones. In Wood [53], pages 83–90.

[11] M R Davidson. Similarity solutions for flow in hydrocyclones. *Chemical Engineering Science*, 43:1499–1505, 1988.

[12] M D Brayshaw. A numerical model for the inviscid flow of a fluid in a hydrocyclone to demonstrate the effects of changes in the vorticity function of the flow field on particle classification. *International Journal of Mineral Processing*, 29:51–75, 1990.

[13] S R Knowles, D R Woods, and I A Fuerstein. The velocity distribution within a hydrocyclone operating without an air core. *Can.J.Chem.Engng*, 51:263, 1973.

[14] C A Capela Moraes, C M Hackenberg, C Russo, and R A Medronho. Theoretical analysis of oily water hydrocyclones. In Claxton et al. [54], pages 383 – 398.

[15] N Riley. High Reynolds' number flows with closed streamlines. *J.Engng Maths*, 15:15, 1981.

[16] P A Davidson. Swirling flow in an axisymmetric cavity of arbitrary profile, driven by a rotating magnetic field. *J. Fluid Mech.*, 245:669–99, 1992.

[17] A D Fitt. The character of 2-phase gas particulate equations. *Applied Mathematical Modelling*, 17:338–354, 1993.

[18] D A Drew and R T Wood. *Overview and Taxonomy of Models and Methods for Workshop on Two-Phase Flow Fundamentals.* National Bureau of Standards, 1985.

[19] M T Thew and M F Becker. Determination of phase behaviour in de-watering hydrocyclones using resistivity measurements: Feasibility study. In Claxton et al. [54], pages 73–93.

[20] J G Webster, editor. *Electrical Impedance Tomography.* Adam Hilger, 1990.

[21] W D Atkins. *Physical Chemistry.* Oxford, fourth edition, 1990.

[22] F J Dickin, R A Williams, and M S Beck. Determination of composition and motion of multicomponent mixtures in process vessels using electrical impedance

tomography–I. principles and process engineering applications. *Chemical Engineering Science*, 48:1883–1897, 1993.

[23] Z Q Chen and F J Paoloni. An integral equation approach to electrical conductance tomography. *IEEE Transactions on Medical Imaging*, 11:570–576, 1992.

[24] D C Barber and A D Seagar. Fast reconstruction of resistance images. *Clinical Physics and Physiological Measurement*, 8:47–54, 1987.

[25] D A G Bruggeman. *Ann. Phys. Leipzig*, 24:636, 1935.

[26] R E Meredith and C W Tobias. *Modern Aspects of Electrochemistry*, volume 14, page 61. Plenum, New York, 1962.

[27] J Bond, J C Cullivan, N Climpson, T Dyakowski, I Faulks, X Jia, J A Kostuch, D Peyton, M Wang, S J Wang, R M West, and R A Williams. Industrial monitoring of hydrocyclone operation using electrical impedance tomography. In *Proceedings of the first world congress on industrial process tomography*, 1999.

[28] S V Patankar. *Numerical Heat Transfer and Fluid Flow.* McGraw Hill, New York, 1980.

[29] P Bradshaw, editor. *Turbulence.* Springer-Verlag, 1976.

[30] R K Duggins and P C W Frith. Turbulence effects in hydrocyclones. In Wood [53], pages 75–82.

[31] F Boysan, R Weber, J Swithenbank, and P A Roberts. Modeling coal-fired cyclone combustors. *Combustion and Fame*, 63:73–86, 1986.

[32] H F Boysan. Renormalization group theory based turbulence models and their applications to industrial problems. In *Engineering Applications of Computational Fluid Dynamics*, pages 43–47, 1993.

[33] E G Hauptmann A Malhotra, R M R Branion. Modeling the flow in a hydrocyclone. *Canadian Journal of Chemical Engineering*, 72:953–960, 1994.

[34] B E Launder, G J Reece, and W Rodi. Progress in the development of a Reynolds' stress turbulence closure. *J. Fluid Mech.*, 68:537–566, 1975.

[35] H K Versteeg and W Malalasekera. *Computational Fluid Dynamics, The Finite Volume Method.* Longman Scientific and Technical, 1995.

[36] N C Markatos. The mathematical modelling of turbulent flows. *Appl. Math. Modelling*, 10:190–221, 1986.

[37] Z Han and R D Reitz. Turbulence modeling of internal-combustion engines using rng k-epsilon models. *Combustion Science and Technology*, pages 267–295, 1995.

[38] K T Hseih and R K Rajamani. Mathematical model of the hydrocyclone based on the physics of fluid flow. *AIChE Journal*, 37:735–747, 1991.

[39] T C Monredon, K T Hsieh, and R K Rajamani. Fluid flow model of the hydrocyclone: an investigation of device dimensions. *International Journal of Mineral Processing*, 35:65–83, 1992.

[40] A K Gupta, D G Lilley, and N Syred. *Swirl Flows.* Abacus Press, Tunbridge Wells, Kent, 1984.

[41] T Dyakowski and R A Williams. Modelling turbulent flow within a small-diameter hydrocyclone. *Chemical Engineering Science*, 48:1143–1152, 1993.

[42] F Boysan, W H Ayers, and J Swithenbank. A fundamental mathematical modelling approach to cyclone design. *Trans. I. Chem. E*, 60:222–230, 1982.

[43] K A Pericleous and N Rhodes andd G W Cutting. A mathematical model for predicting the flow field in a hydrocyclone classifier. In Pickford [52], pages 27–40.

[44] A Rochino. *J Appl. Mech.*, 36:151, 1969.

[45] L Ma, D B Ingham, and X Wen. A numerical simulation of the fluid flow and the collection efficiency of small personal cyclones. In *The 1997 Jubilee Research Event*, pages 253–256, 1997.

[46] M D Slack and A E Wraith. Modelling the velocity distribution in a hydrocyclone. Fluent Technical Report, 1998.

[47] A D Fitt D M Small and M T Thew. The influence of swirl and turbulence anisotropy on cfd modelling for hydrocyclones. In Claxton et al. [54], pages 49 – 62.

[48] A Loader. *Instability and turbulence in confined swirling flow investigated by laser doppler anemometry.* PhD thesis, University of Southampton, 1981.

[49] AEA Technology, Computational Fluid Dynamics Services, Building 8.19, Harwell Laboratory, Oxfordshire, UK. *CFDS-FLOW3D User Guide*, 1994.

[50] AEA Technology D Burt. Private communication, 1995.

[51] Computational Fluid Dynamics Services, Building 8.19, Harwell Laboratory, Oxfordshire 0X11 0RA, UK. *CFDS-FLOW3D User Guide*, 1994.

[52] Mrs. R Pickford, editor. *Second BHRA Conference on Hydrocyclones.* BHRA, 1984.

[53] P Wood, editor. *Third BHRA Conference on Hydrocyclones*, 1987.

[54] D Claxton, L Svarosky, and M Thew, editors. *Hydrocyclones '96*, 1996.